Development of Microfluidic Technologies for Novel Analysis of Fingermark Deposits and Unique Approaches to the Detection of SARS-CoV-2

Jamila Shakira Marshall

St. Joseph, Barbados

B.S. Chemistry, The University of the West Indies at Cave Hill, 2010

M.S. Chemistry, Clark Atlanta University, 2015

A Dissertation presented to the Graduate Faculty of the University of Virginia in Candidacy for the Degree of Doctor of Philosophy

Department of Chemistry

University of Virginia

July 2022

Abstract

Despite the development of innovative, state-of-the-art instrumentation based on the constant expansion of our scientific knowledge base, there is a deficit regarding the availability of field-deployable, low-cost, rapid, and sensitive apparatus for forensic and clinical analyses. Diagnostic and confirmatory tests remain primarily restricted to centralized laboratory settings and benchtop instrumentation, thereby creating strain on resources, multistep, laborious, and time-consuming processes requiring considerable operator input, and limited engagement with the communities dependent on the outcomes. Regarding forensic analyses, specifically, the reliance on laboratories for the processing and evaluation of items of potential evidentiary significance can result in delays that hinder time-sensitive criminal investigations and impede the apprehension of perpetrators.

Microfluidic technologies provide an attractive solution to this unmet need by virtue of their inherent advantages. These include the potential for portable, low-cost, rapid, automated, and integrated systems which are operable at the point of need or at the scene of a criminal investigation. This dissertation describes work towards the realization of micro total analysis systems (μTAs) for various applications.

The development of a microdevice for the identification of the biological sex of a perpetrator via assessment of biomarkers derived from fingermark deposits at the scene of a crime is detailed in Chapter 2. The research discussed in Chapter 3 pivots from the forensic application of microfluidic technology to clinical utilization – the rapid SARS-CoV-2 virus enrichment and RNA extraction for largescale diagnostic screening of clinical samples are explored therein. Along this vein, Chapter 4 details the optimization of a diagnostic protocol for the detection of SARS-CoV-2 using an ultra-rapid microfluidic

PCR instrument. Finally, this concept is expanded to explore the analysis of a bacterial target in Chapter 5, where the diagnosis of whooping cough is adapted to the ultra-rapid instrument via proof-of-concept experiments. Potential future directions, obstacles, and the anticipated broader societal impact of these developments on the field are summarized in the final chapter.

Acknowledgments

This achievement is only possible due to the support (and patience) of many during my time at the University of Virginia. Particularly, this dissertation would not be possible without the guidance and support of my research advisor, Professor James Landers, whose lab I was fortunate enough to join after leaving my first research group. I was apprehensive about "starting over" – especially as a student who had now not only been out of undergraduate school for seven years, but who had also taken a hit regarding my confidence in my abilities and my chosen path. However, during my time in your group, I have rediscovered and solidified my love for science. I have enjoyed working with like-minded individuals to address meaningful and relevant research problems. In addition to multiple opportunities to travel and communicate my research, I have met and casually chatted with professionals whose publications and texts I'd previously only referenced and reverently admired. Finally, and of personal significance, the "family first" response from you in times of crisis was deeply appreciated and made difficult times a little more bearable. I will always be truly grateful to you for this.

I have been fortunate enough to collaborate with many talented scientists, but I'd like to especially express my gratitude to Professor Hewlett and Dr. Fehling, whose guidance and resources made much of my work possible. I'd also like to thank Professor Mintz for making my first grad school experience incredibly enriching. I am also extremely grateful to the past, current, and future Ph.Ds. I've been fortunate to work alongside. Your boundless patience, respect, levity, generosity, support, kindness, and brilliant minds were invaluable and immeasurable gifts, and I am eternally grateful to have met and learned

from you. I also appreciate the opportunity to work with my undergrads, Maddy and Ella, whose support and contributions were pivotal to completing my research projects.

To Mike and the Roberts family – your support, friendship, advice, and generosity have helped to mold the person I have grown to be. It is not an overstatement to say that this would not have been possible without you, and I am incredibly grateful. You will forever be my family.

Daniel – your effervescence and passion for life, people, and at least half the dogs in the US have been a refreshing and unexpected addition to my life. Thank you for your support, your patience, and your selflessness. Thank you for getting me outdoors and ensuring I remembered to eat during some of the most stressful months of my life. Thank you for giving Sherlock and Jane Snow pets when I was overwhelmed. Thank you for being you and for sharing you with me.

To my family, words are insufficient to convey the depth of gratitude I have for you. I am me because of you. I keep going because of your eternal love and support. Thank you to Gran Gran for having a saying to cover every situation perfectly and for bolstering me with constant love and prayer. Thank you to my sissy, who is my favorite part of me. Thank you for picking up my calls, sharing my experiences, and encouraging me. Camille, the babies, my mood reader Aidan – thank you. To my mummy and daddy – your support, infinite love, selflessness, generosity, encouragement, patience, and at least 100 other similar words have always kept me going. I am extremely privileged to be your daughter.

Table of Contents

List of Figures

List of Tables

1. Introduction

1.1. Overview - Microfluidic Technologies

According to Whitesides, the field of microfluidics is rooted in four antecedent analytical domains – molecular analysis, biodefence, molecular biology, and microelectronics.[1] Molecular analyses include gas-phase chromatography, high-pressure liquid chromatography, and capillary electrophoresis.[1] The impetus from biodefence was the unmet need for field-deployable microfluidic systems to detect chemical and biological threats after the end of the cold war.[1] Another progenitor of microfluidics, molecular biology, is the study of macromolecules and associated mechanisms in living organisms. Microfluidic technology arose from this source as an implement with which the requirement for techniques and tools for the analysis of individual microscopic specimens under a continuous fluid flow could be addressed.[2] The additional advantages of this application were the potential for parallel experiments with high sample density and significantly increased throughput.[3]

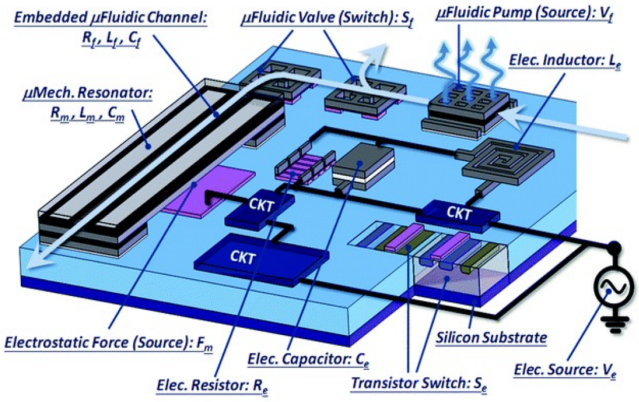

Figure 1-1. Schematic of a single-chip microsystem comprised of microfluidics, micromechanics, and microelectronics with equivalent circuit analogy. Fluidic, mechanical, and electrical domains are denoted by subscript *f*, *m*, and *e*, respectively. Adapted from [4].

Finally, microelectronics provided the framework for modern microfluidics as it was anticipated that the successful technologies associated with photolithography, namely microelectromechanical systems (MEMS) and silicon microelectronics, would be directly

applicable.[1,4] **Figure 1-1** depicts the interconnected nature of these concepts described by Li and Cheng.[4]

Microfluidic technologies entail the control and manipulation of fluid flows with length scales less than a millimeter by employing a number of devices and methods.[5] The volumes of fluid being manipulated are exceedingly small, with processing in the range of microliters to picolitres. Examples of such tools are micro-total analysis systems (μTAs), organ-on-a-chip, and lab-on-a-chip (LOC; previously lab-on-a-CD) devices, which are used for various applications. These include biomedicinal, food processing, environmental sensing, forensic, biochemical, clinical, and pharmaceutical analyses.[1,3–11,12] A schematic summarizing typical applications of microfluidic technologies is shown in **Figure 1-2**.[13.] Further, microfluidics is an interdisciplinary field due to its overlap with microtechnology, optics, biotechnology, materials science, physics, engineering, micromachining, and chemistry.[6]

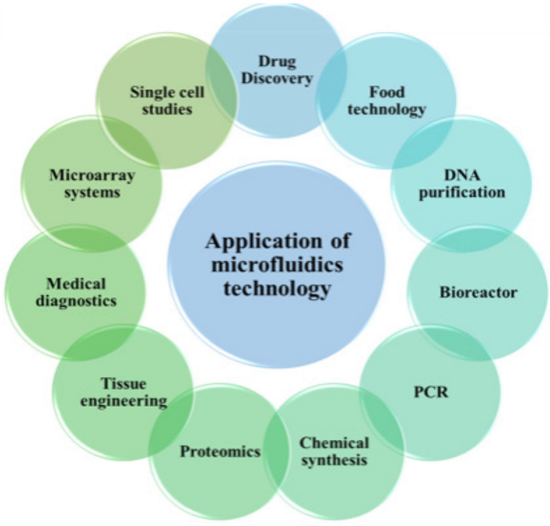

Figure 1-2. Common applications of microfluidic technology. Adapted from [13].

This multifaceted array of applications facilitated by microfluidic technology is supported by the inherent advantages of its "toolbox". These advantages include faster response or "sample-to-answer" times, decreased consumption of sample and reagents, lower operational costs, mitigation, or elimination of cross-contamination by decreasing steps requiring operator input, high analytical throughput, enhanced sensitivity, facile parallelization through multiplexing, potential system integration, reduced energy

consumption, rapid prototyping, portability, and facile fabrication and mass production.[6,8,9,14–18]

Despite the numerous advantages introduced by the miniaturization of conventional analytical techniques, the dominant testing model is the centralized laboratory.[19] The associated traditional strategies often require benchtop instrumentation, specialized operator training, labor-intensive and arduous tasks, and longer turnover times.[19,20] This was distinctly evident in the initial stages of the novel Betacoronavirus severe acute respiratory syndrome coronavirus 2 (SARS-CoV-2) global pandemic, where screening and diagnostic testing were severely stymied by the associated overwhelming burden on resources and clinical practitioners.[21,22]

Although this deficit was highlighted in a clinical setting, a survey of the literature indicates that there is also a considerable requirement for rapid, accurate, and portable devices for use on location in forensic investigation.[15,18,23–25] These apparently disparate fields possess a single unifying factor – there is an unmet need for field-deployable, sensitive, accurate and robust technology for rapid testing in non-centralized laboratory settings. Viewed through this lens, **Chapters 2-5** detail the development and optimization of technologies that serve to alleviate this need.

1.2. Principles of Microfluidics

1.2.1. Overview of Fluid Dynamics

The most critical factor at the core of microfluidics is the variation in fluid behavior at the microscale vs. the macroscale. Bruus defines a fluid as a liquid or a gas which deforms easily and continuously when external forces are applied.[26] On the macroscopic

scale, fluid approximates continuity and exhibits turbulent flow; this refers to unexpected movements and chaotic mixing between fluid streams due to dominant inertial forces.[1,26–28,29] At this magnitude, there is convective mixing – that is, mixing occurs as a combination of all fluid flows.[28] A practical example of this type of mixing is the blending of milk into tea or coffee or rivers flowing.[1,28] At the microscale, however, there is no convective mixing of fluids as volume forces associated with the macroscale are supplanted by surface phenomena such as capillary forces.

Consequently, liquid flow is passive; when two fluid flows converge on the microscale, parallel flow results, and mixing is facilitated by the diffusion of molecules across the fluid interface. This phenomenon is referred to as laminar flow.[1,27,30]At this magnitude, viscosity replaces inertia as the dominant force. The extent to which inertial vs. viscous forces influence the flow of fluids is represented by a dimensionless parameter known as Reynold's number.[1,27,31,32] **Figure 1-3** illustrates the characteristic differences between laminar and turbulent flow at fluid interfaces.[30]

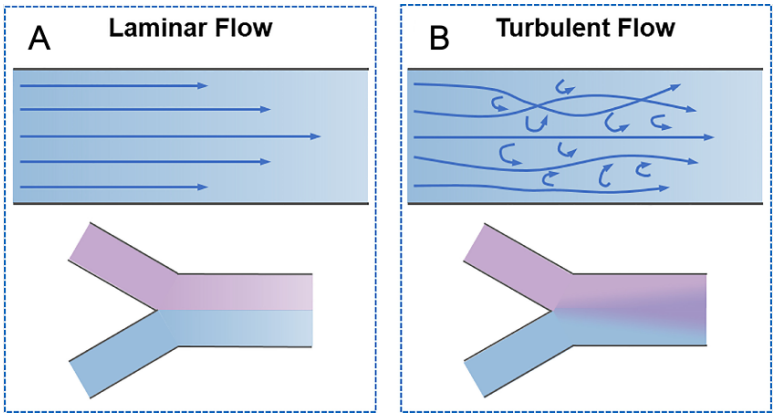

Figure 1-3. Interface characteristics of the liquid flow in microfluidic channels. (A) depicts laminar flow. At this magnitude, the interface between adjacent microfluidic flow is defined and distinct. (B) shows turbulent flow, where the interface between fluid flows is less discernable.

Reynold's number (Re) is calculated using the following equation:

$$Re = \frac{\rho v l}{\mu}$$

where ρ is the density, v is velocity, μ is the viscosity coefficient, and l is the channel diameter.[30,32,33] The transition between laminar and turbulent flow occurs when Re is approximately 2000, with turbulent flow occurring when Re is >2000 while laminar flow is dominant at Re values <2000.[30,34]

These phenomena provide the basis for the creation of microfluidic platforms, defined by Mark et al. as an easily combinable set of microfluidic unit operations that allow for miniaturization and well-defined fabrication.[27] The following section briefly describes these unit operations.

1.1.1 Unit Operations and Microfluidic Platforms

Unit operations comprise the basic fluidic functionalities of a microfluidic platform.[27,35] An extensive but not exhaustive list of unit operations includes sample and reagent supply, pre-storage, release, aliquoting, mixing switching, metering, separation or concentration of molecules, valving, routing, and liquid transport.[27,35] To maximize efficiency, microfluidic platforms should ideally provide an adequate number of unit operations for facile combination and implementation. Combined, unit chains enable experimental workflows or serve as the foundation for assay integration. In tandem, a fusion of unit operations is referred to as a process chain.[35] A pertinent example of a process chain is the enrichment, extraction, and amplification of viral RNA, as detailed in **Chapter 3**.

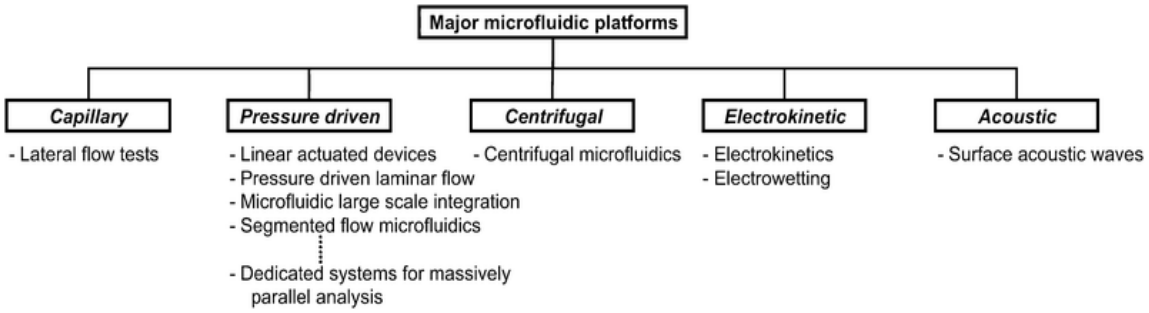

Figure 1-4. Classification of microfluidic platforms according to the characteristic principles of liquid propulsion. Reproduced from [27] with permission from the Royal Society of Chemistry.

According to Mark et al., microfluidic platforms can be assigned to one of five groups (**Figure 1-4**) – capillary, pressure-driven, electrokinetic, acoustic, and centrifugal.[27] These will be briefly reviewed below for the purpose of comprehensive discussion. Still, centrifugal platforms were utilized in this work and will be more explicitly detailed.

Capillary Microfluidics

Devices of this type rely on capillary action to manipulate liquids and allow for the movement of fluids in microchannels without requiring external pumping apparatus.[36,37] The movement of liquid in such platforms is governed by the wettability or wetting properties of the porous or microstructured substrate which comprises the capillary. Liquid flow into the capillaries is passive as the surface tension overcomes the effect of gravity and the liquid's viscosity. Recently, capillary microfluidics is most often associated with paper-based devices, which present low-cost options for assays and can be quickly prototyped.[27,36,37] In most cases, all required reagents are stored within the device, and the readout is optical and colorimetric. These are commonly referred to as "lateral flow tests",

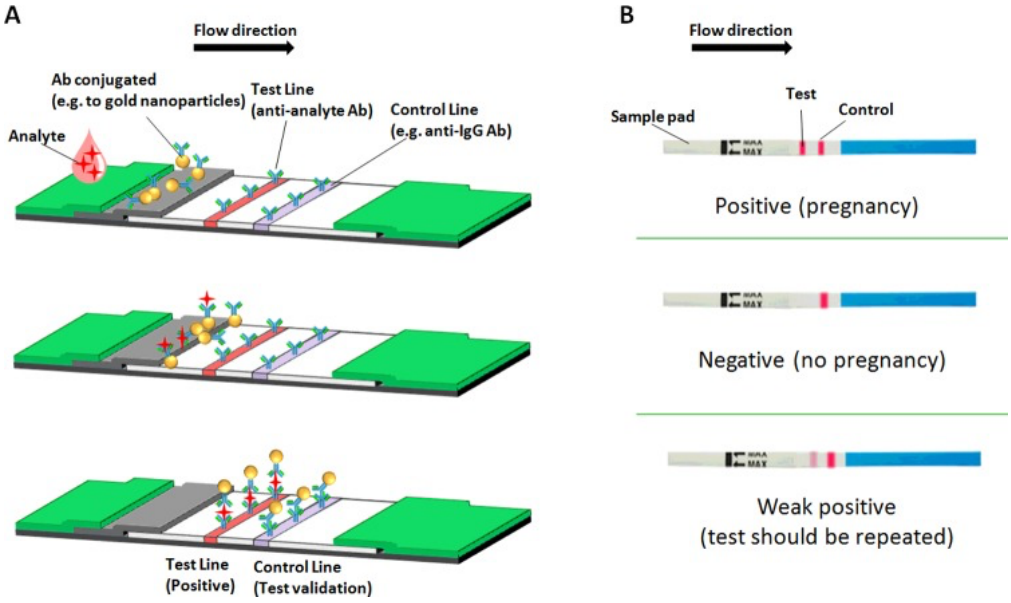

Figure 1-5. Schematic illustration of a lateral flow assay. (A) The image at the top details the deposition of the analyte on the sample pad and its migration towards a conjugate. The middle image illustrates the binding of the target analyte and its migration to the test line. The most vertical image shows the binding and capture of that target analyte. (B) An exemplary pregnancy test (One Step hCG Urine Test) potential results and their interpretation are shown. Reprinted from [38].

and the most widely known example of this technology is the pregnancy test strip (**Figure 1-5**, reprinted from Koczula and Gallota[38]).

Pressure-Driven Microfluidics

These platforms are characterized by mechanisms of liquid transport based on pressure gradients.[27] The unit operation governing this platform is interfacing two or more fluid streams at the junction of a microfluidic channel.

Electrokinetic Microfluidics

In this case, differently charged particles can be controlled and propelled into motion by applying an external electric field. The induced flow is commonly termed electroosmotic flow. Electroosmosis can be used for bulk transport of liquids or separating

particles and molecules within it.[27,39]

Acoustic Microfluidics

Acoustic microfluidics leverages surface acoustic wave (SAW) technologies to manipulate the movement of fluids and particles. According to Zhang et al., acoustic waves are the vibrations that travel as disturbances in matter.[40] Specifically, surface acoustic waves propagate along an elastic material's surface and use droplets residing on a hydrophobic surface in a gaseous environment to transport fluids.[27,40,41] **Figure 1-6** shows an illustration of this phenomenon. (Reproduced from Mark et al. [27] with the permission of the Royal Society of Chemistry.

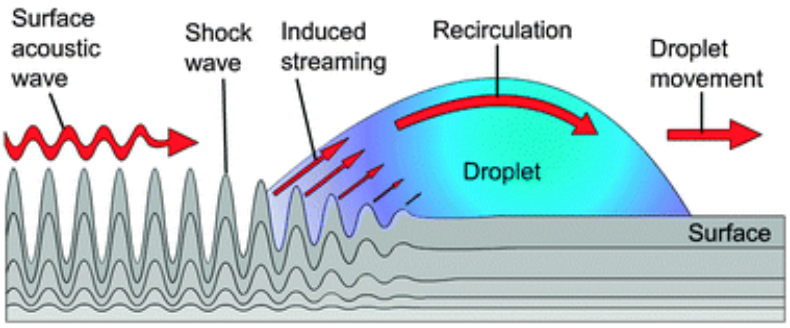

Figure 1-6. The mechanism of a surface acoustic wave (SAW). A stream is induced by the shock waves on the solid-liquid interface resulting in the movement of the droplet. Reproduced from [27] with the permission of the Royal Society of Chemistry.

Centrifugal Microfluidics

Centrifugal microfluidics leverage physical forces to facilitate unit operations.[35] Fluidic behaviors are controlled by the rotational speed, channel geometry, radial location of fluid reservoirs, and sample properties such as density and viscosity.[42,43] This

characteristic method of liquid propulsion is advantageous as it removes the requirement for external pumps while creating a closed fluidic system.[35]

Summarily, according to Ducrée et al., fluid on a planar substrate with a mass density ρ rotating at a distance r from a central axis at an angular velocity ω experiences a centrifugal force (density),

$$f_\omega = \rho r \omega^2$$

an Euler force (density)

$$f_E = \rho r \frac{d\omega}{dt}$$

scaling with the rotational acceleration $d\omega/dr$ and the Coriolis force (density)

$$f_C = 2\rho\omega v$$

scaling with the fluid velocity v in the plane of the substrate, as described in **Figure 1-7**. (Adapted from Madadelahi et al. with permission from the Royal Society of Chemistry.[44]

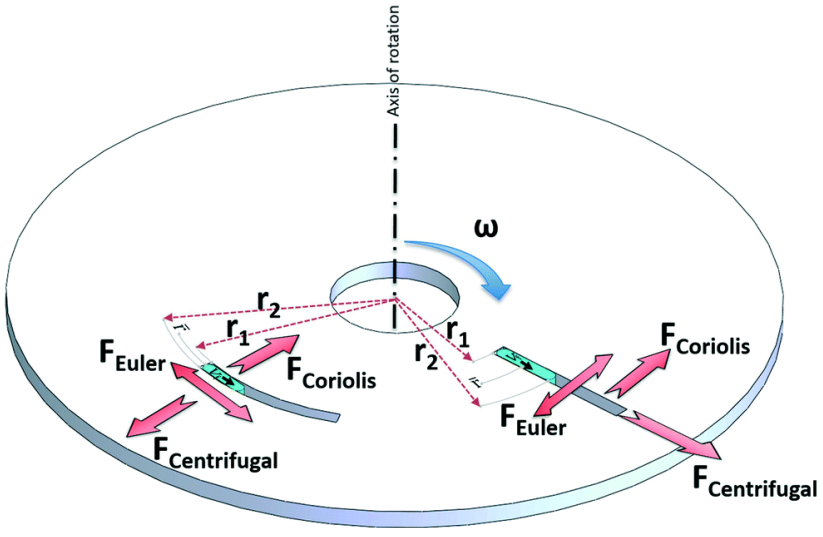

Figure 1-7. Schematic illustrating a centrifugal microfluidic device. The primary influential forces arising from rotation are highlighted. Adapted from [44] with permission from the Royal Society of Chemistry.

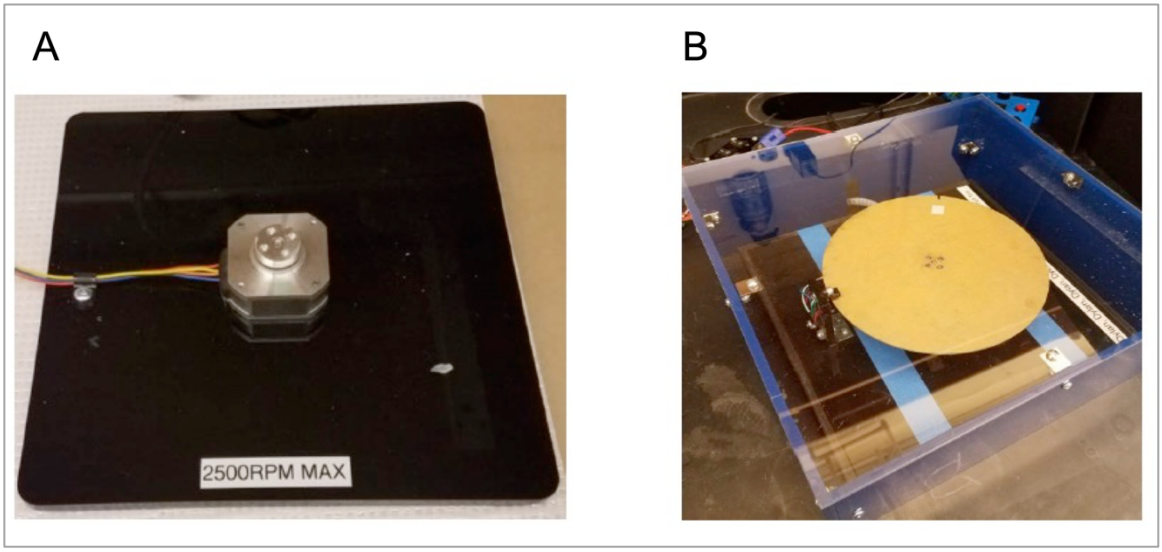

Figure 1-8. Custom-built spin systems. (A) Spin system capable of bidirectional rotations with a maximum frequency of 2500 rpm. (B) Unidirectional spin system capable of rotation frequencies of up to 9000 rpm.

In centrifugal microfluidic systems, these three forces may be directly controlled by the frequency of rotation. This platform is highlighted in the work described in this dissertation; the development and application of a "lab-on-a-disc" device are detailed in **Chapter 2**, while the transferal of fluid in the microfluidic cartridges used in **Chapters 3 to 5** is facilitated via centrifugal rotations. **Figures 1-8A and B** illustrate centrifugal spin systems used in the projects described in the subsequent chapters. Unit operations facilitated by this platform include batch-mode mixing via rapid bidirectional rotations of the spin system and routing whereby specific, discrete volumes were transferred. At the same time, the excess was discarded or retained in the initial chamber as waste.[45]

Centrifugal devices used in the projects discussed were manufactured using the "Print-Cut-Laminate" method pioneered in the Landers lab or via injection molding of polymeric material.[46]

1.3. Onsite Application of Microfluidic Technologies

To preface the projects described in this dissertation, it is necessary to briefly provide an overview of the research problems being addressed along with the associated challenges. Consequently, foundational information regarding the application of microfluidic technologies to forensic and clinical analyses will be detailed in the following sections. The information outlining the forensic applications lays the groundwork for further discussion of the novel adaptation of the Sakaguchi reaction for arginine to a microfluidic platform for the identification of biological sex, as detailed in **Chapter 2**. Subsequently, the basic requirements for point-of-need microfluidic technologies will support further discussion of the unique applications described in **Chapters 3, 4,** and **5**.

1.3.1. Microfluidics for Forensic Applications

In any criminal investigation, the priority for forensic analysts and law enforcement officials is the efficient, accurate, and thorough evaluation of items of evidentiary value to minimize the time elapsed between the commission of a crime and apprehension of a perpetrator. Consequently, onsite forensic investigations would minimize delays encountered when evidence must be located, processed, and dispatched to centralized forensic laboratories for analysis. Such analyses would also reduce the likelihood that perpetrators could depart a crime scene or destroy evidence.[23,47–49]

Further, evidence is often present in trace amounts. As such, it is critical to maximize the information gleaned from these items, as there is little room for error or potential sample loss. The inherent characteristics of microfluidic platforms thus make them suitable for application to forensic investigations. Such benefits include rapid testing,

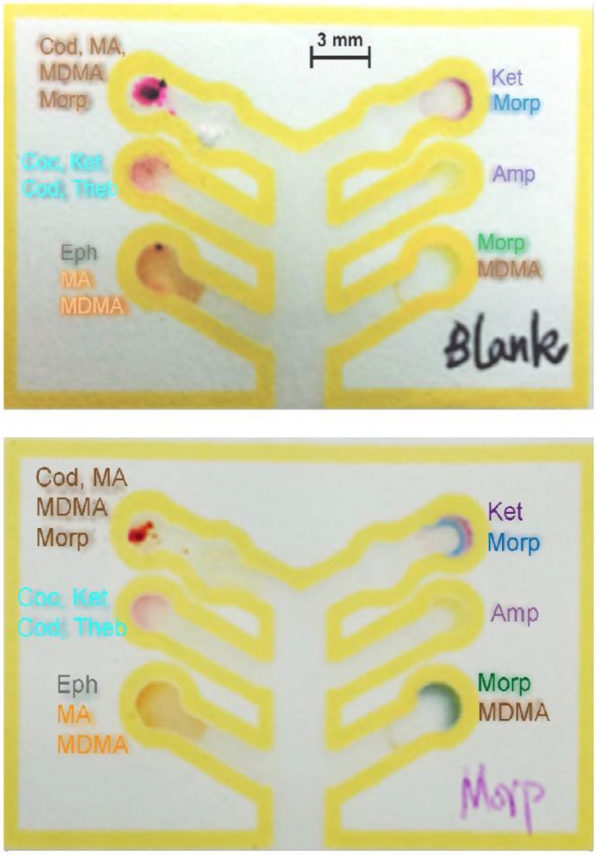

Figure 1-9. µPAD developed to analyze drugs of abuse at a crime scene. Top – Blank Sample; Bottom-a positive result for morphine. Each lane of the device is labeled with the name and color at which each analyte should appear. Lane 1: ephedrine (Eph), methamphetamine (MA) and MDMA; Lane 2: cocaine (Coc), codeine (Cod), ketamine (Ket) and thebaine (The); Lane 3: codeine (Cod), methamphetamine (MA), MDMA and morphine (Morp); Lane 4: ketamine (Ket) and morphine (Morp); Lane 5 amphetamine (Amp); Lane 6 morphine (Morp) and MDMA.

portability, the ability to analyze trace amounts of samples, simplicity, and integration of these systems into existing process chains.[23,48,50,51]

In addition to simplifying sample processing, microfluidic testing is also amenable to evaluating various analyte types. These include body fluids such as urine, blood, saliva, and semen, explosives, gunshot residue, drugs of abuse, and recently (as detailed in **Chapter 2**), the components of fingermark deposits.[23,25,48,52] An example of simple microfluidic platforms for onsite analyses, the micro paper-based analytical devices (µPADs), is shown in **Figure 1-9**.

Recently, the evidence most commonly sought at a crime scene is trace amounts of nucleic acids (deoxyribonucleic acids, DNA, and ribonucleic acids, RNA). To analyze evidence of this type after collection, the "sample" workup usually consists of three steps: cell lysis, DNA extraction, and DNA purification. Briefly, cell lysis may be thermal, chemical, electrochemical, mechanical, or optically induced.[23,16] The details of these steps are outside the focus of this work and will not be discussed in detail. DNA extraction and purification, however, are more pertinent

to the research described here, though not addressed in a forensic capacity. The application of these concepts to clinical applications will be discussed in the following section.

DNA extraction is commonly achieved via solid phase extraction (SPE), binding to magnetic beads, and differential extraction, among other techniques.[23] Microfluidic applications to address these workflows have been explored and discussed by previous research conducted in the Landers Lab.[53–57] As quantities of nucleic acid obtained at crime scenes are usually low as a cell only contains approximately six pg of DNA,[58] amplification is required to ascertain identifying information from this evidence. While multiple methods have been used for this process, the most common is polymerase chain reaction (PCR) which will be briefly outlined here. Other popular techniques include loop-mediated amplification (LAMP) and multiple displacement amplification (MDA).

Polymerase Chain Reaction (PCR)

PCR is a technique by which DNA is amplified exponentially from only a minimal amount of starting material and has been extensively discussed in the literature.[59] Briefly, it consists of three main steps, which comprise an amplification cycle – denaturation, annealing, and extension. These steps are summarized in **Figure 1-10**.[60]

Denaturation refers to the process by which double-stranded DNA is "melted" into single strands or secondary structure in single-stranded DNA is loosened via high-temperature incubation. This denaturation usually occurs at 95 °C.[61] Complementary sequences then hybridize into single strands during the annealing step at 60 – 65 °C.

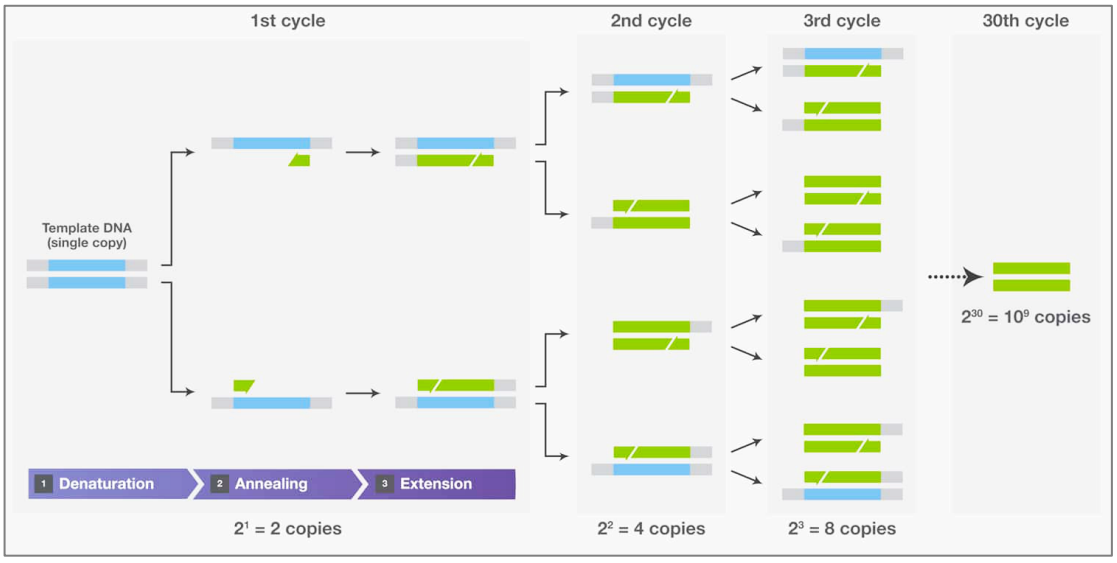

Figure 1-10. Three steps of PCR. These steps are denaturation, annealing, and extension. Exponential amplification of target DNA occurs with repeated cycling. Adapted from [60].

Finally, extension or elongation to synthesize new DNA strands occurs. Typically, 30 – 40 cycles are required for amplification.[59,61] In recent years, several research studies have focused on achieving the fastest on-chip amplification with no loss of sensitivity or specificity.[23] Similar efforts are described in **Chapters 3 – 5**.

Though DNA evidence is a preeminent source of evidence in forensic investigations, fingerprint analysis remains an indispensable tool in identifying perpetrators. It has been reported that fingerprints outperform DNA analysis technologies and similar systems of identification in discerning offenders.[62] In most cases, however, fingerprint analyses entail biometric analysis of the physical pattern and require matches within a database or with an apprehended suspect.[63] Consequently, fingerprints may be used only as exclusionary evidence. Recently, there has been an increase in research into the biological content of deposited fingerprints - termed "fingermark deposits".[64,65] It is theorized that these deposits could eventually be utilized as body fluid evidence

comparable to blood, saliva, or urine. Accordingly, the adaptation of a colorimetric test to a microfluidic platform for the analysis of fingermark deposits is described in **Chapter 2**.

1.3.2. Microfluidics for Clinical Applications

The clinical applications of microfluidic technology for onsite use are often referred to as "point-of-care" (POC) or "point-of-need" (PON) technologies. In addition to presenting alternatives to expensive instrumentation and centralized laboratory processing, these platforms are expected to be affordable, portable, rapid, user-friendly, and amenable to integration.[66–68] Such technologies play a significant role in monitoring and maintaining public health. For example, it was reported that HIV (Human Immunodeficiency Virus) patients tested with a POC device received treatment 130 days faster than those diagnosed using a traditional, centralized lab.[69,70] Sensitivity, accuracy, and speed are critical concerns as these must be maintained for POC devices despite microscale volumes and minimal amounts of analyte. Typical targets for such analyses include metabolites, drugs, human cells, microbes, proteins, and dissolved ions and gases, and sample types are usually blood, saliva, urine, or other comparable body fluids.[71]

The need for such technologies was starkly highlighted during the COVID-19 global pandemic when resources and clinicians quickly became overwhelmed by the burden of mitigating community spread and providing treatment for infected individuals.[72] Still, before the pandemic, the need for such devices in low-resource or remote communities existed in the public consciousness. This prompted the World Health Organization (WHO) to explicitly outline the characteristics of an ideal diagnostic test that could be used in the developing world; such tests are ideally to be **ASSURED** – **A**ffordable

by those at risk of infection, **S**ensitive, **S**pecific, **U**ser-friendly, **R**apid, **E**quipment-free (no significant consumption of power required for operation) and **D**elivered to those who need it.[16,73]

Although there are several microfluidic platforms for clinical POC analyses, PCR is the "gold standard" for molecular diagnostics of this type and usually targets nucleic acids.[67] However, Nucleic Acid Amplification Tests (NAATs), commonly used to describe molecular diagnostics, may also utilize isothermal amplification methods. While PCR uses multiple temperatures to achieve amplification, as described above, isothermal amplification relies on a single temperature which can usually be relatively low, and specific enzymes which denature DNA in preparation for amplification.[16] An exemplary isothermal technique is loop-mediated amplification (LAMP) which does not require heat for the denaturation of double-stranded DNA.[74,75] Lateral flow assays (LFAs) are also used for POC diagnostics and have the advantage of completely satisfying the ASSURED requirements.[73] However, several limitations are associated with this platform, including low sensitivity, lot-to-lot variability, and the acquisition of only qualitative or semi-quantitative results.[16,76,77]

NAATs are usually amenable to automation and integration, sensitive, specific, and straightforward. However, a significant drawback of using gold standard PCR techniques for NAATs is the requirement for complex and bulky thermal cycling equipment, longer turnaround times, and higher power consumption.[16] **Chapters 3, 4,** and **5** thus detail the optimization of assays and instrumentation, which directly address this issue. Sensitivity and specificity of the assay for largescale diagnostics are enhanced by using nanoparticles for the enrichment of nucleic acids (**Chapter 3**)[78], while a portable, comparatively

lightweight instrument that does not require consumption of large amounts of power for rapid PCR amplification analyses[79] is primarily described in **Chapters 4** and **5**.

Another consideration when designing POC assays is sample type; how clinical samples are obtained can significantly impact assay sensitivity and directly influence the likelihood of procuring accurate results. The amenability of applying such methods to infected persons is also reliant on patient comfort and ease of use. At the beginning of the COVID-19 global pandemic, nasopharyngeal and oropharyngeal swabbing were used to obtain clinical samples for diagnoses. However, the requirement for a trained technician or clinician for swabbing, the discomfort and pain experienced by the patient when these methods were used, and a resultant swab shortage initiated research into the analysis of additional sample types.[21,67,80] Nasal swabs, which are less painful and well-suited to patient self-testing, were introduced as an alternative sampling method. Additionally, saliva-based assays were explored as these possess inherent advantages such as ease of use, painless and non-invasive sample collection, and comparable diagnostic performance.[81–84] The variations in sample types and disparate reported data regarding sensitivity and viability of multiple sampling methods motivated the investigation and comparison of diverse clinical sample types as described in **Chapter 3**.

1.4. Research Goals and Concluding Remarks

This dissertation focuses on the development and adaptation of workflows to microfluidic platforms. Specifically, a prominent theme discussed in the following chapters is the optimization of clinical assays to achieve ultra-rapid, accurate, and portable methods of detection or diagnosis. **Chapter 3** describes the optimization of a diagnostic process;

however, unlike **Chapters 4 and 5**, the focus is on maximizing resources for large-scale diagnostics with an eye toward field deployment rather than reducing the runtime of assays while maintaining or improving diagnostic efficiency.

Chapter 2 deviates from the theme of clinical applications – this chapter details the development of a microfluidic device for identifying biological sex from biomarkers contained in a fingermarks deposit matrix. Still, the eventual goal is integration and onsite use when this technology has matured.

Finally, **Chapter 6** outlines the steps required to complete the validation of these projects and toward eventual integration and expansion of the themes discussed. Analyzed comprehensively, the overarching theme of this work is exploring and evaluating solutions to address the requirement for field forward technologies for these applications.

1.5. References

1. Whitesides, G. M. The Origins and the Future of Microfluidics. *Nature* **2006**, *442* (7101), 368–373. https://doi.org/10.1038/nature05058.

2. A, T. *LibGuides: History of Molecular Biology and Biotechnology: Molecular Biology*. https://cshl.libguides.com/c.php?g=474065&p=3243790 (accessed 2022-07-01).

3. Sonnen, K. F.; Merten, C. A. Microfluidics as an Emerging Precision Tool in Developmental Biology. *Developmental Cell* **2019**, *48* (3), 293–311. https://doi.org/10.1016/j.devcel.2019.01.015.

4. Li, S.-S.; Cheng, C.-M. Analogy among Microfluidics, Micromechanics, and Microelectronics. *Lab Chip* **2013**, *13* (19), 3782–3788. https://doi.org/10.1039/C3LC50732G.

5. Stone, H. A.; Stroock, A. D.; Ajdari, A. Engineering Flows in Small Devices: Microfluidics Toward a Lab-on-a-Chip. *Annu. Rev. Fluid Mech.* **2004**, *36* (1), 381–411. https://doi.org/10.1146/annurev.fluid.36.050802.122124.

6. Jiang, L.; Korivi, N. S. 13 - Microfluidics: Technologies and Applications. In *Nanolithography*; Feldman, M., Ed.; Woodhead Publishing, 2014; pp 424–443. https://doi.org/10.1533/9780857098757.424.

7. Aryasomayajula, A.; Bayat, P.; Rezai, P.; Selvaganapathy, P. R. Microfluidic Devices and Their Applications. In Springer Handbook of Nanotechnology; Bhushan, B., Ed.; Springer Berlin Heidelberg: Berlin, Heidelberg, 2017; pp 487–536. https://doi.org/10.1007/978-3-662-54357-3_16.

8. Berlanda, S. F.; Breitfeld, M.; Dietsche, C. L.; Dittrich, P. S. Recent Advances in Microfluidic Technology for Bioanalysis and Diagnostics. Anal. Chem. 2021, 93 (1), 311–331. https://doi.org/10.1021/acs.analchem.0c04366.

9. Sia, S. K.; Kricka, L. J. Microfluidics and Point-of-Care Testing. Lab Chip 2008, 8 (12), 1982–1983. https://doi.org/10.1039/B817915H.

10. Reyes, D. R.; Iossifidis, D.; Auroux, P.-A.; Manz, A. Micro Total Analysis Systems. 1. Introduction, Theory, and Technology. Anal. Chem. 2002, 74 (12), 2623–2636. https://doi.org/10.1021/ac0202435.

11. Pumera, M. Microfluidics in Amino Acid Analysis. *Electrophoresis* **2007**, *28* (13), 2113–2124. https://doi.org/10.1002/elps.200600709.

12. Sun, W.; Luo, Z.; Lee, J.; Kim, H.-J.; Lee, K.; Tebon, P.; Feng, Y.; Dokmeci, M. R.; Sengupta, S.; Khademhosseini, A. Organ-on-a-Chip for Cancer and Immune Organs Modeling. *Advanced Healthcare Materials* **2019**, *8* (4), 1801363. https://doi.org/10.1002/adhm.201801363.

13. Pattanayak, P.; Singh, S. K.; Gulati, M.; Vishwas, S.; Kapoor, B.; Chellappan, D. K.; Anand, K.; Gupta, G.; Jha, N. K.; Gupta, P. K.; Prasher, P.; Dua, K.; Dureja, H.; Kumar, D.; Kumar, V. Microfluidic Chips: Recent Advances, Critical Strategies in Design, Applications and Future Perspectives. *Microfluid Nanofluidics* **2021**, *25* (12), 99. https://doi.org/10.1007/s10404-021-02502-2.

14. Cui, P.; Wang, S. Application of Microfluidic Chip Technology in Pharmaceutical Analysis: A Review. *Journal of Pharmaceutical Analysis* **2019**, *9* (4), 238–247. https://doi.org/10.1016/j.jpha.2018.12.001.

15. Horsman, K. M.; Bienvenue, J. M.; Blasier, K., R.; Landers, J. P. Forensic DNA Analysis on Microfluidic Devices: A Review. *J Forensic Sci* **2007**, *52* (4), 784–799. https://doi.org/10.1111/j.1556-4029.2007.00468.x.
16. Sachdeva, S.; Davis, R. W.; Saha, A. K. Microfluidic Point-of-Care Testing: Commercial Landscape and Future Directions. *Frontiers in Bioengineering and Biotechnology* **2021**, *8*.

17. St John, A.; Price, C. P. Existing and Emerging Technologies for Point-of-Care Testing. *Clin Biochem Rev* **2014**, *35* (3), 155–167.

18. Al-Hetlani, E. Forensic Drug Analysis and Microfluidics. *Electrophoresis* **2013**, *34*, 1262–1272. https://doi.org/10.1002/elps.201200637.

19. Wang, X.; Hong, X.-Z.; Li, Y.-W.; Li, Y.; Wang, J.; Chen, P.; Liu, B.-F. Microfluidics-Based Strategies for Molecular Diagnostics of Infectious Diseases. *Military Medical Research* **2022**, *9* (1), 11. https://doi.org/10.1186/s40779-022-00374-3.

20. Miyazaki, C. M.; Carthy, E.; Kinahan, D. J. Biosensing on the Centrifugal Microfluidic Lab-on-a-Disc Platform. *Processes* **2020**, *8* (11). https://doi.org/10.3390/pr8111360.

21. Guan, W.; Ni, Z.; Hu, Y.; Liang, W.; Ou, C.; He, J.; Liu, L.; Shan, H.; Lei, C.; Hui, D. S. C.; Du, B.; Li, L.; Zeng, G.; Yuen, K.-Y.; Chen, R.; Tang, C.; Wang, T.; Chen, P.; Xiang, J.; Li, S.; Wang, J.; Liang, Z.; Peng, Y.; Wei, L.; Liu, Y.; Hu, Y.; Peng, P.; Wang, J.; Liu, J.; Chen, Z.; Li, G.; Zheng, Z.; Qiu, S.; Luo, J.; Ye, C.; Zhu, S.; Zhong, N. Clinical Characteristics of Coronavirus Disease 2019 in China. *New England Journal of Medicine* **2020**, *382* (18), 1708–1720. https://doi.org/10.1056/NEJMoa2002032.

22. Zhu, N.; Zhang, D.; Wang, W.; Li, X.; Yang, B.; Song, J.; Zhao, X.; Huang, B.; Shi, W.; Lu, R.; Niu, P.; Zhan, F.; Ma, X.; Wang, D.; Xu, W.; Wu, G.; Gao, G. F.; Tan, W. A Novel Coronavirus from Patients with Pneumonia in China, 2019. *New England Journal of Medicine* **2020**, *382* (8), 727–733. https://doi.org/10.1056/NEJMoa2001017.
23. Bruijns, B.; van Asten, A.; Tiggelaar, R.; Gardeniers, H. Microfluidic Devices for Forensic DNA Analysis: A Review. *Biosensors (Basel)* **2016**, *6* (3). https://doi.org/10.3390/bios6030041.

24. Musile, G.; Agard, Y.; Wang, L.; De Palo, E. F.; McCord, B.; Tagliaro, F. Paper-Based Microfluidic Devices: On-Site Tools for Crime Scene Investigation. *TrAC Trends in Analytical Chemistry* **2021**, *143*, 116406. https://doi.org/10.1016/j.trac.2021.116406.

25. Liut, J.; Bott, U.; Madea, B.; Kramer, M.; Maas, A. Evaluation of RapidSTAT®, DrugWipe® 6S, DrugScreen® 5TK and DrugScreen® 7TR for on-Site Drug Testing in German Police Roadside Traffic Patrol. *Drug Test Anal.* **2022**, 1–10. https://doi.org/10.1002/dta.3262.

26. Bruus, H. *Theoretical Microfluidics*; Oxford Master Series in Physics; OUP Oxford, 2008.

27. Mark, D.; Haeberle, S.; Roth, G.; von Stetten, F.; Zengerle, R. Microfluidic Lab-on-a-Chip Platforms: Requirements, Characteristics and Applications. *Chem. Soc. Rev.* **2010**, *39* (3), 1153–1182. https://doi.org/10.1039/B820557B.

28. Castillo-León, J. Microfluidics and Lab-on-a-Chip Devices: History and Challenges. In *Lab-on-a-Chip Devices and Micro-Total Analysis Systems: A Practical Guide*; Castillo-León, J., Svendsen, W. E., Eds.; Springer International Publishing: Cham, 2015; pp 1–15. https://doi.org/10.1007/978-3-319-08687-3_1.

29. Azizipour, N.; Avazpour, R.; Rosenzweig, D. H.; Sawan, M.; Ajji, A. Evolution of Biochip Technology: A Review from Lab-on-a-Chip to Organ-on-a-Chip. *Micromachines* **2020**, *11* (6). https://doi.org/10.3390/mi11060599.

30. Cheng, S.; Chen, W.; Zhang, P. Developing Advanced Polymer Films Based on Microfluidic Laminar Flow. *Giant* **2022**, *9*, 100091. https://doi.org/10.1016/j.giant.2022.100091.

31. Squires, T. M.; Quake, S. R. Microfluidics: Fluid Physics at the Nanoliter Scale. *Rev. Mod. Phys.* **2005**, *77* (3), 977–1026. https://doi.org/10.1103/RevModPhys.77.977.

32. Reynolds, O. XXIX. An Experimental Investigation of the Circumstances Which Determine Whether the Motion of Water Shall Be Direct or Sinuous, and of the Law of Resistance in Parallel Channels. *Philosophical Transactions of the Royal Society of London* **1883**, *174*, 935–982. https://doi.org/10.1098/rstl.1883.0029.

33. Charmet, J.; Arosio, P.; Knowles, T. P. J. Microfluidics for Protein Biophysics. *Journal of Molecular Biology* **2018**, *430* (5), 565–580. https://doi.org/10.1016/j.jmb.2017.12.015.

34. Schulte, T. H.; Bardell, R. L.; Weigl, B. H. Microfluidic Technologies in Clinical Diagnostics. *Clinica Chimica Acta* **2002**, *321* (1), 1–10. https://doi.org/10.1016/S0009-8981(02)00093-1.

35. Strohmeier, O.; Keller, M.; Schwemmer, F.; Zehnle, S.; Mark, D.; von Stetten, F.; Zengerle, R.; Paust, N. Centrifugal Microfluidic Platforms: Advanced Unit Operations and Applications. *Chem. Soc. Rev.* **2015**, *44* (17), 6187–6229. https://doi.org/10.1039/C4CS00371C.

36. Olanrewaju, A.; Beaugrand, M.; Yafia, M.; Juncker, D. Capillary Microfluidics in Microchannels: From Microfluidic Networks to Capillaric Circuits. *Lab Chip* **2018**, *18* (16), 2323–2347. https://doi.org/10.1039/C8LC00458G.

37. Hassan, S.-U.; Tariq, A.; Noreen, Z.; Donia, A.; Zaidi, S. Z. J.; Bokhari, H.; Zhang, X. Capillary-Driven Flow Microfluidics Combined with Smartphone Detection: An Emerging Tool for Point-of-Care Diagnostics. *Diagnostics (Basel)* **2020**, *10* (8). https://doi.org/10.3390/diagnostics10080509.

38. Koczula, K. M.; Gallotta, A. Lateral Flow Assays. *Essays Biochem* **2016**, *60* (1), 111–120. https://doi.org/10.1042/EBC20150012.

39. Fu, L.-M.; Yang, R.-J.; Lee, G.-B.; Liu, H.-H. Electrokinetic Injection Techniques in Microfluidic Chips. *Anal. Chem.* **2002**, *74* (19), 5084–5091. https://doi.org/10.1021/ac025821w.

40. Zhang, P.; Bachman, H.; Ozcelik, A.; Huang, T. J. Acoustic Microfluidics. *Annual Rev. Anal. Chem.* **2020**, *13* (1), 17–43. https://doi.org/10.1146/annurev-anchem-090919-102205.

41. Ding, X.; Li, P.; Lin, S.-C. S.; Stratton, Z. S.; Nama, N.; Guo, F.; Slotcavage, D.; Mao, X.; Shi, J.; Costanzo, F.; Huang, T. J. Surface Acoustic Wave Microfluidics. *Lab Chip* **2013**, *13* (18), 3626–3649. https://doi.org/10.1039/C3LC50361E.

42. Madou, M.; Zoval, J.; Jia, G.; Kido, H.; Kim, J.; Kim, N. Lab on a CD. *Annu Rev Biomed Eng* **2006**, *8*, 601–628. https://doi.org/10.1146/annurev.bioeng.8.061505.095758.

43. Gorkin, R.; Park, J.; Siegrist, J.; Amasia, M.; Lee, B. S.; Park, J.-M.; Kim, J.; Kim, H.; Madou, M.; Cho, Y.-K. Centrifugal Microfluidics for Biomedical Applications. *Lab Chip.* **2010**, *10* (14), 1758–1773. https://doi.org/10.1039/B924109D.

44. Madadelahi, M.; Acosta-Soto, L. F.; Hosseini, S.; Martinez-Chapa, S. O.; Madou, M. J. Mathematical Modeling and Computational Analysis of Centrifugal Microfluidic Platforms: A Review. *Lab Chip* **2020**, *20* (8), 1318–1357. https://doi.org/10.1039/C9LC00775J.

45. Ducrée, J.; Haeberle, S.; Lutz, S.; Pausch, S.; Stetten, F. von; Zengerle, R. The Centrifugal Microfluidic Bio-Disk Platform. *Journal of Micromechanics and Microengineering* **2007**, *17* (7), S103–S115. https://doi.org/10.1088/0960-1317/17/7/s07.

46. Thompson, B. L.; Ouyang, Y.; Duarte, G. R. M.; Carrilho, E.; Krauss, S. T.; Landers, J. P. Inexpensive, Rapid Prototyping of Microfluidic Devices Using Overhead Transparencies and a Laser Print, Cut and Laminate Fabrication Method. *Nat. Protoc.* **2015**, *10* (6), 875–886. https://doi.org/10.1038/nprot.2015.051.

47. de Araujo, W. R.; Cardoso, T. M. G.; da Rocha, R. G.; Santana, M. H. P.; Muñoz, R. A. A.; Richter, E. M.; Paixão, T. R. L. C.; Coltro, W. K. T. Portable Analytical Platforms for Forensic Chemistry: A Review. *Analytica Chimica Acta* **2018**, *1034*, 1–21. https://doi.org/10.1016/j.aca.2018.06.014.

48. Cromartie, R. L.; Wardlow, A.; Duncan, G.; McCord, B. R. Development of a Microfluidic Device (MPADs) for Forensic Serological Analysis. *Anal. Methods* **2019**, *11* (5), 587–595. https://doi.org/10.1039/C8AY02080A.

49. Estes, M. D.; Yang, J.; Duane, B.; Smith, S.; Brooks, C.; Nordquist, A.; Zenhausern, F. Optimization of Multiplexed PCR on an Integrated Microfluidic Forensic Platform for Rapid DNA Analysis. *The Analyst* **2012**, *137* (23), 5510–5519. https://doi.org/10.1039/c2an35768b.

50. DuVall, J. A.; Le Roux, D.; Thompson, B. L.; Birch, C.; Nelson, D. A.; Li, J.; Mills, D. L.; Tsuei, A.; Ensenberger, M. G.; Sprecher, C.; Storts, D. R.; Root, B. E.; Landers, J. P. Rapid Multiplex DNA Amplification on an Inexpensive Microdevice for Human Identification via Short Tandem Repeat Analysis. *Anal Chim Acta* **2017**, *980*, 41–49. https://doi.org/10.1016/j.aca.2017.04.051.

51. Roux, D. L.; Root, B. E.; Hickey, J. A.; Scott, O. N.; Tsuei, A.; Li, J.; Saul, D. J.; Chassagne, L.; Landers, J. P.; Mazancourt, P. de. An Integrated Sample-in-Answer-out Microfluidic Chip for Rapid Human Identification by STR Analysis. *Lab Chip* **2014**, *14* (22), 4415–4425. https://doi.org/10.1039/C4LC00685B.

52. Marshall, J. S.; Sita, M. L.; Landers, J. P. Microfluidic Device for the Identification of Biological Sex by Analysis of Latent Fingermark Deposits. *Micromachines* **2021**, *12* (4). https://doi.org/10.3390/mi12040442.

53. Dignan, L. M.; Woolf, M. S.; Tomley, C. J.; Nauman, A. Q.; Landers, J. P. Multiplexed Centrifugal Microfluidic System for Dynamic Solid-Phase Purification of Polynucleic Acids Direct from Buccal Swabs. *Anal. Chem.* **2021**, *93* (19), 7300–7309. https://doi.org/10.1021/acs.analchem.1c00842.

54. Clark, C.; Turiello, R.; Cotton, R.; Landers, J. P. Analytical Approaches to Differential Extraction for Sexual Assault Evidence. *Anal Chim Acta* **2021**, *1141*, 230–245. https://doi.org/10.1016/j.aca.2020.07.059.

55. Xu, K.; Clark, C. P.; Poe, B. L.; Lounsbury, J. A.; Nilsson, J.; Laurell, T.; Landers, J. P. Isolation of a Low Number of Sperm Cells from Female DNA in a Glass-

PDMS-Glass Microchip via Bead-Assisted Acoustic Differential Extraction. *Anal Chem* **2019**, *91* (3), 2186–2191. https://doi.org/10.1021/acs.analchem.8b04752.

56. Birch, C.; Landers, J. P. Electrode Materials in Microfluidic Systems for the Processing and Separation of DNA: A Mini Review. *Micromachines (Basel)* **2017**, *8* (3), 76. https://doi.org/10.3390/mi8030076.

57. Jackson, K. R.; Borba, J. C.; Meija, M.; Mills, D. L.; Haverstick, D. M.; Olson, K. E.; Aranda, R.; Garner, G. T.; Carrilho, E.; Landers, J. P. DNA Purification Using Dynamic Solid-Phase Extraction on a Rotationally-Driven Polyethylene-Terephthalate Microdevice. *Anal Chim Acta* **2016**, *937*, 1–10. https://doi.org/10.1016/j.aca.2016.06.036.

58. Kloosterman, A.; Mapes, A.; Geradts, Z.; van Eijk, E.; Koper, C.; van den Berg, J.; Verheij, S.; van der Steen, M.; van Asten, A. The Interface between Forensic Science and Technology: How Technology Could Cause a Paradigm Shift in the Role of Forensic Institutes in the Criminal Justice System. *Philosophical Transactions of the Royal Society B: Biological Sciences* **2015**, *370* (1674), 20140264. https://doi.org/10.1098/rstb.2014.0264.

59. Lorenz, T. C. Polymerase Chain Reaction: Basic Protocol Plus Troubleshooting and Optimization Strategies. *J Vis Exp* **2012**, No. 63, 3998. https://doi.org/10.3791/3998.

60. *PCR Basics - US*. https://www.thermofisher.com/us/en/home/life-science/cloning/cloning-learning-center/invitrogen-school-of-molecular-biology/pcr-education/pcr-reagents-enzymes/pcr-basics.html (accessed 2022-07-14).

61. *PCR Basics*. https://www.thermofisher.com/us/en/home/life-science/cloning/cloning-learning-center/invitrogen-school-of-molecular-biology/pcr-education/pcr-reagents-enzymes/pcr-basics.html (accessed 2022-07-09).

62. Cadd, S.; Islam, M.; Manson, P.; Bleay, S. Fingerprint Composition and Aging: A Literature Review. *Sci. Justice* **2015**, *55* (4), 219–238. https://doi.org/10.1016/j.scijus.2015.02.004.

63. Brunelle, E.; Huynh, C.; Alin, E.; Eldridge, M.; Le, A. M.; Halámková, L.; Halámek, J. Fingerprint Analysis: Moving Toward Multiattribute Determination via Individual Markers. *Anal.Chem.* **2018**, *90* (3), 2401–2401. https://doi.org/10.1021/acs.analchem.8b00039.

64. Ferguson, L. S.; Wulfert, F.; Wolstenholme, R.; Fonville, J. M.; Clench, M. R.; Carolan, V. A.; Francese, S. Direct Detection of Peptides and Small Proteins in Fingermarks and Determination of Sex by MALDI Mass Spectrometry Profiling. *Analyst* **2012**, *137* (20), 4686–4692. https://doi.org/10.1039/C2AN36074H.

65. González, M.; Gorziza, R. P.; de Cássia Mariotti, K.; Pereira Limberger, R. Methodologies Applied to Fingerprint Analysis. *J. Forensic Sci.* **2020**, *65* (4), 1040–1048. https://doi.org/10.1111/1556-4029.14313.

66. Li, Z.; Bai, Y.; You, M.; Hu, J.; Yao, C.; Cao, L.; Xu, F. Fully Integrated Microfluidic Devices for Qualitative, Quantitative and Digital Nucleic Acids Testing at Point of Care. *Biosensors and Bioelectronics* **2021**, *177*, 112952. https://doi.org/10.1016/j.bios.2020.112952.

67. Harpaldas, H.; Arumugam, S.; Rodriguez, C. C.; Kumar, B. A.; Shi, V.; Sia, S. K. Point-of-Care Diagnostics: Recent Developments in a Pandemic Age. *Lab Chip* **2021**, *21* (23), 4517–4548. https://doi.org/10.1039/D1LC00627D.

68. Bhattacharjee, G.; Maurya, R.; Alzahrani, K. J.; Gohil, N.; Lam, N. L.; Singh, V. Chapter Eight - Microfluidics Based Point-of-Care for Disease Diagnostics. In *Progress in Molecular Biology and Translational Science*; Pandya, A., Singh, V.,

Eds.; Micro/Nanofluidics and Lab-on-Chip Based Emerging Technologies for Biomedical and Translational Research Applications - Part B; Academic Press, 2022; Vol. 187, pp 241–248. https://doi.org/10.1016/bs.pmbts.2021.07.024.

69. *Point-of-Care Testing: One Solution to Global Healthcare*. https://www.globalpointofcare.abbott/en/products-solutions/solutions.html (accessed 2022-07-26).

70. Wynberg, E.; Cooke, G.; Shroufi, A.; Reid, S. D.; Ford, N. Impact of Point-of-Care CD4 Testing on Linkage to HIV Care: A Systematic Review. *J Int AIDS Soc* **2014**, *17* (1), 18809. https://doi.org/10.7448/IAS.17.1.18809.

71. Gubala, V.; Harris, L. F.; Ricco, A. J.; Tan, M. X.; Williams, D. E. Point of Care Diagnostics: Status and Future. *Anal. Chem.* **2012**, *84* (2), 487–515. https://doi.org/10.1021/ac2030199.

72. Valera, E.; Jankelow, A.; Lim, J.; Kindratenko, V.; Ganguli, A.; White, K.; Kumar, J.; Bashir, R. COVID-19 Point-of-Care Diagnostics: Present and Future. *ACS Nano* **2021**, *15* (5), 7899–7906. https://doi.org/10.1021/acsnano.1c02981.

73. Urdea, M.; Penny, L. A.; Olmsted, S. S.; Giovanni, M. Y.; Kaspar, P.; Shepherd, A.; Wilson, P.; Dahl, C. A.; Buchsbaum, S.; Moeller, G.; Hay Burgess, D. C. Requirements for High Impact Diagnostics in the Developing World. *Nature* **2006**, *444* (1), 73–79. https://doi.org/10.1038/nature05448.

74. Tsaloglou, M.-N.; Watson, R. J.; Rushworth, C. M.; Zhao, Y.; Niu, X.; Sutton, J. M.; Morgan, H. Real-Time Microfluidic Recombinase Polymerase Amplification for the Toxin B Gene of Clostridium Difficile on a SlipChip Platform. *Analyst* **2014**, *140* (1), 258–264. https://doi.org/10.1039/C4AN01683A.

75. Lee, S. H.; Park, S.-M.; Kim, B. N.; Kwon, O. S.; Rho, W.-Y.; Jun, B.-H. Emerging Ultrafast Nucleic Acid Amplification Technologies for Next-Generation Molecular Diagnostics. *Biosens Bioelectron* **2019**, *141*, 111448. https://doi.org/10.1016/j.bios.2019.111448.

76. Li, X.; Tian, J.; Shen, W. Thread as a Versatile Material for Low-Cost Microfluidic Diagnostics. *ACS Appl. Mater. Interfaces* **2010**, *2* (1), 1–6. https://doi.org/10.1021/am9006148.

77. Yew, C.-H. T.; Azari, P.; Choi, J. R.; Li, F.; Pingguan-Murphy, B. Electrospin-Coating of Nitrocellulose Membrane Enhances Sensitivity in Nucleic Acid-Based Lateral Flow Assay. *Analytica Chimica Acta* **2018**, *1009*, 81–88. https://doi.org/10.1016/j.aca.2018.01.016.

78. *Virus Capture Kits | Ceres Nanosciences, Inc. | United States*. Ceres Nano. https://www.ceresnano.com/viruscapture (accessed 2022-07-26).

79. Nouwairi, R. L.; Cunha, L. L.; Scott, O.; Hickey, J.; Thomson, S.; Knowles, S.; Chapman, J.; Landers, J. P. Ultra-Rapid Real-Time Microfluidic RT-PCR Instrument for Nucleic Acid Analysis. *Lab Chip* **2022**.

80. Arena, F.; Pollini, S.; Rossolini, G. M.; Margaglione, M. Summary of the Available Molecular Methods for Detection of SARS-CoV-2 during the Ongoing Pandemic. *International Journal of Molecular Sciences* **2021**, *22* (3). https://doi.org/10.3390/ijms22031298.

81. Aaron Goutte; Tasha M Santiago-Rodriguez; Heather L Fehling; Rafal Iwasiow. Detection of SARS-CoV-2 in Saliva Using Tailed Amplicon Sequencing. *Journal of Infectious Diseases & Therapy* **2021**, *9* (4). https://doi.org/10.4172/2332-0877.1000464.

82. Barat, B.; Das, S.; De Giorgi, V.; Henderson, D. K.; Kopka, S.; Lau, A. F.; Miller, T.; Moriarty, T.; Palmore, T. N.; Sawney, S.; Spalding, C.; Tanjutco, P.; Wortmann, G.; Zelazny, A. M.; Frank, K. M. Pooled Saliva Specimens for SARS-CoV-2 Testing. *Journal of Clinical Microbiology* **2021**, *59* (3), e02486-20. https://doi.org/10.1128/JCM.02486-20.

83. Marshall, J. S.; Turiello, R.; Cunha, L. L.; Frazier, E. V.; Hickey, J.; Chapman, J.; Poulter, M. D.; Fehling, H. L.; Landers, J. P. Rapid SARS-CoV-2 Virus Enrichment and RNA Extraction for Efficient Diagnostic Screening of Pooled Nasopharyngeal or Saliva Samples for Dilutions Up to 1:100. *Diagnostics* **2022**, *12* (6). https://doi.org/10.3390/diagnostics12061398.

84. Han, P.; Ivanovski, S. Saliva—Friend and Foe in the COVID-19 Outbreak. *Diagnostics* **2020**, *10* (5). https://doi.org/10.3390/diagnostics10050290.

2. The Application of Microfluidic Technologies to the Identification of Biological Sex by Analysis of Latent Fingermark Deposits

2.1. Introduction

Fingerprint analysis is an indispensable tool used in forensic and criminal investigations. Despite the emergence of state-of-the-art DNA analysis technologies, it was reported that fingerprints outperform these and other comparable identification systems in the discernment of dangerous offenders.[1] Another pertinent example of the indispensability of these analyses is the discovery that identical twins have discernible fingerprints despite possessing indistinguishable DNA genetic profiles.[2] Such a distinction supports the premise that fingerprints serve as an invaluable investigative tool. Although the biometric analysis of the physical fingerprint pattern is quite prevalent, there has been significantly less research regarding the potential use of fingerprints as biological samples compared to other body fluids such as blood or saliva. Development in fingerprint analysis has primarily been confined to visual or digital comparison and matching of prints for approximately the past 110 years. Conversely, research regarding the viability of fingermarks as biological samples has only become prevalent in the last decade.[3,4]

When considering the use of fingerprints in this capacity, it is essential to note the distinction between the common term “fingerprint” and a term often used in the forensic community in such cases, “fingermark”. Fingerprints refer to the unique, physical pattern emplaced following contact between the finger’s papillary skin and another surface. Fingermarks are the “biological material transferred from the surface of the skin to another surface on contact”.[5,6] Latent fingermarks and fingerprints refer to those which are poorly

visible or undetectable to the unaided eye but can be developed for analysis. This inherent difference can serve to address the deficiencies of current fingerprint analysis techniques.[7]

Latent fingermarks are primarily comprised of sweat secretions from the sebaceous and eccrine glands and incorporate many metabolites from hormone-regulated metabolic mechanisms.[3] These metabolites can then be regarded as biomarkers or indicators of other physical and physiological properties such as age, ethnicity, health status, and biological sex.[3,8]

Traditionally, fingermark development has primarily been achieved using colored dyes or stains. The methods implemented typically require chemical development in a laboratory and are not used at a crime scene.[9] The treatment employed is usually dependent on the deposition surface. For porous samples like paper or cardboard, liquid chemical treatments such as 1,2-diazafluoren-9-one (DFO) development and the well-known ninhydrin are most often used.[9,10] The ninhydrin method has been used in federal, city, and state crime laboratories for almost 50 years. However, an inherent drawback of this reaction is that the end-product, diketohydrindylidene-diketohydrindamine (DYDA) or Ruhemann's purple, may also be developed from other α-NH2 compounds such as ammonium salts. This cross-reactivity gives rise to the potential for interference.[10] In cases where fingermarks are deposited on smooth, non-porous surfaces, development is often achieved using cyanoacrylate (commonly known as superglue) vapor or vacuum-metal deposition.[9] These chemical techniques discern the latent fingermark but do not provide detailed biological information about its content.

To date, most studies in this area of fingermark analysis have been conducted using spectrophotometric methods.[3,5] One such example is the successful development of

chemical and enzymatic assays targeting amino acids present in fingermarks for use as biomarkers by Brunelle et al.[3,4,10,11] Specifically, determination of the biological sex of the fingermark originator has been identified as a means of linking a specific analyte to one originator attribute. This differentiator was intended to serve as a basis for the eventual expansion of the protocol to include the identification of multiple characteristics via individual markers or analytes.[4] In this study, detection was achieved spectrophotometrically using UV–vis analysis. While there are many advantages inherent to spectrophotometric analysis regarding precision and sophistication, colorimeters are comparatively less expensive and can be more compact, mobile, and simple to operate.[12] As such, a rapid, inexpensive, simple, and portable device of this type for analysis of the biological contents of fingermarks would be beneficial for use at crime scenes.[4]

It is useful to note that although males are statistically more likely to be involved in criminal activities than women, research has persisted in this area for multiple reasons.[13] Firstly, it is believed that analysis of fingermark content can be instrumental in cases where there is no reference fingerprint in a database to which a crime scene fingerprint could be compared for individualization.[14] Additionally, analysis of deposits could provide biological information about the perpetrator in cases where there is distortion or deterioration of fingermarks.[14]

Chemical and enzymatic assays conducted in previous experiments have shown that females have an overall higher concentration of amino acids in their sweat than males.[3,4,15] In most cases, the concentrations of amino acids in the fingermarks of female origin are approximately twofold those obtained from males. As such, amino acid concentration in fingermark material can indicate the biological sex of the source.

Table 2-1. Average free amino acid concentration (µM) values for females and males derived from sweat. Adapted from Harker & Harding, 2013.[15] Eccrine sweat from 12 healthy volunteers was evaluated using ninhydrin derivatization followed by HPLC.

Amino Acid	Concentration (µM)		
	Females	Males	Δ Conc.
Alanine	387.0	196.8	190.2
Arginine	94.8	54.0	40.8
Asparagine	38.0	16.1	21.9
Aspartic acid	119.6	63.8	55.8
Citrulline	196.7	126.7	70.0
Cysteine	1.2	0.9	0.3
Glutamine	17.8	12.0	5.8
Glutamic acid	178.0	110.9	67.1
Glycine	646.3	341.8	304.5
Histidine	179.0	80.4	98.6
Isoleucine	49.4	22.9	26.5
Leucine	62.5	32.4	30.1
Lysine	52.8	28.5	24.3
Methionine	8.5	3.4	5.1
Ornithine	136.1	68.4	67.7
Phenylalanine	37.8	17.2	20.6
Proline	72.8	34.9	37.9
Serine	984.0	520.8	463.2
Threonine	209.0	112.1	96.9
Tryptophan	15.1	7.1	8.0
Tyrosine	55.9	30.3	25.6
Valine	91.9	45.9	46.0
β-alanine	12.8	3.4	9.4

While enzymatic assays present certain advantages such as specificity and sensitivity, there are also disadvantages inherent to using such methods. Enzymes are less stable than many chemical components and can have a limited shelf-life. Thus, carefully controlled storage conditions and more frequent replacements are required. Consequently, a specific and sensitive chemical assay is more widely applicable for detecting amino acids in fingermark content. One such chemical assay is the Sakaguchi Test for the detection of arginine.[16] In this test, arginine, sodium hypobromite, and α-naphthol react under alkaline conditions to produce a red-brown complex.[4,16] The intensity of the color is directly indicative of the concentration of arginine present in the sample.

This test is applicable in determining biological sex from fingermarks as the average concentrations of arginine in males' and females' sweat differ significantly. Males have an average concentration of 54.0 ± 12.61 µM (SEM). In contrast, in females, the average concentration in sweat is 94.8 ± 12.86 µM (SEM), as shown in **Table 2-1.** Herein, SEM refers to the standard error of the mean and is indicative of the dispersion of sample means around the population mean, thereby accounting for sample size.[17] In addition to having a satisfactory delta between male and female concentrations, arginine was selected as the basis of differentiation as there is a unique, specific, colorimetric test to determine

its presence. This characteristic interaction with 1-naphthol under the appropriate conditions is due to the guanidium moiety, highlighted in **Figure 2-1**. A definitive colorimetric result also allows for the analysis of results using open-source image analysis software, namely, the Fiji (Fiji Is Just ImageJ) distribution of ImageJ.[18,19] This protocol presents a lower-cost alternative to detection by UV–vis spectrophotometry. It is advantageous as the only requirements are the software (freeware) and a standard digital scanner. In concert with the scanner, the proposed microdevice measures the arginine content in fingermarks using non-enzymatic assays, thereby quickly and objectively determining unknown individuals' biological sex. We note that (to our knowledge) this is the first microfluidic device capable of facilitating objective, cost-effective analysis of fingermark deposits via optimization of the Sakaguchi reaction. Additionally, this technology can be further adapted to allow for an integrated, automated, and portable analysis system.

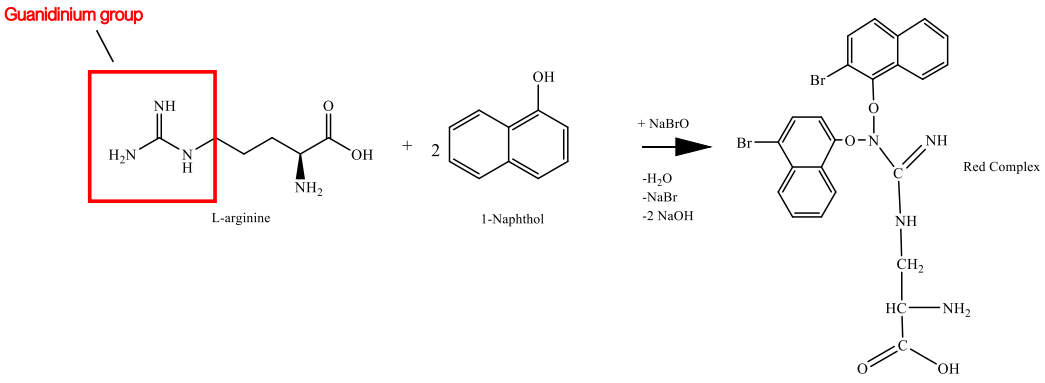

Figure 2-1. Overview of the Sakaguchi reaction. The guanidinium group in arginine which enables colorimetric detection s highlighted. This mechanism was created using ChemDraw, a registered trademark of Perkin Elmer Informatics.

2.2 Materials and Methods

2.2.1 Image Analysis

All images were analyzed using FIJI software. Following color development in each case, the detection domains were scanned using an Epson Perfection® V600 Photo Scanner (Epson America, Inc., Plainfield, IN, USA) and saved as TIFF files for image processing and analysis. Target segments were further isolated using the color thresholding feature of Fiji.[19,20] The images were first analyzed using the RGB (red, green, blue) color space, and results were generated in standard units in the 0 – 255 range. Images were then converted using the software's red to magenta conversion plugin and retested using the RGB color space. This step was followed by a conversion from the RGB to the HSB (hue, saturation, brightness) color space to analyze saturation. Results generated for saturation were reported as a percentage (0 –100%).

2.2.2 Proof of Concept—Sakaguchi Reaction and Modified Detection Method

Standard solutions with concentrations of 20, 40, 60, 80, 100, and 120 μM of L-arginine (Fisher Scientific, Hampton NH, USA) were prepared by dissolution in Millipore water. Stock solutions of 1.25 M and 2.50 M sodium hydroxide (Sigma-Aldrich, St. Louis, MO, USA) and 1.5 mM α-naphthol (Alfa Aesar, Haverhill, MA, USA) in 95% ethanol (v/v) (Sigma-Aldrich, St. Louis, MO, USA) were prepared. Additionally, a stock solution of sodium hypobromite was made by combining 32 μL of bromine (99+%, Acros Organics, Morris, NJ, USA) and 1.25 M sodium hydroxide to achieve a total volume of 5 mL. For each standard, 150 μL was added to a 1.5 mL centrifuge tube (USA Scientific, Inc., Ocala, FL, USA). This was followed by the addition of 30 μL each of 2.5 M sodium hydroxide

and 1.5 mM α-naphthol solutions as outlined by Huynh et al.[3.] There was a standard addition of 3.0 µL of 2.5 mM L-arginine to each reaction to facilitate measurable color development. The reactants in each tube were mixed using a vortex mixer (Vornado™ Miniature Vortexer, Benchmark Scientific, Sayreville, NJ, USA) and incubated at 4 °C for 5 min. Following incubation, 5 µL of sodium hypobromite was added to the centrifuge tube, the reaction mixture was vortexed, and the tubes were scanned before image analysis was performed.

2.2.3. Device Fabrication

The device was created using the Print, Cut, and Laminate (PCL) fabrication method previously developed by the Landers' lab.[21] The microfluidic device was first designed using Autodesk® AutoCAD® software, and the file was transferred to VersaLA-SER®VL3.50 software for the ablation of the design by the laser cutting instrument. Six layers comprised of black and transparent polyethylene (PET) (No Stripe Copier/Laser Transparency Film, Film Source Inc. (Tokyo Film Service Co. Ltd., Tokyo, Japan), heat-sealing adhesive (HSA) (Adhesives Research, Glen Rock, PA, USA), and polymethylmethacrylate (PMMA) (McMaster Carr, Santa Fe Springs, CA, USA). After programmed cutting of the layers, any extraneous obstructions remaining in the vents, channels, and inlets were removed using tweezers. The layers were combined using a custom alignment tool and laminated at 180 °C by passing the aligned structure through an office laminator (Akiles UltraLam 250 B). Several iterations of the microdevice were created using the same methodology before the optimal architecture was determined.

2.2.4. Fingermark Deposition and Arginine Extraction - Pilot Tests

Fingermark deposits were collected from volunteers who were assigned a reference code to protect their identities. Still, the biological sexes of the donors were known by the primary researcher to confirm proof of concept. Volunteers were asked to individually place their fingertips onto a designated area on PET transparency film (No Stripe Copier/Laser Transparency Film, Film Source Inc.) and directed to maintain contact for approximately 5 s. Fingermark deposits at this stage were "natural" as there were no specific preparatory instructions given to volunteers before the placement of deposits. The relevant segment of the transparency was then removed and placed in a 35 x 10 mm sterile polystyrene Petri dish (Falcon® Disposable Petri Dishes, Corning, NY, USA) and stored at ambient temperatures (~24 °C) for ≥ 24 h.

After storage, 120 µL of 0.01 M HCl (Fisher Scientific, Waltham, MA, USA) stock solution was placed directly onto the fingermark. The cover was replaced, and the dish was heated at 40 °C for 20 min using a hotplate/stirrer (VWR 4x4 Ceramic Hotplate/Stirrer 120 V). The sample solution was then transferred to the microfluidic device by pipetting 100 µL of this liquid from the transparency film surface. The Sakaguchi reaction was then initiated using 22 µL each of 2.5 M sodium hydroxide and 1.5 mM α-naphthol.[3,16] There was a standard addition of 3.0 µL of 2.5 mM L-arginine to each reaction to facilitate measurable color development. The contents of the mixing chamber were mixed using a custom-built stepper spin system (Sanyo Denki SANMOTION Stepper Motor, Parallax Propeller microcontroller) for 30 cycles at 1500 rpm. Mixing was facilitated by quick, repeated lateral rotations of the disc clockwise and anticlockwise enabled by the motor. The reaction mixture (on disc) was then incubated at 4 °C for 5 min. Following incubation,

the laser valve was breached via laser actuation using a Power and Time Adjustable Manual Laser (PTAML) (Thorlabs) (500 mW, 0.5 s). To initiate color development, sodium hypobromite (4 μL) was added to the microfluidic device's detection window. The device was then rotated using a custom spin system (E-flite Park 450 Spin System, Parallax Propeller microcontroller) at 2750 rpm for 15 s to allow for the metered transferal of 140 μL to the detection domain and mixing with sodium hypobromite. The detection window was then scanned, and the images were analyzed.

2.2.5. Lifted Deposits

The substrates chosen for deposition of fingermarks were a standard laminate benchtop and a stainless-steel light switch. The intended location of deposition was first sanitized using a 10% bleach solution. The area was then wiped with 90% ethanol and allowed to dry naturally. Donors deposited fingermarks on the relevant substrate, and a section of PET transparency film (~9 cm^2) was placed directly onto the deposits, with care taken to avoid sliding or smudging. As with the pilot tests, donors had no preparatory instructions before the fingermarks' deposition. When the PET film was securely in place, the pressure was carefully applied back and forth on the film's upper surface for 5 – 7 s to allow for the transferal of deposits. The PET film was carefully lifted from the surface using precision tweezers, inverted, and placed in a 35 mm borosilicate Petri dish. This Petri dish was stored at ambient temperature for ≥ 24 h before arginine extraction. Samples from matching donors were deposited directly onto PET film and used as controls.

2.2.6. Magnetically Powdered Deposits

Fingermarks deposited onto PET film were dusted using magnetic, bichromatic fingermark powder (Lynn Peavey Company, Lenexa, KS, USA). The excess powder was removed using a magnetic brush, and the samples were stored for ≥ 24 h at ambient temperature before arginine extraction. Following acid hydrolysis, the hydrolysate was transferred from the surface of the deposit to a centrifuge tube. A strong magnet was placed under the tube to promote the sedimentation of residual magnetic particles. A volume of 100 μL of the hydrolysate was then transferred to the microdevice to undergo the Sakaguchi reaction. Image and data analysis were subsequently executed. Duplicate samples from donors were deposited directly onto PET film and used as controls.

2.2.7. Blind Study

Volunteers were solicited from within the research group for the acquisition of fingermark deposits. There was no assigned ratio of biological sexes or prescribed age range. Volunteers were first asked to thoroughly wash their hands using a generic antibacterial soap, which was provided. Volunteers were then asked to place their hands in standard nitrile, unpowdered gloves. A designated colleague was present to ensure that there was no contact with extraneous surfaces such as stationary, taps, and gloves' outer surfaces. Subjects then placed their fingers firmly in designated slots on PET for 5 s each. The participants' biological sexes were withheld from the researcher conducting experiments until presumptive IDs of sample donors had been established.

2.3. Results and Discussion

2.3.1. Color Space Selection

Experiments were initially conducted in-tube to determine the feasibility of using the Epson V600 as the detector. Digital images obtained from the Epson V600 were analyzed using the FIJI image processing package.[18,19] The images were first examined based on the average "red value" of the RGB color space for each set of standards. It was presumed that since the resultant complex of the Sakaguchi reaction was red, the average red value from RGB would be proportional to the arginine concentration. **Figure 2-2.** depicts the poor linearity observed when increasing average red value was correlated to increasing concentration. This outcome suggested the potential for correlation but disqualified the independent use of this parameter as a viable indicator.

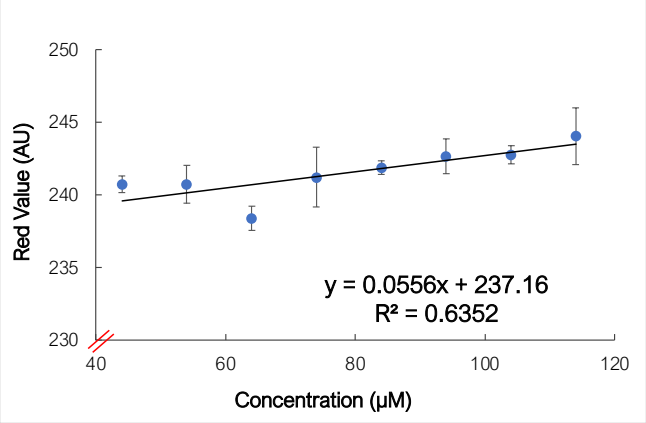

Figure 2-2. Results obtained from initial image analysis using the average red value as the metric. This metric was found to be non-ideal for this purpose given the poor correlation observed between arginine concentration and average red value ($n = 5$).

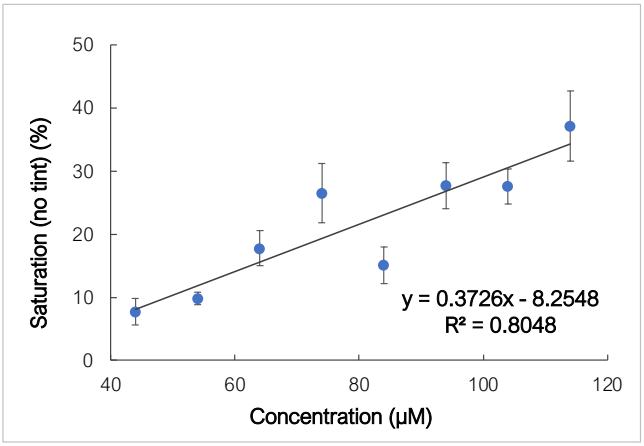

Figure 2-3. Results obtained from the initial image analysis using saturation as the metric. Although there was improvement in correlation of this value with arginine concentration, it was determined to be unsatisfactory. Images were tinted prior to saturation measurements thereafter to address this issue ($n = 5$).

As such, the data set was analyzed using the saturation parameter of the HSB color space. Following this change, a slightly

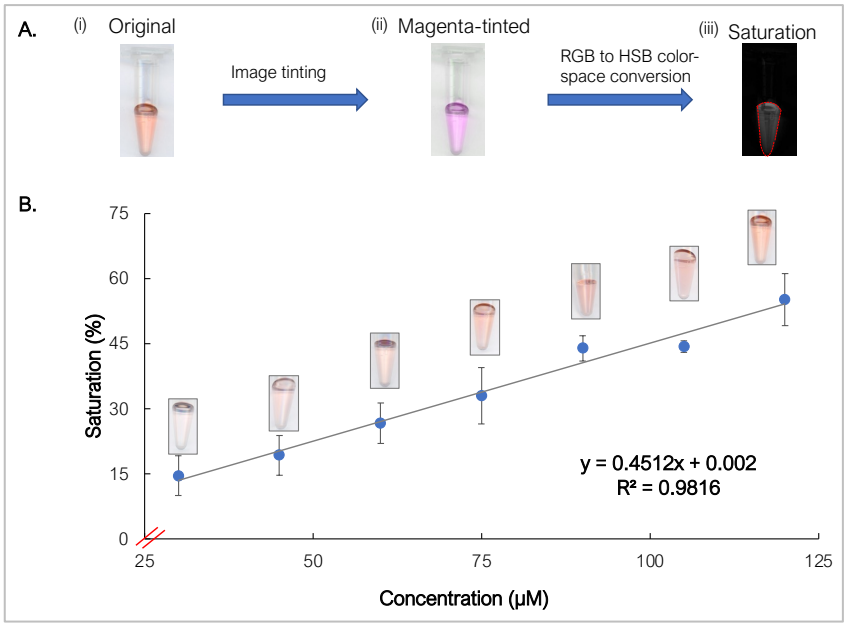

Figure 2-4. Illustration of results obtained in-tube using image-tinting techniques. (A)(i) shows a scanned image of a tube containing the complex formed after the Sakaguchi reaction was performed on a standard sample. The intensity of red color correlates directly to increasing arginine concentration. (ii) shows the image following red to magenta conversion in Fiji. Saturation (image shown in (iii)) was obtained using RGB (red, blue, green) to HSB (hue, saturation, brightness) color space conversion, resulting in a more linear relationship between saturation and concentration. (B) shows the curve obtained when concentration was correlated with saturation values following image-tinting ($n = 5$). The corresponding images obtained for each concentration are also depicted on this curve.

improved but non-ideal correlation between increasing concentration and saturation values was observed (**Figure 2-3**).

Given the improvements observed due to employing saturation measurement, the next step was to apply pre-existing image-tinting techniques previously developed in our lab to determine whether these were beneficial in this case.[22] Consequently, the red to magenta FIJI plugin was used before analyzing the average saturation values, as illustrated in **Figure 2-4A**.

In this conversion, the blue channel of the RGB color space is excluded and replaced with a second copy of the red channel. Additionally, occurrences of red in a red/green image are converted to magenta, creating a magenta/green merge.[23] This plugin was designed to accommodate individuals with red-green blindness and significantly enhance the red channel's contribution.[23] However, the adaptation of this feature for this

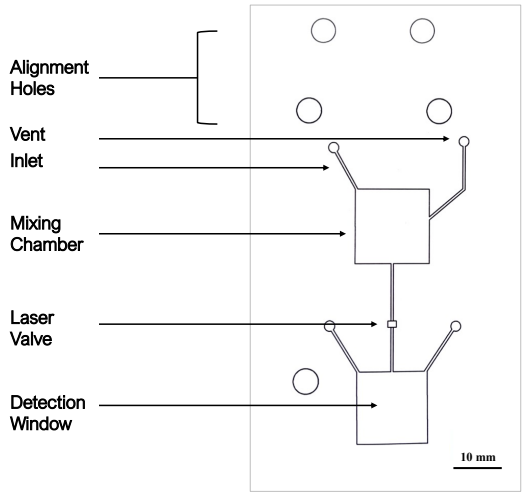

Figure 2-5. Schematic showing the initial architecture of the microdevice. This design was reevaluated due to the incomplete transfer of fluid from the mixing chamber to the detection window after centrifugal mixing of reagents.

purpose resulted in enhanced differentiation of shades of red. As a result, there was greater discernment of subtle differences in saturation, as shown by the plot obtained (**Figure 2-4B**). This combination of techniques was included in the image analysis stage of experiments thereafter.

2.3.2. Optimized Device Design

The next phase of this research entailed designing, optimizing, and fabricating a disc that best accommodates the image analyses as experimentally determined. Several iterations of microdevice architecture were evaluated before the optimized design of the centrifugal disc was determined.

Initially, to evaluate fluid flow, a rectangular chip featuring square chambers was created and applied to the analysis of mock samples (**Figure 2-5**). Mixing was enabled via spinning and shaking using the in-house rotational devices.

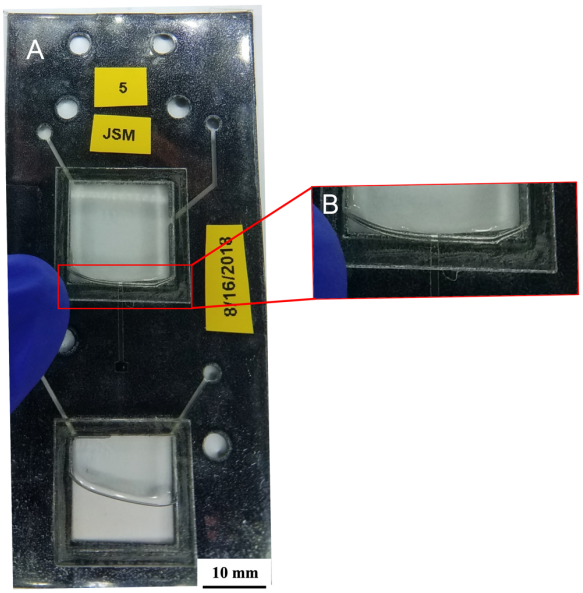

Figure 2-6. Image of original microdevice architecture and distribution of fluid following mixing via centrifugal rotation. (A) The assembled microdevice used for proof-of-concept experiments. (B) An enhanced view of the mixing chamber highlighting the liquid retained in the lower corners. This occurrence led to the redesign of the chamber shape and architecture.

Following preliminary experiments, it was determined that this architecture was not ideal as there was incomplete transferal of liquids from the first to the second chamber on spinning; fluid was retained in the lower corners of the first chamber, as shown in **Figure 2-6**. This could be attributed to the magnitude of the contact angle formed between the liquid and the inner surface of the chamber. The contact angle refers to the site at which a liquid-vapor interface interacts with a solid surface.[24] It has been established that the liquid is less likely to adhere to a solid surface as the contact angle increases. Pertinently, contact angles less than 90° are indicative of a hydrophilic interaction.[25] It thus follows that when the square architecture liquid adhered to the lower 90° corners of the mixing chamber after mixing via centrifugal rotation. Consequently, this architecture was supplanted by circular chambers in the optimized device.

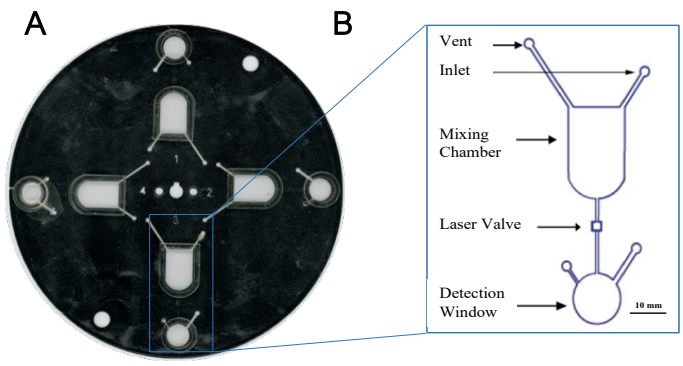

Figure 2-7. Optimized microfluidic disc. (A) shows a scanned image of the final version of the disc designed for these experiments. (B) is a magnified schematic of the architecture of each microfluidic domain as designed using AutoCAD® software. This disc was created using the Print, Cut, and Laminate technique previously developed by the Landers lab.[21]

The resulting optimized design of the device is shown in **Figure 2-7**. The disc features four discrete segments, each 90° to the neighboring section. The shape of the microdevice evolved from an initially rectangular architecture to a circular disc to maximize the benefits of centrifugal microfluidic mixing and facilitate multiple testing segments per disc. All iterations of the chip were five-layer devices with the addition of PMMA to increase the chamber depth and capacity and PET to cover the expanded chambers. The first uncoated PET layer defines the device's inlets, compartments, and vent holes. The second and fourth layers

demarcate the chambers and the channel barriers. The third toner-coated layer is a barrier between the second and fourth layers before the required fluid transfer between chambers following the actuation of the laser valve. The fifth layer covers exposed channels and chambers to create an enclosed system. Layers four and six are coated with a heat-sealing adhesive (HSA), which facilitates the binding of layers in the lamination process. Layer 7 is an uncoated PET layer that enables the use of the microdevice as a closed system. These layers are illustrated in **Figure 2-8**.

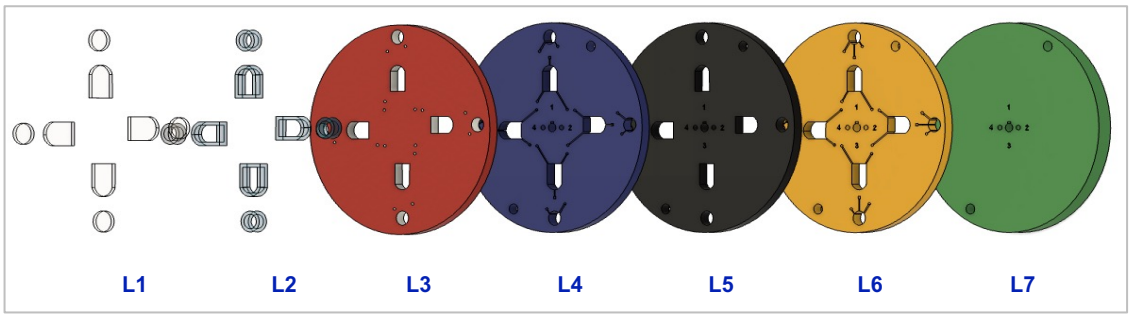

Figure 2-8. A schematic describing the individual layers of the microdevice used in these experiments. Layer (L) 1 is the polyethylene layer used to seal microfluidic chambers. L2 shows the poly(methyl methacrylate) (PMMA) segments used to increase the capacity of the fluidic chambers. L3 and L7 represent polyethylene (PE) layers. L4 and L6 represent polyethylene layers coated with heat-sealing adhesive (HSA) which is solvent-based, cross-linked, and purely acrylic. This allowed for cohesion within the microdevice. L5 represents a black PE layer which serves as a barrier between fluidic channels until laser actuation.

The reagents (2.5 M NaOH, 1.5 mM α-naphthol in ethanol) and sample or standard solutions are introduced via inlet to the mixing chamber, and mixing was via the external, centrifugal microfluidic system. The barrier was breached by melting the valve using a custom laser, followed by color development in the detection window as previously described. The generation of centrifugal forces promotes transfer through high-frequency, unidirectional rotations. **Figure 2-9** details a cross-section of the microdevice and illustrates how valve ablation facilitates fluid transfer.

The optimized microdevice was coupled with image analysis techniques to create a calibration curve. **Figure 2-10** illustrates the images obtained for the standards at each

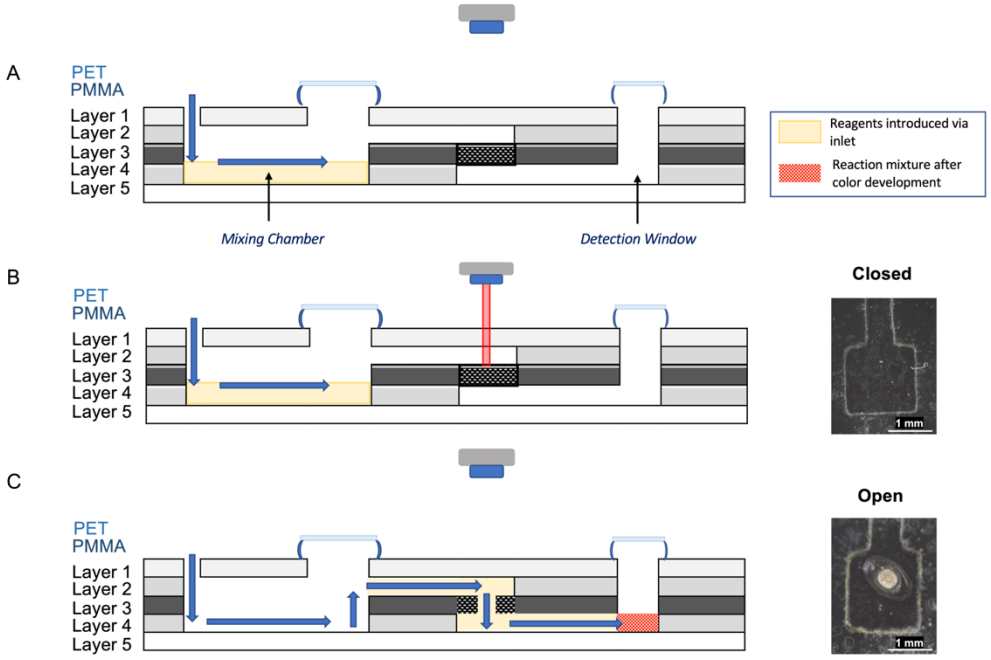

Figure 2-9. Lateral view of microdevice describing fluidic flow. (A) Reagents introduced via inlet, held in the mixing chamber by closed laser valve. Mixing occurs via bidirectional rotations using a custom-built spin system. (B)Laser valve absorbs energy from red laser ablation, creating access to next chamber. (C) Metered transfer of reactants to the second chamber where reagents are added for color development.

stage of image analysis – (A) shows the images immediately following color development

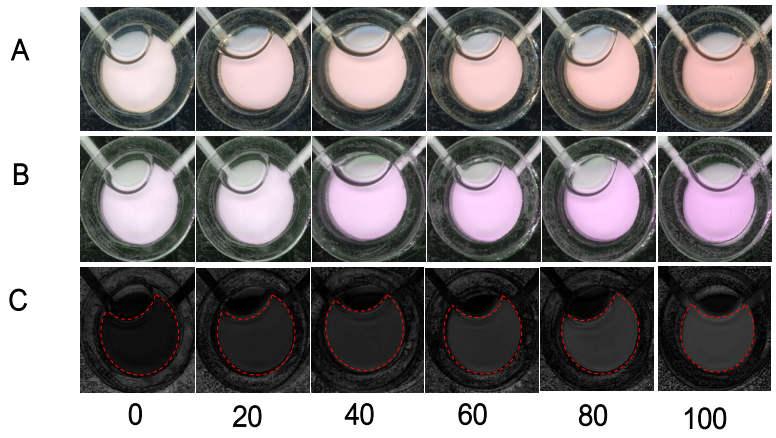

Figure 2-10. Illustrative images of detection windows. From left to right – the concentration of arginine increases as indicated by the corresponding increase in color intensity. Image analysis processing steps are depicted by row (A) the images before tinting, (B) the images following red to magenta conversion, and (C) RGB to HSB color space conversion.

and image acquisition, (B) shows the results of red to magenta tinting, and (C) exemplifies the final image obtained following RGB to HSB color space conversion. **Figure 2-11**

shows the robust and linear correlation between saturation and arginine concentration following this conversion, as evidenced by the marked improvement in the R squared value (0.635 for initial red channel measurements compared to 0.995 post-conversion).

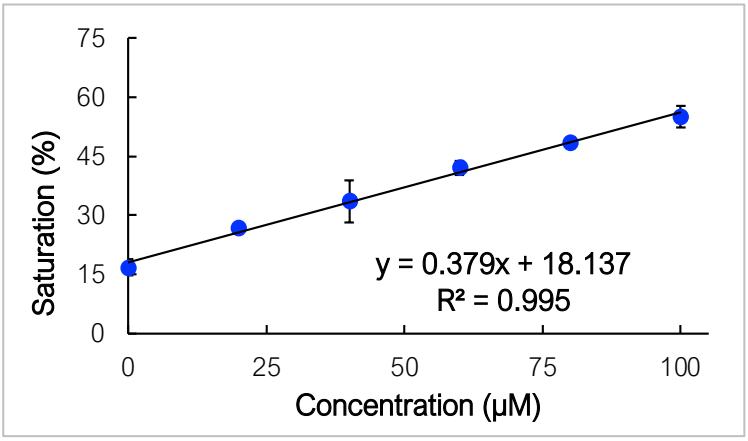

Figure 2-11. Calibration curve obtained using optimized microdevice. This curve demonstrates the strong, linear, correlation between saturation and concentration of arginine.

2.3.3. Pilot Tests

Subsequently, pilot experiments were conducted using a small number of donor samples (n = 7 for each biological sex). These samples were obtained via the voluntary donation of fingermark deposits from individuals of both biological sexes within the research group. As previously stated, volunteers were assigned a reference code to protect their identities, and there was no predetermined ratio of biological sexes. There was also no enrichment of fingermarks at this stage: no touching or rubbing of the nose or forehead before deposition. Omitting fingermark enrichment was intended to facilitate objective investigation of the potential to detect and analyze arginine content in non-ideal but realistic conditions. As such, data obtained would more closely approximate “natural” sweat content in deposits.

Additionally, a consistent delta was observed between mean thumb and "little" finger arginine concentrations compared to those obtained for the other fingers. It was determined that it would be prudent to focus analyses on the index, middle, and ring fingers. This delta was attributed to the difference in skin surface area in contact with the PET surface for the largest and smallest fingers.

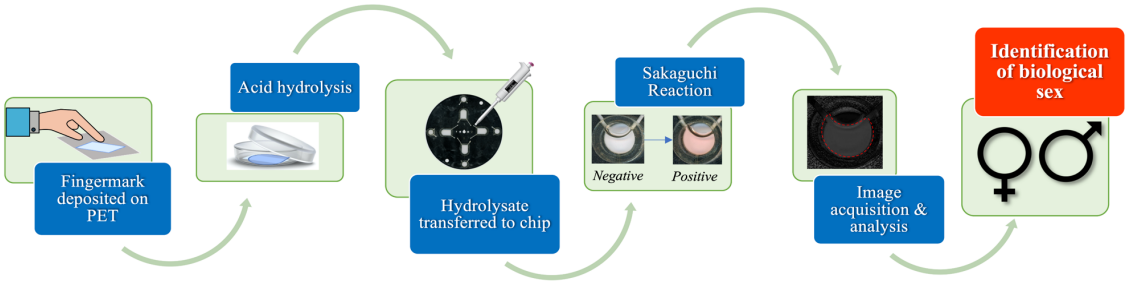

Figure 2-12. Schematic outlining the process used to analyze arginine content in donor fingermark deposits and consequently determine presumptive biological sex.

As illustrated in **Figure 2-12**, the deposits were first placed on PET squares and incubated before further analysis. Post-incubation processes were completed in ~40 min with the inclusion of the acid hydrolysis step (20 min). In the acid hydrolysis step, the hydrophilic components of the fingermark deposits, such as amino acids, proteins, and salts, migrate to the hydrochloric acid solution. The hydrophobic PET surface retains the lipophilic components derived from sebaceous secretions. These phenomena enable the extraction of arginine from the fingermark deposit matrix.

Following image and data analysis of all samples, the mean arginine concentrations obtained experimentally from males and females were compared to literature values and each other. These comparisons showed that there was no significant statistical difference. For males, the experimental mean obtained was 42.2 ± 4.4 µM, as compared to the theoretical value of 54.0 ± 12.6 µM.[15] For females, the mean arginine concentration obtained experimentally was 79.6 ± 4.3 µM, as compared to the literature value of 94.8 ±

12.9 µM.[15] The statistical similarities were confirmed for both data sets using the t-test. The p-value obtained when experimental values for female samples were compared to literature values was 0.256. When this comparison was analyzed for male samples, a p-value of 0.367 was obtained. Conversely, it was also determined that the mean arginine concentrations for male and female samples were significantly statistically different ($p < 0.001$). This information is summarized in **Figure 2-13**.

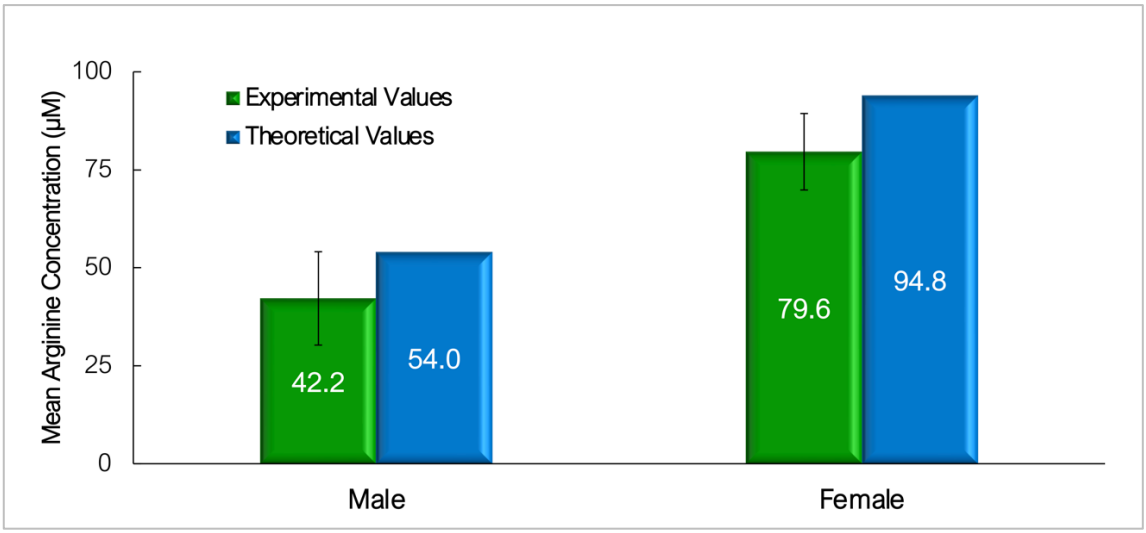

Figure 2-13. Literature values for mean arginine concentration vs. experimental values in pilot tests. The mean arginine concentrations of male and female samples were significantly different ($p < 0.001$). Experimental values obtained for males and females were not statistically different from literature values (males - 42.2 ± 4.4 vs. 54.0 ± 12.6 µM ($p = 0.367$); females - 79.6 ± 4.3 µM vs. 94.8 µM ± 12.9 ($p = 0.256$) (experimental vs. literature, ± SEM in all cases) ($n = 7$) [15].

2.3.4. Lifted Fingermark Deposits

In the pilot testing phase of these experiments, fingermarks were deposited on PET to evaluate the feasibility of the protocol and detection method. However, fingermarks are found on other substrates, such as wood, glass, doorknobs, laminate, or paper in a forensic investigation. Porosity, wettability, and other substrate characteristics play a significant role in forecasting the longevity and viability of deposits.[9,26] It has been experimentally determined that up to three times more amino acid material is found in sediments on porous

surfaces (e.g., paper and cardboard) than on non-porous substrates (e.g., glass and metal).[9] Eccrine sweat is more readily absorbed than sebaceous secretions and is thus more efficiently transferred onto porous substrates. Sebaceous secretions, however, can remain on the substrate surface for up to several years following deposition.[9] **Figure 2-14** illustrates the typical effects of substrate on the longevity of fingermark deposits (reprinted with permission).[26] Consequently, it was imperative to investigate this phenomenon under "real-world" conditions.

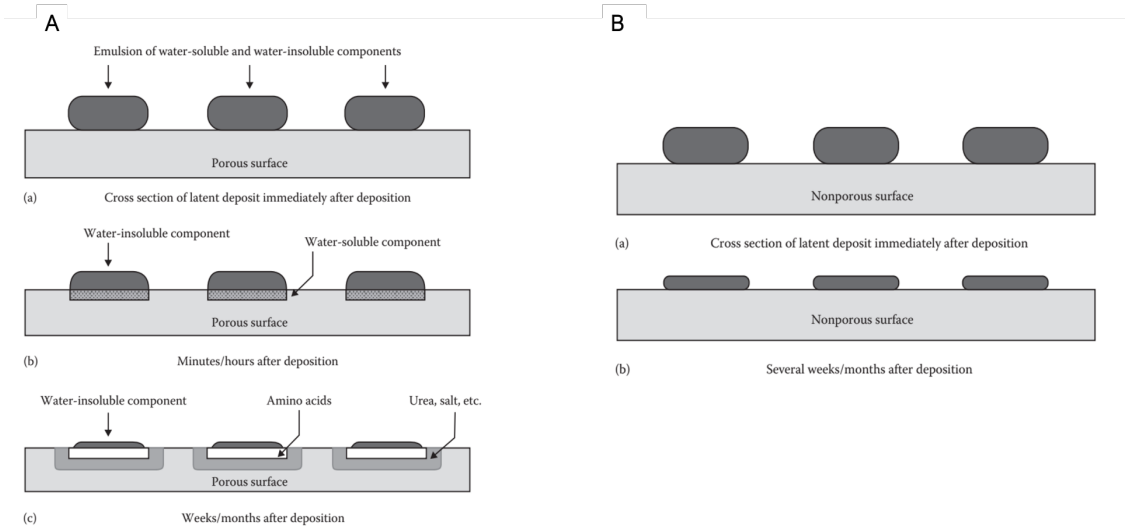

Figure 2-14. Depiction of the effect of surface porosity on the longevity of fingermark deposits after deposition. (A) illustrates the typical observations when fingermarks are deposited on porous surfaces, while (B) details fingermark behavior following deposition on nonporous surfaces [26].

The surfaces selected in this case were a laminate benchtop and a stainless-steel light switch cover. These were located in the research lab and chosen due to their non-porosity. It was presumed that the low-porosity substrates would create a realistic but non-ideal set of conditions in addition to being commonly accessed locations. Consequently, the robustness of the proposed modifications was also investigated. A schematic outlining the details of the lifting process is shown in **Figure 2-15**.

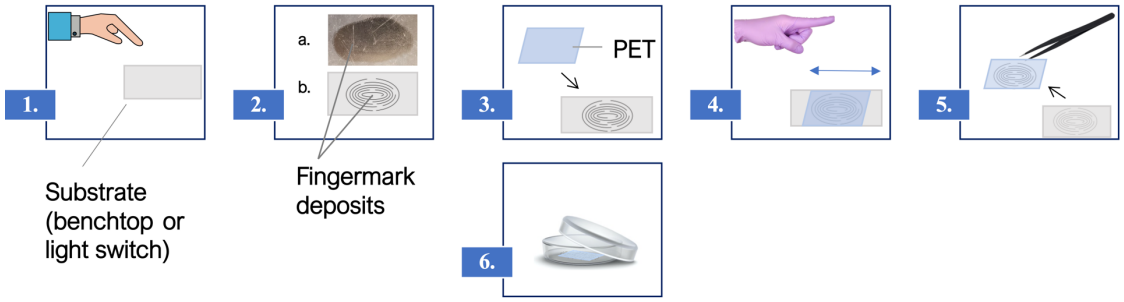

Figure 2-15. Schematic outlining the process used to obtain lifted fingermark deposits. (1) The donor deposited fingermarks on the appropriate substrate. (2) represents the fingermark deposits as they appear on the substrate, with (a) showing a digital image of a fingermark deposit on a benchtop as obtained in the experiments, and (b) showing a representative illustration. (3) A section of PET transparency film (~9 cm^2) was placed directly onto the deposits. (4) Pressure was carefully applied back and forth on the upper surface of the film to promote the transferal of deposits. (5) PET film was lifted from the surface using precision tweezers, inverted, and (6) placed in a 35 mm borosilicate Petri dish. Samples deposited directly on PET sheets were used as controls.

Given the paucity of arginine in fingermark deposits of male origin, it was probable that the inclusion of these samples could result in misleading results, whereby the scarcity of material would be incorrectly interpreted as an experimental design flaw or procedural failure. Consequently, proof-of-concept experiments were conducted using deposits from female donors only to reduce this uncertainty. This assertion was supported by Huynh et al., where the low signal from male fingermarks resulted in the use of deposits from females exclusively.[3] The results of this phase of tests are graphically displayed in **Figure 2-16**.

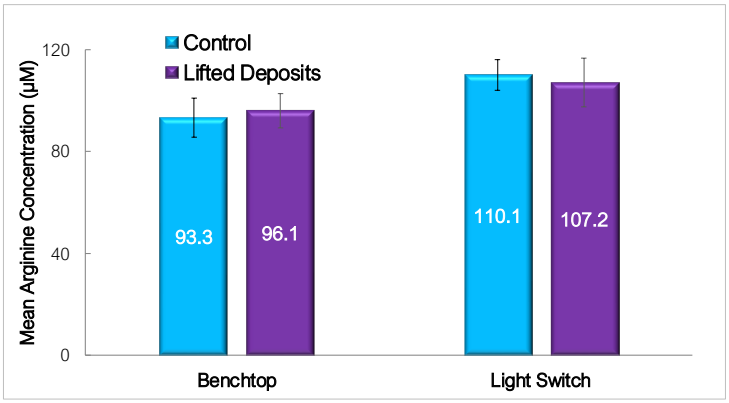

Figure 2-16. Comparison of the mean arginine concentrations obtained from lifted vs. control fingermark deposits (female donors). Samples deposited directly on PET sheets were used as controls (*n* = *3*).

It was observed that despite the variation of surfaces and the inclusion of lifting steps, there was no significant

statistical difference between arginine concentrations in lifted fingermark deposits and those deposited directly onto PET as controls. For samples lifted from the benchtop, the mean arginine concentration obtained was 96.1 ± 6.7 μM, compared to controls with a mean of 93.3 ± 7.7 μM ($p = 0.799$). The mean arginine concentrations obtained for samples lifted from the light switch were 107.2 ± 9.5 μM and 110.1 ± 6.0 μM for lifted and control samples, respectively ($p = 0.805$, $\alpha = 0.05$). All samples are reported with standard error measurements. It was also determined that the concentration means of the lifted benchtop samples and the lifted light switch samples were not significantly different ($p = 0.162$). These findings support the potential for applying the proposed protocol to crime scene forensic investigations.

2.3.5. Magnetically Powdered Fingermark Deposits

Powders have been described as "probably the oldest and most common techniques for the enhancement of latent fingerprints".[9] Fluorescent, magnetic, and carbon-based powders of various colors and compositions are routinely used to visualize latent prints at a crime scene. Given the inherently destructive nature of the proposed protocol, it was determined that the potential combination of techniques merited investigation. This combination would accommodate visualization of the print before experiments and chemical analysis, thereby allowing for the acquisition of both biometric and biochemical information. The bichromatic magnetic powder was chosen due to its sensitivity and potential to be visualized on both light and dark surfaces. Additionally, the excess powder can be removed using non-contact methods. This characteristic is beneficial as it reduces

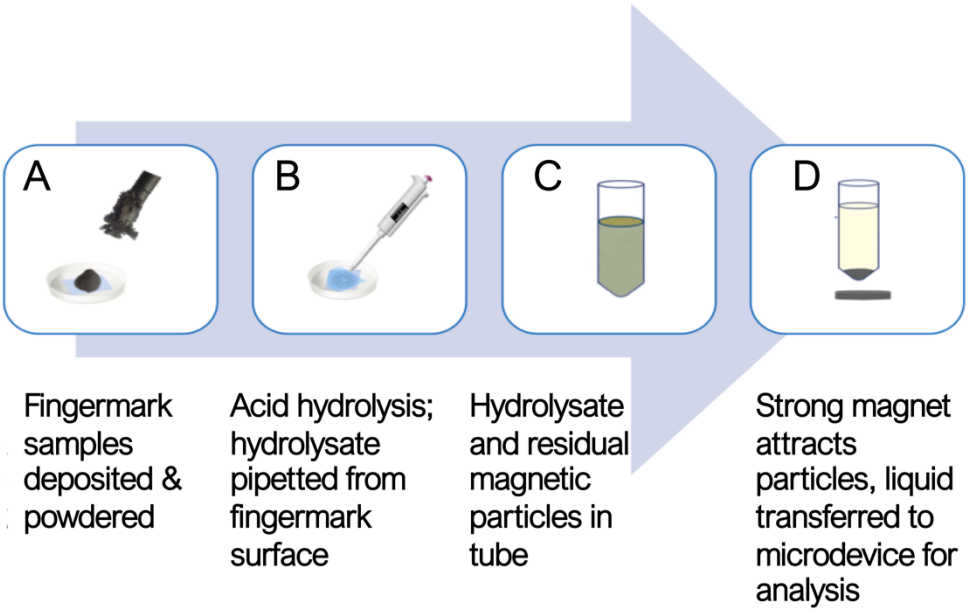

Figure 2-17. Summary of the process used to analyze magnetically- powdered samples. (1) Fingermarks were deposited on PET, placed in Petri dishes, and dusted using the magnetic powder and brush. Excess powder was removed from the deposits' surface before incubation. (2) Acid hydrolysis after incubation; hydrolysate then pipetted from the surface of the sample. (3) Mixture of residual magnetic particles and hydrolysate transferred to a centrifuge tube. (4) Strong magnet placed under the tube to promote sedimentation of the magnetic particles. Hydrolysate was then transferred to the microdevice and analyzed using the optimized protocol.

the chances of contamination or potential distortion of deposits. The process used for testing magnetically powdered fingermark deposits is described in **Figure 2-17**.

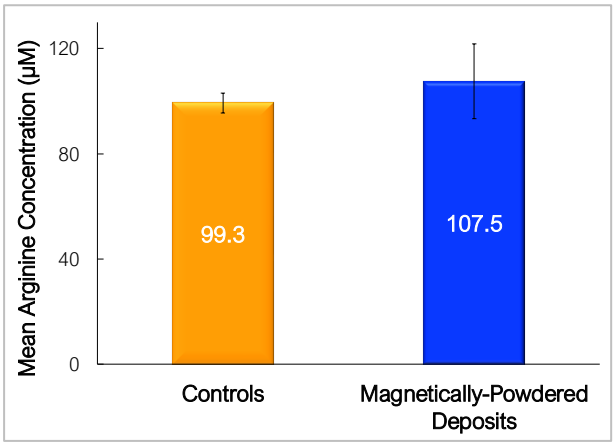

Figure 2-18. Comparison of mean arginine concentrations derived from magnetically powdered vs. control fingermark deposits from female donors. Controls were unpowdered samples deposited on PET sheets ($n = 6$).

It was determined that there was no significant difference between mean arginine concentrations obtained from magnetically powdered fingermark deposits and unpowdered controls deposited on PET ($p = 0.590$), as shown in **Figure 2-18**. Female donors were again used exclusively for these experiments to decrease the uncertainty

regarding experimental conditions. The results obtained suggest the potential for combining visualization techniques with the proposed protocol and optimized microdevice to acquire more information about potential perpetrators at a crime scene.

2.3.6. Blind Study

A blind study was conducted to analyze the robustness and applicability of the protocol conclusively. In the pilot testing phase of experiments, volunteers were assigned a reference code to protect their identities but were known to the researcher. For these experiments, however, the donors' biological sexes were recorded by a colleague for post-experimental verification and withheld from the primary analyst to preclude experimental bias. Biological sex was then presumptively proposed based on the results obtained and subsequently determined to be correct or incorrect.

Fingermark deposits were obtained from 16 unique participants. Of these, one set was rejected as there were no discernable prints or residues. As with the pilot study, five impressions were taken from each donor, but the thumb and little finger deposits were excluded due to inconsistent and erratic concentration values resulting from differences in

Table 2-2. Summary of results obtained from the blind study. The biological sexes of all participants were correctly determined except for one case.

Sample Number	Presumptive ID	Actual ID	Match (Yes / No)
1	Female	Female	Yes
2	Male	Male	Yes
3	Female	Female	Yes
4	Female	Female	Yes
5	Female	Female	Yes
6	Female	Female	Yes
7	Female	Female	Yes
8	Male	Male	Yes
9	Female	Female	Yes
10	Female	Female	Yes
11	Male	Male	Yes
12	Female	Female	Yes
13	Male	Female	No
14	Male	Male	Yes
15	Female	Female	Yes

finger sizes. Consequently, three prints each from eleven females and four males were analyzed, and the results obtained from these experiments are summarized in **Table 2-2**. The biological sexes of all participants were correctly determined except for one case. As such, the accuracy of discernment between biological sexes was fourteen of fifteen (93%).

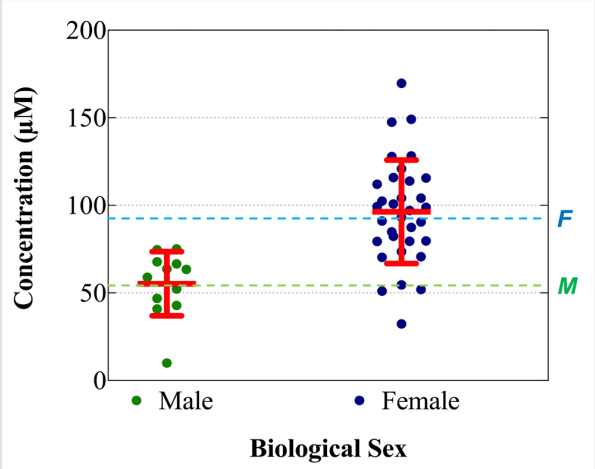

Figure 2-19. Comparison of mean arginine concentrations obtained from male vs. female individual samples in a blind study. These means were found to have a significant statistical difference ($p < 0.001$). For males ($n = 12$), the mean obtained was 55.26 ± 5.3 µM (SEM), which was not statistically different from the literature value, 54.0 ± 12.6 µM ($p = 0.914$) [15]. The mean concentration obtained experimentally for samples from female donors ($n = 33$), 96.4 ± 5.1 µM, was not statistically different from the literature value, 94.8 µM ± 12.9 ($p = 0.908$) [15]. The literature values are represented on the graph by green and blue broken lines for females and males, respectively. The gray dots represent values obtained for individual samples. The red dot represents the mean concentration obtained for each data set. The red horizontal lines represent the upper and lower bounds for the 95% confidence intervals.

The data from the blind study was further analyzed by comparison to known literature values. In this case, each deposit provided was enumerated to illustrate best the spread of data obtained, rather than evaluating data sets by the donor. This information is summarized in **Figure 2-19**. The arginine concentration means for males versus female donors in the study were significantly statistically different ($p < 0.001$). For males (*n = 12*), the mean arginine concentration obtained, 55.3 ± 5.3 µM was not statistically different from the literature value, 54.00 ± 12.61 µM ($p = 0.914$).[15] The mean arginine concentration obtained experimentally for samples from female donors, 96.4 ± 5.1 µM (*n = 33*), was not statistically different from the literature value, 94.80 ± 12.9 µM ($p = 0.908$).[15]

2.4. Conclusions

The creation of an optimized microfluidic device to identify biological sex via fingermark deposit analysis is detailed herein. These objectives were achieved by adapting and optimizing the colorimetric Sakaguchi reaction for a microfluidic platform coupled with an inexpensive but objective detection method employing freeware and a standard computer scanner. Jointly, these were used to reliably determine the donor's biological sex from fingermark content in ≤ 40 min (following incubation) with mean arginine concentrations that were statistically similar to those previously reported in the literature. The biological sexes of fourteen out of fifteen unknown participants were correctly designated via presumptive testing, demonstrating 93% accuracy of identification using the proposed protocol. Additionally, the compatibility of the proposed method with lifted samples and fingermarks treated with bichromatic magnetic powder was demonstrated. Given the inexpensive and rapid nature of testing methods and required equipment, the potential for reducing assay time, instrument expenditure, and consumption of reagents is evident.[27]

2.5. References

1. Cadd, S.; Islam, M.; Manson, P.; Bleay, S. Fingerprint Composition and Aging: A Literature Review. *Sci. Justice* **2015**, *55* (4), 219–238. https://doi.org/10.1016/j.scijus.2015.02.004.

2. Jain, A. K.; Prabhakar, S.; Pankanti, S. On the Similarity of Identical Twin Fingerprints. *Pattern Recognit.* **2002**, *35* (11), 2653–2663. https://doi.org/10.1016/S0031-3203(01)00218-7.

3. Huynh, C.; Brunelle, E.; Halámková, L.; Agudelo, J.; Halámek, J. Forensic Identification of Gender from Fingerprints. *Anal. Chem.* **2015**, *87* (22), 11531–11536. https://doi.org/10.1021/acs.analchem.5b03323.

4. Brunelle, E.; Huynh, C.; Alin, E.; Eldridge, M.; Le, A. M.; Halámková, L.; Halámek, J. Fingerprint Analysis: Moving Toward Multiattribute Determination via Individual Markers. *Anal.Chem.* **2018**, *90* (3), 2401–2401. https://doi.org/10.1021/acs.analchem.8b00039.

5. Ferguson, L. S.; Wulfert, F.; Wolstenholme, R.; Fonville, J. M.; Clench, M. R.; Carolan, V. A.; Francese, S. Direct Detection of Peptides and Small Proteins in Fingermarks and Determination of Sex by MALDI Mass Spectrometry Profiling. *Analyst* **2012**, *137* (20), 4686–4692. https://doi.org/10.1039/C2AN36074H.

6. González, M.; Gorziza, R. P.; de Cássia Mariotti, K.; Pereira Limberger, R. Methodologies Applied to Fingerprint Analysis. *J. Forensic Sci.* **2020**, *65* (4), 1040–1048. https://doi.org/10.1111/1556-4029.14313.

7. Kasper, S. *Latent Print Processing Guide*; Academic Press, an imprint of Elsevier: London, 2016.

8. A. J. Thody; S. Shuster. Control and Function of Sebaceous Glands. *Physiol. Rev.* **1989**, *69* (2), 383–416. https://doi.org/10.1152/physrev.1989.69.2.383.

9. Houck, M. *Forensic Fingerprints*; Houck, M., Ed.; Advanced Forensic Science Series; Academic Press, an imprint of Elsevier, 2016.

10. Brunelle, E.; Le, A. M.; Huynh, C.; Wingfield, K.; Halámková, L.; Agudelo, J.; Halámek, J. Coomassie Brilliant Blue G-250 Dye: An Application for Forensic Fingerprint Analysis. *Anal. Chem.* **2017**, *89* (7), 4314–4319. https://doi.org/10.1021/acs.analchem.7b00510.

11. Brunelle, E.; Huynh, C.; Le, A. M.; Halámková, L.; Agudelo, J.; Halámek, J. New Horizons for Ninhydrin: Colorimetric Determination of Gender from Fingerprints. *Anal. Chem.* **2016**, *88* (4), 2413–2420. https://doi.org/10.1021/acs.analchem.5b04473.

12. Firdaus, M. L.; Aprian, A.; Meileza, N.; Hitsmi, M.; Elvia, R.; Rahmidar, L.; Khaydarov, R. Smartphone Coupled with a Paper-Based Colorimetric Device for Sensitive and Portable Mercury Ion Sensing. *Chemosensors* **2019**, *7* (2), 25. https://doi.org/10.3390/chemosensors7020025.

13. *Uniform Crime Report Crime in the United States, 2019*.

14. van Helmond, W.; van Herwijnen, A. W.; van Riemsdijk, J. J. H.; van Bochove, M. A.; de Poot, C. J.; de Puit, M. Chemical Profiling of Fingerprints Using Mass Spectrometry. *Forensic Chemistry* **2019**, *16*, 100183. https://doi.org/10.1016/j.forc.2019.100183.

15. Harker, M.; Harding, C. R. Amino Acid Composition, Including Key Derivatives of Eccrine Sweat: Potential Biomarkers of Certain Atopic Skin Conditions. *Int. J. Cosmet. Sci.* **2013**, *35*, 163–168. https://doi.org/10.1111/ics.12019.

16. Sakaguchi, S. ÜBER EINE NEUE FARBENREAKTION von PROTEIN UND ARGININ. *J. Biochem* **1925**, *5* (1), 25–31. https://doi.org/10.1093/oxfordjournals.jbchem.a128359.

17. Altman, D. G.; Bland, J. M. Standard Deviations and Standard Errors. *BMJ* **2005**, *331* (7521), 903. https://doi.org/10.1136/bmj.331.7521.903.

18. Abramoff, M. D.; Magalhaes, P. J.; Ram, S. J. Image Processing with ImageJ. *Biophotonics Int.* **2004**, *11*, 36–42.

19. Schindelin, J.; Arganda-Carreras, I.; Frise, E.; Kaynig, V.; Longair, M.; Pietzsch, T.; Preibisch, S.; Rueden, C.; Saalfeld, S.; Schmid, B.; Tinevez, J.-Y.; White, D. J.; Hartenstein, V.; Eliceiri, K.; Tomancak, P.; Cardona, A. Fiji: An Open-Source Platform for Biological-Image Analysis. *Nat. Methods* **2012**, *9* (7), 676–682. https://doi.org/10.1038/nmeth.2019.

20. Woolf, M. S.; Dignan, L. M.; Scott, A. T.; Landers, J. P. Digital Postprocessing and Image Segmentation for Objective Analysis of Colorimetric Reactions. *Nat. Protoc.* **2021**, *16* (1), 218–238. https://doi.org/10.1038/s41596-020-00413-0.

21. Thompson, B. L.; Ouyang, Y.; Duarte, G. R. M.; Carrilho, E.; Krauss, S. T.; Landers, J. P. Inexpensive, Rapid Prototyping of Microfluidic Devices Using Overhead Transparencies and a Laser Print, Cut and Laminate Fabrication Method. *Nat. Protoc.* **2015**, *10* (6), 875–886. https://doi.org/10.1038/nprot.2015.051.

22. Krauss, S. T.; Nauman, A. Q.; Garner, G. T.; Landers, J. P. Color Manipulation through Microchip Tinting for Colorimetric Detection Using Hue Image Analysis. *Lab Chip.* **2017**, *17* (23), 4089–4096. https://doi.org/10.1039/C7LC00796E.

23. Schindelin, J. *Replace Red with Magenta*. https://imagej.net/Replace_Red_with_Magenta. (accessed 2019-01-14).

24. Saha, A. A.; Mitra, Sushanta K. Effect of Dynamic Contact Angle in a Volume of Fluid (VOF) Model for a Microfluidic Capillary Flow. *J Colloid Interface Sci.* **2009**, *339* (2), 461–480. https://doi.org/10.1016/j.jcis.2009.07.071.

25. Pratap, T.; Patra, K. Chapter 16 - Micro–Nano Surface Texturing, Characterization, and Their Impact on Biointerfaces. In *Advanced Machining and Finishing*; Gupta, K., Pramanik, A., Eds.; Elsevier, 2021; pp 577–610. https://doi.org/10.1016/B978-0-12-817452-4.00008-7.

26. Daluz, H. M. *Fundamentals of Fingerprint Analysis*, 2nd ed.; CRC Press: Boca Raton, 2018.

27. Marshall, J. S.; Sita, M. L.; Landers, J. P. Microfluidic Device for the Identification of Biological Sex by Analysis of Latent Fingermark Deposits. *Micromachines* **2021**, *12* (4). https://doi.org/10.3390/mi12040442.

3. A Rapid SARS-CoV-2 Virus Enrichment and Extraction Method for Efficient Diagnostic Screening via Largescale Pooling of Clinical Samples

3.1. Introduction

The novel Betacoronavirus severe acute respiratory syndrome coronavirus 2 (SARS-CoV-2) was identified in Wuhan, China, in December 2019 and quickly spread worldwide.[1,2] As of early January 2022, the coronavirus disease 2019 (COVID-19) pandemic has affected over 290 million people and caused more than 5.45 million deaths globally.[3] Several methods for sample collection and detection have emerged in recent months to address the increased demand for diagnostic laboratory testing, SARS-CoV-2 surveillance of asymptomatic persons, and to accommodate varying community needs.[4,5] Besides simply diversifying testing methodologies available, it is important that all novel approaches for coronavirus clinical testing are amenable to simple implementation, are relatively inexpensive, and are not prohibitively time-consuming.

With regard to sample collection and cellular lysis, the focus of diagnostic testing for SARS-CoV-2 has been on symptomatic persons via testing of upper respiratory specimens collected by swabs and extracted by a solid-phase approach.[4,5] While nasopharyngeal (NP) specimens continue to be the COVID-19 laboratory diagnostic standard, [6,7] saliva sampling has garnered significant attention as a low-cost, non-invasive alternative that affords comparable sensitivity for SARS-CoV-2 detection.[8] Furthermore, saliva specimens provide a more facile opportunity for pooled surveillance testing, a strategy proposed by several institutions for the monitoring of COVID-19 transmission.[9,10] Alternative viral lysis methods have also been demonstrated; notably, our group proposed a technique for SARS-CoV-2 nanoparticle-facilitated enrichment and enzymatic lysis from

clinical samples that leverages existing PDQeX technology in under 10 minutes.[11] This method demonstrated comparable sensitivity to gold-standard methods for RNA isolation from clinical samples and provided positive diagnoses from NP specimens and saliva collections.

Beyond sample collection and following lysis and isolation of viral RNA from swabs, reverse transcription-polymerase chain reaction (RT-PCR) is most commonly used for confirmatory detection and diagnosis of the virus. This approach is preferential over other molecular-based assays due to its capacity for sensitive and specific pathogen detection and potential for implementation with rapid diagnostic workflows.[12]

Microfluidic alternatives employing RT-PCR for detection and analysis are attractive for several reasons pertaining to the COVID-19 pandemic, as they permit rapid, automated, and streamlined detection.[13] Ideally, microfluidic detection would be coupled with upstream sample preparation within one integrated device; a miniaturized total analysis system (μTAS). However, this is less easily accomplished with large volume samples, such as those encountered with largescale pooling.[14]

Pooling is a sampling method whereby multiple specimens are combined into a "batch" or "pool", which is then analyzed using resources equivalent to those required for an individual test.[15] This minimizes the volumes of reagents used, lowers the cost per test, increases testing capacity, and decreases the required time investment for analyses.[16] It can be especially beneficial for largescale diagnostic screening in populations where the prevalence of the infection is low.[17] Additionally, it is a valuable tool for mitigating the spread of an illness in cases where patients are infected but asymptomatic.

Given the current steady decline in recorded cases,[18] a sensitive and rapid method for this application could be essential for efficient and accurate monitoring of infection rates. As such, a workflow for streamlined surveillance monitoring of SARS-CoV-2 with the potential for diagnosis from pooled clinical samples is detailed here. This methodology couples the ultrafast SARS-CoV-2 virus enrichment and extraction sample preparation technique optimized previously by our group with downstream detection of pooled samples by rapid microfluidic RT-PCR.[11] For proof-of-principle, downstream detection is accomplished by conventional RT-PCR using gold-standard instrumentation and kit chemistries given Emergency Use Authorization (EUA) by the Centers for Disease Control and Prevention (CDC). Additionally, microfluidic detection from pooled eluates using a custom-built RT-PCR instrument and corresponding microchips is demonstrated.[19] The presented workflow seeks to alleviate the macro-to-micro issues associated with microfluidic testing of pooled samples in a streamlined format, thereby promoting enhanced virus surveillance and decreased transmission rates.

3.2. Materials and Methods

3.2.1. Clinical SARS-CoV-2 Sample Preparation and Analysis

Three types of clinical samples were used in this study; samples derived from nasopharyngeal swabs stored in viral transport medium (VTM), neat saliva spiked with this VTM, and saliva samples collected, transported, and stored using DNA Genotek OMNIgene® ORAL (OME-505) device (DNA Genotek Inc., Ottawa, Ontario, Canada). Clinical VTM samples were analyzed via real-time RT-PCR using the Abbott M2000 Real-Time SARS-CoV-2 Assay (Abbott, Illinois, USA) or the Xpert® Xpress SARS-CoV-2

Assay (Cepheid, Sunnyvale, CA, USA) coupled with the Abbott M2000 Real-Time System (Abbott, Illinois, USA). Individual samples were then de-identified, assigned a sample code, and vortexed for 10 s before the transferal of a 0.6 - 1 mL aliquot to a pre-labeled, 2 mL screw-cap microcentrifuge tube. Aliquoted samples were inactivated via heat-treatment at 65 °C for 30 min and stored in a sealed, biohazard-designated zip-top bag at –20 °C until analysis. Neat (undiluted) saliva used for VTM spiking was diluted using a diluent buffer in a 1:3 ratio before use. The diluent buffer was prepared by first dissolving 3.3073 g NaCl, 0.0807 g KCl, 0.5678 g Na2HPO4, and 0.0978 g KH2PO4 in 40 mL of molecular biology grade water (Fisher Scientific, Pittsburgh, PA, USA) to obtain a 10X phosphate-buffered saline (PBS) solution. The pH of this solution was then adjusted to 7.35 using NaOH, and 200 µL of solution was combined with 1400 µL molecular biology grade water (Fisher Scientific) and 400 µL BLUE buffer (MicroGEM International, PLC., Charlottesville, VA, USA) to create the saliva dilution buffer. Saliva samples were obtained using the DNA Genotek OMNIgene® ORAL (OME-505) device for the stabilization of viral RNA in the CRL COVID-19 Self Collection Testing Kit from Clinical Reference Laboratory, Inc. (CRL, Lenexa, KS, USA. Initial COVID-19 testing conducted at CRL was performed using the CRL Rapid Response™ test with Emergency Use Authorization (EUA) granted by the FDA.[20] RNA extractions at CRL were conducted using the Zymo Quick-DNA/RNA™ Viral MagBead kit (Zymo Research Corporation, Irvine, CA, USA) on Tecan automated platforms (Tecan Life Sciences, Männedorf, Switzerland). RT-PCR was performed using the Logix Smart™ Coronavirus Disease 2019 (COVID-19) kit (Co-Diagnostics, Inc., Salt Lake City, UT, USA) using Bio-Rad CFX96™ Touch Real-Time PCR detection systems with Bio-Rad CFX Manager 3.1 software (Bio-

Rad Laboratories, Hercules, CA, USA). Before receipt by the University of Virginia Health System, saliva samples were de-identified according to HIPAA standards. Samples were shipped and stored at room temperature to best approximate "real-world" conditions; the self-collection system is reported to stabilize samples at room temperature for approximately 21 days.[21,22] There was no dilution of VTM clinical samples nor self-collected saliva samples before pooling and extraction.

3.2.2. Sample Pooling Protocol

Clinical SARS-CoV-2 samples were classified as having a "high", "moderate," or "low" viral titer based on the clinically detected C_T value from real-time RT-PCR. "High", "moderate", and "low" samples were those assigned C_T values of < 20, 20 - 30, and > 30, respectively. A sample pool was created for each classification by combining 250 µL each of three positive samples with similar C_T values to form a 750 µL bulk sample, as shown in the first step of **Figure 3-1A**. The appropriate volumes of these positive pools were then combined with negative clinical samples to achieve 1:10, 1:50, and 1:100 dilutions of positive bulk sample to negative sample (**Figure 3-1A**). This process was repeated without deviation for all clinical sample types analyzed.

3.2.3. RNA Extractions using the PDQeX Platform

Before extraction, samples were enriched via nanoparticle pre-concentration as described by Dignan et al.[11] Each dilution ratio was applied to a total volume of 500 µL; for example, 50 µL of positive pooled sample was added to 450 µL of negative clinical sample for the 1:10 dilution. The dilution setup and sample preparation workflow are

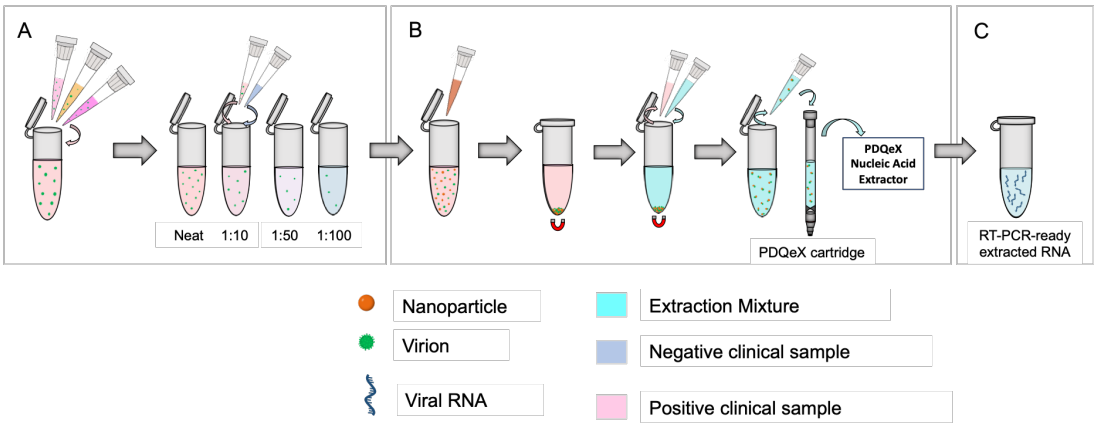

Figure 3-1. Schematic illustrating the workflow for sample preparation and RNA extraction. Based on the clinically assigned C_T value, samples (nasopharyngeal swabs in VTM, or saliva, as appropriate) were classified as having a high, moderate, or low viral titer (C_T value < 20, 20 – 30, or > 30, respectively). (A) Equal volumes of three positive samples with similar clinically assigned C_T values were combined to represent a pooled positive sample. The appropriate ratios were achieved by diluting this pooled positive sample in clinically negative samples. (B) SARS-CoV-2 virions were pre-concentrated using paramagnetic nanoparticles. This step facilitated the adsorption of virions to the nanoparticles, which were then magnetically separated from the sample. The supernatant was removed, and the extraction cocktail was added for the resuspension of nanoparticles. The desorption and extraction of RNA were then facilitated via thermocycling. This process was repeated for each dilution pool. (C) RT-PCR-ready extracted viral RNA.

illustrated in **Figure 3-1A**. Briefly, 100 µL of Nanotrap® Magnetic Virus Particles (CERES Nanosciences, Inc, Manassas, VA, USA) were added to each dilution pool, with thorough mixing via vortexing (**Figure 3-1B**). Per the manufacturer's recommendation, the supernatant was removed, and the extraction cocktail was added. The cocktail comprised 88 µL of nuclease-free water, 2 µL of RNAGEM (MicroGEM US Inc., Charlottesville, VA, USA), and 10 µL of 10 X BLUE Buffer (MicroGEM, Charlottesville, VA, USA). Following thorough mixing, the combined sample and extraction cocktail mixture was transferred to a PDQeX cartridge before thermocycling in the PDQeX Nucleic acid Extractor (MicroGEM, Charlottesville, VA, USA) at 95 °C for 5 minutes (**Figure 3-1B and C**). This process was repeated for each dilution pool. The extracts were then immediately analyzed via RT-PCR.

3.2.4. RT-PCR Conditions

The C_T data obtained from RT-PCR experiments were used to evaluate the relative success of upstream preparation and detection of SARS-CoV-2 viral RNA in pooled and diluted samples. The RT-PCR assay used was developed by the Centers for Disease Control and Prevention (CDC) under an emergency use authorization (EUA) in February 2020.[23] Each reaction was a total volume of 20 µL and was comprised of 5 µL of viral RNA extract, 5 µL of TaqPath™ 1-Step RT-q-PCR Master Mix (Thermo Fisher Scientific, Waltham, MA, USA), 1 µL of SARS-CoV-2 (2019-nCoV) CDC RUO N1 primer-probe mix (Integrated DNA Technologies, Coralville, IA, USA), and 9 µL of PCR-grade water. The 2019-nCoV_N_Positive Control plasmid (Integrated DNA Technologies, Coralville, IA, USA) was serially diluted to obtain concentrations of 1000, 100, 50, and 10 copies/µL and used as positive controls for real-time RT-PCR. Samples were run in either triplicate or quintuplicate using the suggested protocol for the TaqPath™ 1-Step RT-q-PCR Master Mix, including UNG incubation at 25 °C for 120 s, reverse transcription at 50 °C for 900 s, polymerase activation at 95 °C for 120 s, and 40 amplification cycles (95 °C for 3 s and 60°C for 30 s). Extracts and controls were analyzed using a QuantStudio™ 5 Real-Time PCR System for Human Identification (Applied Biosystems, Waltham, MA, USA).

3.2.5. Double-Blind Study – Clinical Saliva Samples

A double-blind study was conducted to assess the accuracy of qualitative differentiation between clinical positive and negative samples using the proposed pooling protocol while ensuring the absence of selection bias. Deidentified clinical negative and positive saliva samples (obtained using the OMNIgene®•ORAL self-collection system)

were randomly selected, analyzed via RT-PCR, and labeled with a numerical sample code at Clinical Reference Laboratory Inc. Samples were then shipped to the researchers at UVA for analysis. Each sample was then randomly assigned an in-house code (X1 – X10) which correlated to the numerical sample code provided by the third party. These samples were diluted to the appropriate ratios using negative saliva samples, as detailed in **Figure 3-1A**, before RNA extraction and RT-PCR analysis (**Figures 3-1B and C**). Presumptive results were then conveyed to the third party for comparison to known data.

3.2.6. Adaptation of Assay to an Ultra-Rapid Real-Time Microfluidic PCR Amplification Instrument

Preliminary experiments were conducted using clinical saliva samples to determine the feasibility of adapting the assay for use with a novel in-house PCR amplification instrument. Data from the in-house device was compared to conventional gold-standard techniques. Extraction was performed using the RNeasy Mini Kit (Qiagen, Valencia, CA, USA), and RT-PCR was performed utilizing the QuantStudio™ 5 Real-Time PCR System for Human Identification and the manufacturer's thermocycling protocol as previously described. Experiments were conducted in parallel using the PDQeX Nucleic Acid Extractor with Nanotrap® Magnetic Virus Particles enrichment for extraction, while PCR amplification was realized using the Ultra-Rapid Real-Time Microfluidic PCR Amplification instrument. TaqPath™ 1-Step RT-q-PCR Master Mix and SARS-CoV-2 (2019-nCoV) CDC RUO N1 primer-probe mix chemistry was used for both conventional and microfluidic RT-PCR.

Briefly, 300 µL were taken from each of four positive clinical saliva samples and combined to create a neat pool with an average reported C_T value of 21.7 ± 1.06 and a total volume of 1.2 mL. A 1:50 dilution pool was prepared from the amalgamated neat stock using negative saliva samples as diluent with a final volume of 600 µL. The neat and 1:50 pools were split equally, with half designated for conventional analyses and the remainder for use in microfluidic experiments. 250 µL each were taken from each pool and analyzed using conventional methods. Identical aliquots were analyzed using the microfluidic method described above. Negative saliva samples were included as controls, and the conventional RT-PCR was conducted according to the manufacturer's protocol as previously described. For microfluidic experiments, however, the thermocycling program comprised reverse transcription at 50 °C for 300 s, polymerase activation at 95 °C for 120 s, and 40 amplification cycles (95 °C for 1 s and 60°C for 15 s). Data obtained were analyzed and compared.

Regarding the operation of the instrument, real-time amplification was enabled by first mounting the reagent-filled microfluidic chip onto the alignment pegs and clamping it between the Peltiers as shown in **Figure 3-2** (detailed further in the following chapter).[19] A light-proof box was then placed over the instrument. The fluorescence detector was positioned orthogonally to the amplification chamber (**Figure 3-2B**) and Peltiers (**Figure 3-2C**) to detect laser-induced fluorescence (LIF) via a 488 nm sapphire laser while

simultaneously thermal cycling.[19] The system was coded to perform two-step PCR (denaturation and annealing) following an initial "synthesis" step.

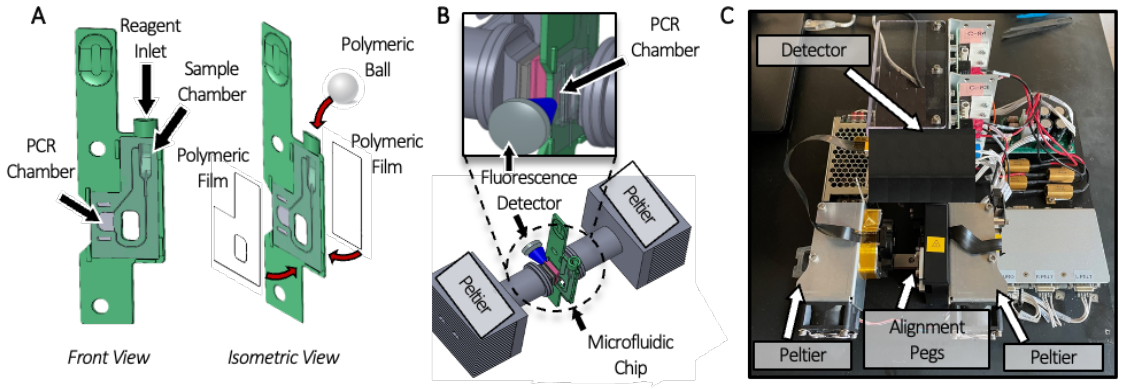

Figure 3-2. The microfluidic instrument used for rapid PCR analyses. (A) Front and isometric views of the microfluidic chip. (B) Schematic of the instrument with the fluorescence detector highlighted. (C) Custom instrument including alignment pegs used for chip placement and the clamping Peltiers. [19]

3.2.7. Statistical Analyses

All statistical analyses were conducted using GraphPad Prism version 9.3.1. (350) for macOS, GraphPad Software San Diego, California USA.[24]

3.3. Results

3.3.1. Pooling of Nasopharyngeal (VTM) Clinical Samples

Clinical nasopharyngeal (NP) samples classified as having 'high' and 'moderate' relative viral titers were pooled and prepared using the nanoparticle enrichment and enzymatic extraction protocol. A representative amplification plot from the RT-PCR analysis of extracted RNA from the high titer pool and the corresponding dilutions of this sample type is shown in **Figure 3-3**. The average C_T values for high and moderate pools are summarized in **Figure 3-4**. Amplification was observed for all dilutions in these sample

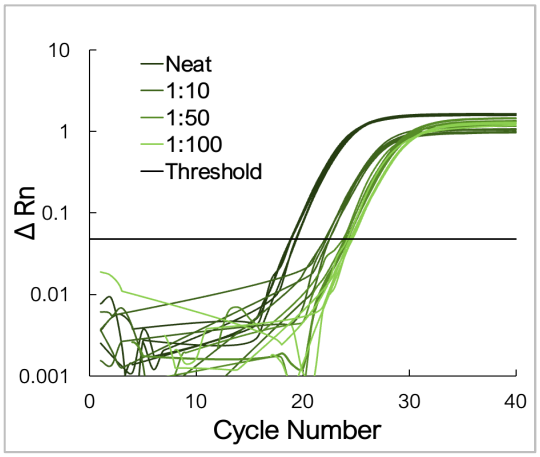

Figure 3-3. Amplification data obtained from pooling experiments using clinical nasopharyngeal swab samples. A representative normalized amplification plot obtained from RT-qPCR analysis of the extracted RNA (high viral titer) (*n* = *5*).

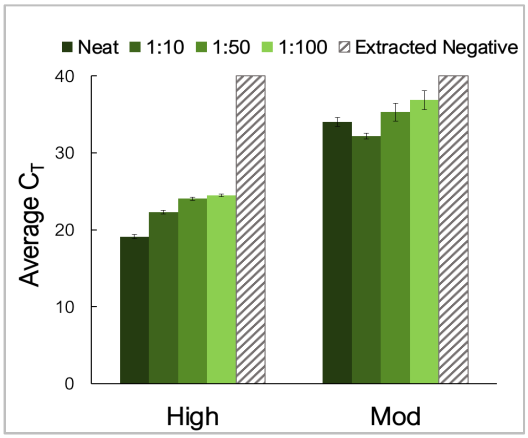

Figure 3-4. Summary of C_T data. Dilution ratios increase from left to right. Amplification was successful for all dilutions of high and moderate viral titer clinical samples (*n* = *5*).

pools. The average C_T values for high titer samples increased incrementally from 19.1 ± 0.27 for neat samples to 24.5 ± 0.17 for the most dilute pool (1:100). Average C_T values for moderate viral titer dilutions increased from 34.0 ± 0.58 for the neat samples to 36.9 for the 1:100 dilution. The C_T values for the 1:10 dilution were lower than those observed for the neat samples.

Tukey's multiple comparisons tests showed that despite this decrease, there was no significant difference between the C_T values obtained for neat samples compared to those obtained for 1:10 and 1:50 dilutions (p = 0.2040 and 0.0954, respectively).[24,25] No amplification was observed in the extracted negative samples, and these were assigned the maximum cycle value (40).

3.3.2. Spiking of Negative Saliva and Subsequent Pooling

Here, clinical NP samples of high and moderate concentrations were spiked into fresh saliva, pooled, and analyzed via the previously described protocol. A representative amplification plot from the RT-PCR analysis of extracted RNA from the high titer pool

and the corresponding dilutions of this sample type is shown in **Figure 3-5A**. The average C_T values for high and moderate pools are summarized in **Figure 3-5B**. There was successful amplification for all dilutions and viral titer designations following RT-PCR. Additionally, amplification was observed in the extracted negative samples, with an average C_T value of 38.7 ± 1.08.

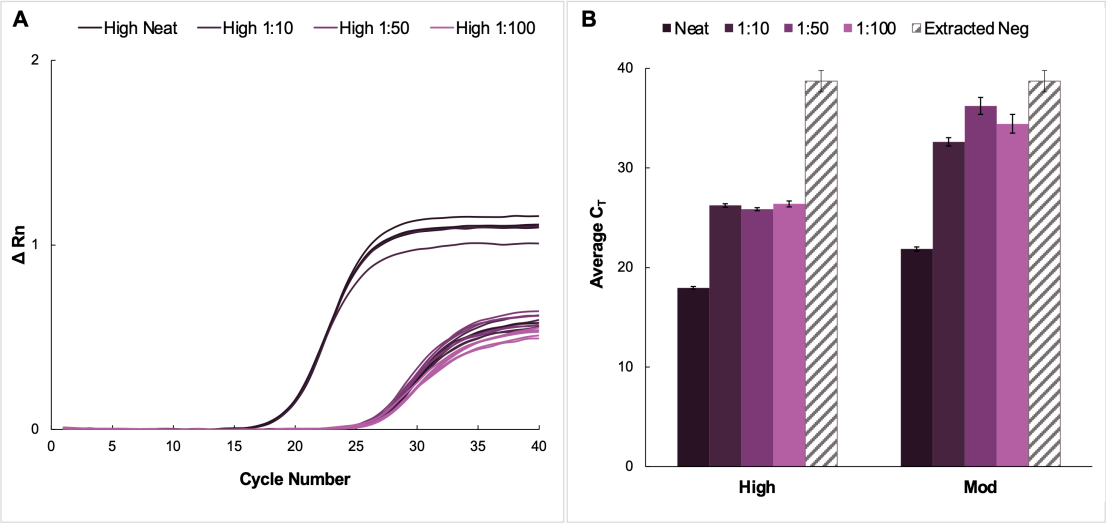

Figure 3-5. Amplification data obtained from pooling experiments using fresh saliva spiked with clinical nasopharyngeal swab samples. (A) A representative normalized amplification plot obtained from RT-PCR analysis of the extracted RNA (high viral titer). (B) A summary of the C_T data. Dilution ratios increase from left to right. In this case there was amplification in extracted negative samples (*n* = 5).

For high viral titer samples, there was an increase in C_T value when the dilution factor increased from 1:10 to 1:50 and a decrease for the 1:100 pool. Still, Tukey's multiple comparison test determined that though the data obtained for the 1:10 and 1:100 dilutions were statistically different ($p < 0.0001$), there was no significant difference between the average C_T values obtained for the 1:50 compared to the 1:100 dilutions ($p = 0.7520$).[24,25]

In the case of the moderate C_T samples, there was a significant increase in average C_T values for the diluted samples compared to the neat, from 21.9 ± 0.42 for the neat sample up to 34.4 ± 0.30 for the 1:100 dilution. This was followed by a rise in C_T values for the 1:50 dilution before a decrease in average C_T values for the 1:100 dilutions. Unlike the

high-titer samples, the average C_T values for all moderate dilution pools were found to be statistically different when compared using Tukey's test.[24,25]

3.3.3. Pooling of Saliva Samples

High, moderate, and low concentration clinical saliva samples obtained using the CRL COVID-19 Self Collection Testing Kit were pooled and prepared as described above. Amplification was observed for all samples and corresponding dilutions (**Figure 3-6**).

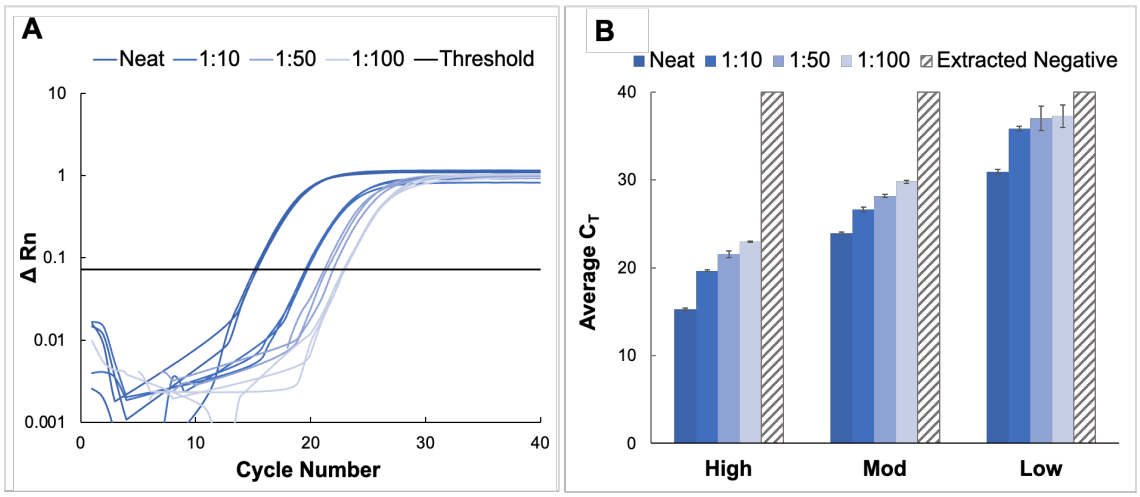

Figure 3-6. Amplification data obtained from pooling experiments using saliva samples collected using the CRL OMNIgene®•ORAL sampling kit. (A) A representative normalized amplification plot obtained from RT-PCR analysis of extracted RNA (high viral titer). (B) Summary of C_T data. Dilution ratios increase from left to right (*n = 3*).

C_T values increased by approximately four units for each viral titer (high, moderate, and low) when comparing neat samples to those diluted to the corresponding 1:10 dilutions; however, the deltas of the average C_T values decreased for dilutions beyond 1:10. Namely, C_T values increased by approximately 1.6 cycles between dilutions for high and moderate samples and between 0.27 and 1.2 cycles for low concentration samples. Overall, the average C_T value for low titer samples incrementally increased from 30.9 ± 0.28 for the neat sample to 37.3 for the 1:100 dilution.

Average C_T values ranged from 23.9 ± 0.13 for the neat sample to 29.8 ± 0.19 for the 1:100 dilution for moderate viral titer samples. As seen with the high titer samples, there was a consistent incremental increase in average C_T value as the negative to positive clinical sample ratio increased. It was determined using Tukey's test that the average C_T values for the high viral titer dilutions were statistically distinct from each other.[24,25] This was also true for the moderate viral titer pools. However, for low viral titer dilutions, it was determined that there was no statistical difference between means when the 1:50 dilutions were compared to those diluted to 1:100 ($p > 0.9999$).

3.3.4. Double-blind Study – Clinical Saliva Study

Clinical saliva samples obtained using CRL COVID-19 Self Collection Testing Kits were first analyzed at CRL, blinded, and then transferred to our lab to facilitate the double-blind study. Pooling, enrichment, and extractions were conducted in the same manner as described for samples of known viral concentrations. The presumptive qualitative diagnoses (positive or negative) for dilution pools created using each of 10 blinded samples were 100 % concordant with clinical results; five positive and five negative samples were accurately identified using the optimized pooling protocol. No amplification was observed in the samples which were later confirmed as negative.

The amplification results for positive samples pooled up to 1:100 are shown in **Figure 3-7**, along with the C_T value obtained from CRL following initial analyses at their location (depicted as a colored, shaded bar). For sample X2 (**Figure 3-7A**), the average C_T values obtained for the neat samples were ~1.5 cycles higher than the reported CRL value (27.1) and ranged from 28.5 ± 0.33 for the neat sample up to 33.3 for the 1:100 dilution (*n*

= *3*). Statistical analyses of X2 dilutions determined that there were no significant differences between the neat samples vs. the 1:10 dilutions ($p = 0.0931$) or the CRL reported value ($p > 0.9999$). Additionally, there were no statistical differences between the data obtained for the 1:50 dilutions compared to the 1:100 dilutions ($p = 0.0329$).[24,25]

In the case of sample X5 (**Figure 3-7B**), C_T values increased from a reported value of 16.2 to 23.8 ± 0.19 for the neat sample up to 24.3 ± 0.16 for the 1:100 dilution. Though there was a general overall increase in average C_T values as the dilution factor increased, the neat samples had a higher average C_T value than the 1:10 dilution. In this case, the reported value was statistically different from the average C_T value for the neat samples ($p < 0.0001$). [24,25] There was no significant difference between the value obtained for the neat samples vs. the 1:100 dilutions.

For sample X7 (**Figure 3-7C**), there was no apparent trend regarding changes in average C_T values as dilution ratios changed. The only statistically distinct groups were the neat samples compared to the 1:10 dilution ($p = 0.0441$).[24,25] More significant standard deviations were observed in this group than in any other analyses of blind samples. The average C_T values increased as the dilution ratio increased for samples X8 and X9 (results summarized in **Figures 3-7D and E**, respectively). For X8, values ranged from 19.8 ± 0.13 to 28.0 ± 0.36 as dilution ratios increased (CRL value = 18.1), while the average C_T values ranged from 29.9 ± 0.36 to 35.7 ± 0.79 for sample X9 (CRL value = 25.2). Statistical analyses showed that for sample X9, the 1:10 dilutions vs. 1:50, as well as the 1:50 vs. 1:100 were not significantly different ($p = 0.1058$ and 0.5762, respectively).

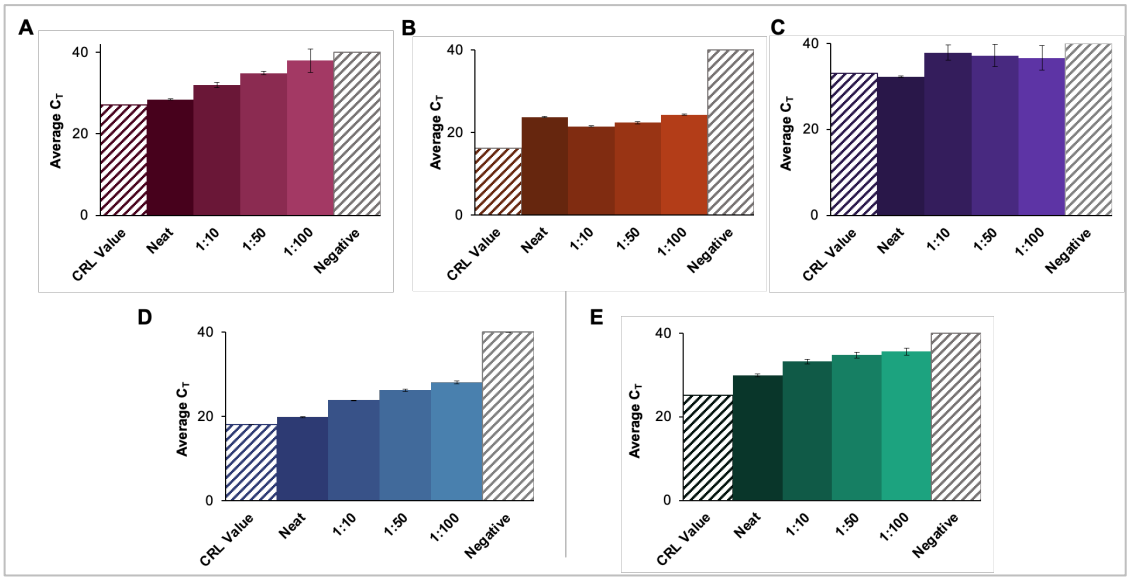

Figure 3-7. Results of a blind study conducted using CRL clinical saliva samples. (A-E) summarize the data obtained from evaluations of blinded CRL samples. Pools for each of 10 blinded samples were created and tested according to the developed protocol and were found to be in 100% agreeance with the reported qualitative results (five positive and five negative samples). The significant increase in C_T value obtained for b and e could be attributed to collection at an earlier date than other positive samples. These may thus have had a lower viral load when analyzed than at initial CRL testing. A negative clinical saliva sample was extracted according to the protocol described for positive clinical samples. A, B, C, and D, and E represent X2, X5, X7, X8, and X9, respectively, and $n = 3$ in each case.

3.3.5. Integration of Assay into a Microfluidic Format

Clinical saliva samples were analyzed using conventional vs. microfluidic methods, and the results were compared. The portable, in-house '*Ultra-Rapid Real-Time Microfluidic PCR Amplification*' instrument used for the microfluidic analyses is shown in **Figure 3-2**. After extraction and RT-PCR analyses, amplification was observed in all reported positive samples tested for neat and 1:50 pools using conventional and microfluidic methods. The average C_T values obtained for the traditional assays were 20.92 ± 0.947 and 24.37 ± 0.158 for neat and 1:50 sample types, respectively. Microfluidic analyses yielded C_T values of 24.3 ± 0.58 and 29 (no deviation) for neat and 1:50 samples.

Additionally, the temperature profile obtained using a thermocouple to monitor the progression of thermocycling in the microfluidic chip chamber is compared to that

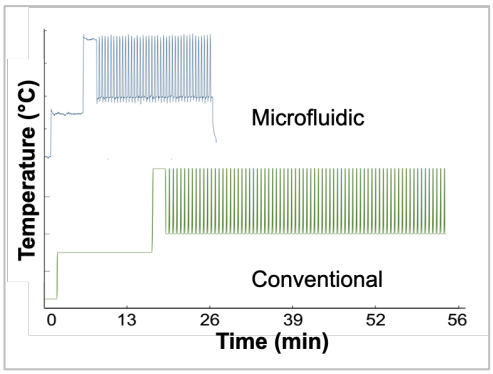

Figure 3-8. Comparison of temperature profiles obtained for microfluidic vs. conventional instruments. Temperature profile expected for the conventional instrument (63 min runtime) compared to that obtained via thermocouple monitoring for the microfluidic instrument (25 min runtime).

projected for the conventional instrument in **Figure 3-8**. The microfluidic device consistently and accurately achieved target temperatures of 95 °C and 60 °C while significantly reducing the overall assay runtime from 63 minutes to 27 minutes.

An increase of 3.5 units for the average C_T values of the neat pools was obtained microfluidically compared to conventional methods. Additionally, there was an increase of 4.7 units when data for the 1:50 pools obtained using microfluidic methods were compared to conventional methods. A graphical comparison of C_T values obtained using conventional vs. microfluidic methods is given in **Figure 3-9.**

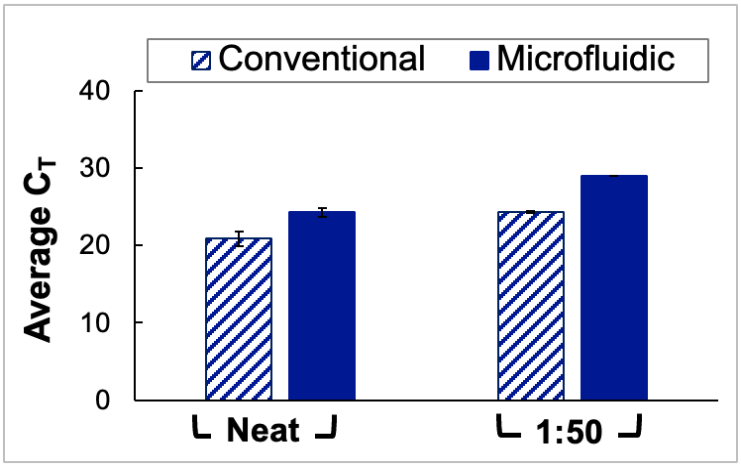

Figure 3-9. Summary of data obtained from a direct comparison of conventional and microfluidic methods - Qiagen extraction & QuantStudio 5 RT-PCR vs. PDQeX extraction and amplification using the ultra-rapid instrument, respectively. *n = 3* in each case).

3.4. Discussion

A previously reported protocol for ultra-fast viral enrichment and enzymatic extraction was used for upstream sample preparation from pooled SARS-CoV-2 samples in multiple sample matrices.[11]Here, viral transport media derived from nasopharyngeal samples, fresh saliva spiked with VTM from nasopharyngeal samples, and saliva samples obtained using a commercially available collection system spanning commonly observed C_T values were analyzed using the adapted protocol, which leveraged magnetically-actuated nanoparticles to capture and isolate virions from the clinical sample matrices.

To demonstrate the sensitivity and performance of the adapted protocol, average C_T values acquired from RT-PCR of prepared viral RNA were compared. Relative viral concentrations and potential effects of largescale dilutions were evaluated based on the theory that any adverse effects arising from sample preparation or dilution steps would result in slower or decreased amplification and comparatively increased C_T values. It was expected that an increase in dilution factor would result in a corresponding rise in average C_T value for dilutions within sample pools.[26] This general trend of a commensurate increase in C_T value and dilution factors reflects a synchronous reduction of the number of virions in the overall volume. Here, we demonstrate successful enrichment, extraction, and detection of virions with minimal loss of amplification or sample concentration with the proposed workflow.

3.4.1. Pooling of Nasopharyngeal (VTM) Samples

Pooling studies were initially completed with VTM nasopharyngeal samples as previous experiments had demonstrated the successful application of the method with

clinical samples of this type.[11] Here, dilutions of 1:10, 1:50, and 1:100 were evaluated; although unlikely that pools of 1:50 or 1:100 will be utilized in practice, it was deemed critical to assess the limits of the method as a measure of its large-scale applicability.

Neat VTM samples classified as having a high viral load (reported C_T value < 20) were successfully detected from samples diluted up to 1:100. A general increase in C_T value was observed for samples classified as moderate except for the 1:10 dilution, where replicate C_T values were lower than that of the neat sample. Though this was unexpected, statistical analyses (Tukey's multiple comparisons tests) found no significant difference between these means, as described in the results section. It was determined that the unexpected occurrence was not prohibitively detrimental to the comprehensive analysis of the data set. Samples reported as having low viral loads were excluded from these analyses as previous experiments showed that for samples of this type, as C_T values approached the maximum number of cycles (40, in this case), it was more likely that the RNA was not homogeneously distributed; consequently, distribution of data points was abnormal.[11]

3.4.2. Pooling of Neat Saliva Spiked with VTM Clinical Samples

When clinical NP samples were spiked with fresh saliva, pooled, and prepared via the previously described protocol, successful amplification was observed for high and moderate viral titer samples. Yet, the theorized trend whereby C_T value was expected to increase incrementally as the dilution factor increased was not evident. Previous work demonstrated no significant difference in data obtained using diluted clinical VTM samples compared to saliva diluted with in-house diluent buffer.[11] However, in that case, preliminary experiments only investigated dilutions up to 10X. The data reported here

indicate stochastic deviations from the expected trend at higher dilutions. Presumably, as the ratio of fresh saliva to sample increased, the inhomogeneity of sample matrices, that is, VTM compared to saliva, induced disparate virion responses to sample enrichment. Though alleviated by the addition of buffer solution, the viscosity of saliva also contributed to the inhomogeneity of samples as mixing was likely inefficient.

Additionally, this was the only sample type where amplification of extracted negatives was observed. Although the average C_T values approximated 40 cycles, this was a nonideal occurrence and could likely be attributed to experimental contamination or, potentially, the detection of a noninfectious, weak positive. It should be noted that the saliva used was obtained from volunteers who had recently (within 3-5 days before donation) tested negative for the presence of the virus. Consequently, while the spiking of VTM into fresh saliva served to approximate workflow performance with pooled clinical samples, the challenges associated with this sample type further validated the need to test uncontrived saliva samples.

3.4.3. Pooling of Clinical Saliva Samples

The CRL COVID-19 Self Collection Testing kit, which includes the DNA Genotek OMNIgene® ORAL (OME-505) device, was granted Emergency Use Authorization (EUA) by the FDA in 2020 based on extensive trials and favorable results from performance evaluations.[20] Consequently, this was deemed an ideal source of clinical saliva samples, reflective of existing pandemic control measures.

Average C_T values increased stepwise for all clinical saliva samples, especially for high and moderate viral titer samples. This observation was attributed to slight decreases

in sensitivity as the negative to positive sample ratio increased. The increase was less consistent for low viral titer dilutions, with the samples of higher dilution ratios statistically approximating the cycle numbers for extracted negative samples. This observation was not extraordinary, given the low virion concentration and the potential for associated stochastic sampling. Nonetheless, qualitative detection in clinical samples with very low viral loads was successfully demonstrated. Additionally, previous studies have indicated that the likelihood of infectivity for patients whose samples are in this range is extremely low, thereby minimizing the potential adverse effects that could result from similarly ambiguous results.[27]

The acquisition of more conclusive results with this sample type when compared to data obtained for contrived saliva samples may also indicate that the buffering system used plays a critical role in determining the feasibility of using saliva samples for diagnoses; the commercially available test kit and the associated reagents appeared to better stabilize and homogenize these samples than the in-house buffering solution, leading to more facile downstream analysis.

3.4.4. Double-Blind study – Clinical Saliva Samples

The presumptive qualitative diagnoses obtained from pooled saliva samples diluted as high as 1:100 from blinded samples were 100% in agreement with the reported clinical results. Further, examination of the results from pooled samples shows that, generally, as the dilution factor increased, so did C_T value. Beyond concordance, the values obtained from these analyses were compared with those obtained from CRL; it was hypothesized

that differences in C_T values would occur as sample preparation, extraction, RT-PCR, and experimental conditions were not identical.

There was no statistical difference between the values we obtained for neat samples and those reported by CRL for samples X2, X7, or X8 (**Figures 3-7A, C, and D**). However, dissimilarities were pronounced for samples X5 and X9 (**Figures 3-7B and E**), for which C_T values increased by 7.4 and 4.4 units, respectively. Interestingly, when results were compared to clinical data to determine the degree of concordance, CRL reported that these samples were several days older than the other eight blinded samples and, as such, may have been adversely affected by sample degradation. This explains the disparity in average C_T value; the initial viral load detected by CRL likely decreased during the elapsed period while additional samples were accumulated, blinded, shipped, and finally analyzed by the described method.

Despite fluctuations in average C_T values for X5 and X7 (**Figures 3-7B and C**), successful qualitative diagnoses were achieved using the described pooling protocol. For sample X7 specifically, these differences could be explained by the low initial viral load indicated by C_T values of 33.1 (CRL) and 32.3 ± 0.20 (experimental values). As seen with low viral titer saliva samples in non-blinded experiments, these results can likely be attributed to stochastic sampling.

3.4.5. Integration of Assay into a Microfluidic Platform

Given the successful application of the described pooling method to assays conducted using a gold-standard RT-PCR instrument, namely the QuantStudio™ 5 Real-Time PCR System for Human Identification, the next phase of experiments will entail

optimization of the method for a novel portable, in-house '*Ultra-Rapid Real-Time Microfluidic PCR Amplification'* instrument as shown in **Figures 3-2A and B.** Preliminary results shown here (**Figure 3-9**) indicate that the device is capable of decreasing the overall runtime for the assay from approximately 63 minutes to 27 minutes (a total time reduction of about 57%) when the assay, currently under optimization, is compared to the manufacturer's (TaqPath™ 1-Step RT-q-PCR Master Mix) recommended protocol. Additionally, experiments indicate that this runtime can be reduced further. This reduction was achieved by varying thermocycling conditions, for example, ramp rates and dwell times, to determine the feasibility of acquiring satisfactory data while using conditions other than those outlined by the manufacturer.

Figure 3-9 illustrates the results obtained when conventional methods – gold standards for extraction and RT-PCR (Qiagen & QuantStudio 5) – are compared to those obtained using the microfluidic platform. When neat and 1:50 dilutions of clinical saliva sample pools were analyzed in parallel, the average C_T values acquired using the conventional vs. microfluidic methods were statistically different (as determined by t-tests, $p = 0.0060$ for comparison of neat samples and <0.0001 for 1:50 dilutions). However, the potential for a substantial reduction in total runtime, the eventual goal of creating a fully integrated portable instrument, and the demonstrated successful qualitative analyses of up to 1:50 dilutions of clinical saliva samples serve to temper the nonideal increase in cycle numbers. This instrument also introduces the potential for rapid, point-of-need (PON), qualitative diagnosis of pooled samples in largescale settings pending the projected integration of extraction and amplification stages into a single miniaturized total analysis system.

3.5. Conclusions

The application of an enrichment and extraction method to large-scale diagnostic screening for SARS-CoV-2 is described herein. Experimental results indicate that the technique is compatible with pooled samples up to dilutions of 1:100 and with a range of sample types, including neat VTM eluate from NP swabs and saliva samples stored in DNA Genotek's proprietary buffer solution for the OMNIgene® ORAL (OME-505) device. Additionally, successful detection of SARS-CoV-2 was achieved for these sample types with minimal loss in sensitivity and comprehensive qualitative accuracy. Still, in the case of contrived saliva samples prepared by spiking NP-derived VTM into fresh saliva, the results were inconclusive and inconsistent, suggesting that the in-house buffering solution used for homogenization and stabilization of the saliva matrix requires further optimization to perform comparably to commercial test kits. This is further substantiated by the fact that the average C_T values obtained from our analyses of the saliva samples collected using these kits approximated those from the third party despite undergoing shipment and multi-day storage.

A double-blind study was also conducted to objectively investigate the performance of this method when applied to "real world" use. The results of this study which utilized the proposed method were 100% concordant with the reported clinical values, with the accurate qualitative designation of five positive and five negative samples achieved, suggesting the potential for obtaining accurate clinical diagnoses in clinical settings.[28]

Finally, preliminary experiments demonstrated the potential for the optimization of the pooling assay for point-of-need (PON) deployment using a novel, ultra-rapid, microfluidic PCR amplification device.

3.6. References

1. Zhu, N.; Zhang, D.; Wang, W.; Li, X.; Yang, B.; Song, J.; Zhao, X.; Huang, B.; Shi, W.; Lu, R.; Niu, P.; Zhan, F.; Ma, X.; Wang, D.; Xu, W.; Wu, G.; Gao, G. F.; Tan, W. A Novel Coronavirus from Patients with Pneumonia in China, 2019. *New England Journal of Medicine* **2020**, *382* (8), 727–733. https://doi.org/10.1056/NEJMoa2001017.

2. Guan, W.; Ni, Z.; Hu, Y.; Liang, W.; Ou, C.; He, J.; Liu, L.; Shan, H.; Lei, C.; Hui, D. S. C.; Du, B.; Li, L.; Zeng, G.; Yuen, K.-Y.; Chen, R.; Tang, C.; Wang, T.; Chen, P.; Xiang, J.; Li, S.; Wang, J.; Liang, Z.; Peng, Y.; Wei, L.; Liu, Y.; Hu, Y.; Peng, P.; Wang, J.; Liu, J.; Chen, Z.; Li, G.; Zheng, Z.; Qiu, S.; Luo, J.; Ye, C.; Zhu, S.; Zhong, N. Clinical Characteristics of Coronavirus Disease 2019 in China. *New England Journal of Medicine* **2020**, *382* (18), 1708–1720. https://doi.org/10.1056/NEJMoa2002032.

3. World Health Organization. *WHO Coronavirus (COVID-19) Dashboard*. https://covid19.who.int (accessed 2022-01-04).

4. Arena, F.; Pollini, S.; Rossolini, G. M.; Margaglione, M. Summary of the Available Molecular Methods for Detection of SARS-CoV-2 during the Ongoing Pandemic. *International Journal of Molecular Sciences* **2021**, *22* (3). https://doi.org/10.3390/ijms22031298.

5. Meagan N. Esbin; Oscar N. Whitney; Shasha Chong; Anna Maurer; Xavier Darzacq; Robert Tjian. Overcoming the Bottleneck to Widespread Testing: A Rapid Review of Nucleic Acid Testing Approaches for COVID-19 Detection. *RNA* **2020**, *26*, 771–783. https://doi.org/10.1261/rna.076232.120.

6. Ravi, N.; Cortade, D. L.; Ng, E.; Wang, S. X. Diagnostics for SARS-CoV-2 Detection: A Comprehensive Review of the FDA-EUA COVID-19 Testing Landscape. *Biosensors and Bioelectronics* **2020**, *165*, 112454. https://doi.org/10.1016/j.bios.2020.112454.

7. World Health, O. *Laboratory Testing for Coronavirus Disease (COVID-19) in Suspected Human Cases: Interim Guidance, 19 March 2020*; World Health Organization: Geneva, 2020.

8. Medeiros da Silva, R. C.; Nogueira Marinho, L. C.; de Araújo Silva, D. N.; Costa de Lima, K.; Pirih, F. Q.; Luz de Aquino Martins, A. R. Saliva as a Possible Tool for the SARS-CoV-2 Detection: A Review. *Travel Medicine and Infectious Disease* **2020**, *38*, 101920. https://doi.org/10.1016/j.tmaid.2020.101920.

9. Barat, B.; Das, S.; De Giorgi, V.; Henderson, D. K.; Kopka, S.; Lau, A. F.; Miller, T.; Moriarty, T.; Palmore, T. N.; Sawney, S.; Spalding, C.; Tanjutco, P.; Wortmann, G.; Zelazny, A. M.; Frank, K. M. Pooled Saliva Specimens for SARS-CoV-2 Testing. *Journal of Clinical Microbiology* **2021**, *59* (3), e02486-20. https://doi.org/10.1128/JCM.02486-20.

10. Joaquín Moreno-Contreras; Marco A. Espinoza; Carlos Sandoval-Jaime; Marco A. Cantú-Cuevas; Daniel A. Madrid-González; Héctor Barón-Olivares; Oscar D. Ortiz-Orozco; Asunción V. Muñoz-Rangel; Cecilia Guzmán-Rodríguez; Manuel Hernández-de la Cruz; César M. Eroza-Osorio; Carlos F. Arias; Susana López. Pooling Saliva Samples as an Excellent Option to Increase the Surveillance for SARS-CoV-2 When Re-Opening Community Settings. *PLOS ONE* **2022**, *17* (1), e0263114.

11. Dignan, L. M.; Turiello, R.; Layne, T. R.; O'Connell, K. C.; Hickey, J.; Chapman, J.; Poulter, M. D.; Landers, J. P. An Ultrafast SARS-CoV-2 Virus Enrichment and Extraction Method Compatible with Multiple Modalities for RNA Detection. *Anal Chim Acta* **2021**, *1180*, 338846. https://doi.org/10.1016/j.aca.2021.338846.

12. Waidi Folorunso Sule; Daniel Oladimeji Oluwayelu. Real-Time RT-PCR for COVID-19 Diagnosis: Challenges and Prospects. *Pan African Medical Journal* **2020**, *35*.

13. Dong, X.; Liu, L.; Tu, Y.; Zhang, J.; Miao, G.; Zhang, L.; Ge, S.; Xia, N.; Yu, D.; Qiu, X. Rapid PCR Powered by Microfluidics: A Quick Review under the Background of COVID-19 Pandemic. *TrAC Trends in Analytical Chemistry* **2021**, *143*, 116377. https://doi.org/10.1016/j.trac.2021.116377.

14. Fredrickson, C. K.; Fan, Z. H. Macro-to-Micro Interfaces for Microfluidic Devices. *Lab Chip* **2004**, *4* (6), 526–533. https://doi.org/10.1039/B410720A.

15. U. S. Food and Drug Administration. *Pooled Sample Testing and Screening Testing for COVID-19*. Coronavirus. https://www.fda.gov/medical-devices/coronavirus-covid-19-and-medical-devices/pooled-sample-testing-and-screening-testing-covid-19#:~:text=Pooling%20samples%20involves%20mixing%20several,expected%20than%20positive%20results (accessed 2022-03-24).

16. Nadja Grobe; Aljahi Cherif; Xiaoling Wang; Zijun Dong; Peter Kotanko. Sample Pooling: Burden or Solution? *Clinical Microbiology and Infection* **2021**, *27*, 1212–1220. https://doi.org/10.1016/j.cmi.2021.04.007.

17. Cherif, A.; Grobe, N.; Wang, X.; Kotanko, P. Simulation of Pool Testing to Identify Patients With Coronavirus Disease 2019 Under Conditions of Limited Test Availability. *JAMA Network Open* **2020**, *3* (6), e2013075–e2013075. https://doi.org/10.1001/jamanetworkopen.2020.13075.

18. CDC. *COVID Data Tracker Weekly Review*. COVID Data Tracker Weekly Review. https://www.cdc.gov/coronavirus/2019-ncov/covid-data/covidview/index.html (accessed 2022-03-24).

19. Nouwairi, R. L.; Cunha, L. L.; Scott, O.; Hickey, J.; Thomson, S.; Knowles, S.; Chapman, J.; Landers, J. P. Ultra-Rapid Real-Time Microfluidic RT-PCR Instrument for Nucleic Acid Analysis. *Lab Chip* **2022**.

20. *Emergency Use Authorization (EUA) Summary CRL Rapid Response*. https://www.fda.gov/media/140661/download (accessed 2022-01-17).

21. *Inactivation of SARS-CoV—2 in samples collected using Oragene, Oracollect and OMNIgene products from DNA Genotek*.

22. Aaron Goutte; Tasha M Santiago-Rodriguez; Heather L Fehling; Rafal Iwasiow. Detection of SARS-CoV-2 in Saliva Using Tailed Amplicon Sequencing. *Journal of Infectious Diseases & Therapy* **2021**, *9* (4). https://doi.org/10.4172/2332-0877.1000464.

23. National Center for Immunization and Respiratory Diseases (NCIRD), D. of V. D. *Interim Guidance for Use of Pooling Procedures in SARS-CoV-2 Diagnostic, Screening, and Surveillance Testing*. https://www.cdc.gov/coronavirus/2019-ncov/lab/pooling-procedures.html#anchor_1595517996705 (accessed 2021-05-07).

24. GraphPad Software, L. L. C. *Prism 9 for MacOS*; GraphPad Software, LLC: San Diego, California USA, 2021.

25. John W. Tukey. Comparing Individual Means in the Analysis of Variance. *Biometrics* **1949**, *5* (2), 99–114. https://doi.org/10.2307/3001913.

26. Chong, B. S. W.; Tran, T.; Druce, J.; Ballard, S. A.; Simpson, J. A.; Catton, M. Sample Pooling Is a Viable Strategy for SARS-CoV-2 Detection in Low-Prevalence Settings. *Pathology* **2020**, *52* (7), 796–800. https://doi.org/10.1016/j.pathol.2020.09.005.

27. Bullard, J.; Dust, K.; Funk, D.; Strong, J. E.; Alexander, D.; Garnett, L.; Boodman, C.; Bello, A.; Hedley, A.; Schiffman, Z.; Doan, K.; Bastien, N.; Li, Y.; Van Caeseele, P. G.; Poliquin, G. Predicting Infectious Severe Acute Respiratory Syndrome Coronavirus 2 From Diagnostic Samples. *Clinical Infectious Diseases* **2020**, *71* (10), 2663–2666. https://doi.org/10.1093/cid/ciaa638.

28. Marshall, J. S.; Turiello, R.; Cunha, L. L.; Frazier, E. V.; Hickey, J.; Chapman, J.; Poulter, M. D.; Fehling, H. L.; Landers, J. P. Rapid SARS-CoV-2 Virus Enrichment

and RNA Extraction for Efficient Diagnostic Screening of Pooled Nasopharyngeal or Saliva Samples for Dilutions Up to 1:100. *Diagnostics* **2022**, *12* (6). https://doi.org/10.3390/diagnostics12061398.

4. Towards the Rapid, Point-Of-Need Diagnosis of SARS-CoV-2 using an Ultra-Rapid Microfluidic PCR Instrument

4.1. Introduction

As discussed in **Chapters 1 and 3,** point-of-need instrumentation for molecular diagnostics is attractive due to the potential for rapid, streamlined, and automated detection.[1] This is especially pertinent regarding the detection of the SARS-CoV-2 virus, as highlighted by the recent global pandemic. As discussed, some vital requirements for the implementation of clinical tests include simplicity, cost-effectiveness, and speed.[1,2] The applicability of RT-PCR due to its sensitivity, specificity, and potential for incorporation into process chains for rapid diagnostics has also been discussed.[1–4]

Consequently, the work described here is an extension of that discussed in **Chapter** 3, wherein the application of enrichment, RNA extraction, and sample pooling of the SARS-CoV-2 virus is described. These analyses also leverage foundational work previously published by members of the Landers lab regarding initial enrichment and extraction studies,[5] the adaptation of this protocol to a centrifugal microfluidic device,[6] and the design, fabrication, and validation of the ultra-rapid real-time microfluidic PCR amplification instrument.[4] Here, the studies converge as a basis for evaluating the applicability of these concepts in tandem, with an eye toward completing a process chain from multiple unit operations, as detailed in **Chapter 1,** and the completion of an integrated, miniaturized total analysis system (μTAs).

Preliminary experiments indicated the potential for reducing total assay runtime for this application, with a 57% reduction in speed detailed in the previous chapter.[2] Additionally, recent work published by Nouwairi et al. regarding the ultra-rapid real-time

microfluidic PCR amplification instrument outlined an 84% reduction in PCR amplification time for RNA and DNA targets in clinical samples.[4] This was achieved by utilizing the rapid PCR kinetics associated with microfluidic technologies, hardware design and manufacture, and the polymeric materials selected for the reaction cartridge.[4] Combined with the inherent advantages of microfluidic systems regarding ease of operation, reduced consumption of resources, the potential for integration, and reduced cost, it was theorized that efforts to adapt the SARS-CoV-2 diagnostic assay to this system were a worthwhile and potentially critical pursuit.

Here, proof-of-principle using viral plasmids as targets is demonstrated. First, the optimization of the assay is investigated using a conventional instrument and an in-tube platform, as the traditional instrument has a higher throughput capacity compared with the microfluidic device; up to 96 in-tube assays can be analyzed simultaneously using the QuantStudio™ 5 Real-Time PCR System for Human Identification, while the microfluidic device analyzes a single sample for each amplification experiment. With this approach, the most effective thermocycling parameters for rapid amplification were determined, and further reductions in overall assay analysis runtime were tested with the microfluidic platform. Of course, the ability to further decrease amplification and detection time with the novel platform was made possible by leveraging its interfacing microfluidic chip.

As a proof of concept, validation experiments were completed using viral RNA extracted from clinical saliva samples. However, it was impossible to conduct these experiments due to logistical difficulties regarding access to the conventional instrumentation. Still, the workflow detailed here includes the successful extraction of the

RNA using the PDQeX Nucleic Acid Extractor before storage of these specimens for future analysis.

Finally, a protocol for the recycling and reuse of microfluidic cartridges was developed to conserve resources and mitigate the disruption of research due to shipping and manufacturing challenges. The evolution of the recycling protocol and data associated with its successful implementation are also outlined.

4.2. Materials and Methods

4.2.1. Preparation and Analysis of Clinical SARS-Cov-2 Samples

Although the extracted specimens remain in storage, the enrichment and extraction techniques are described here as these activities have been completed and are to be used for future validation experiments. As detailed in **Chapter 3.2.**, saliva samples were obtained using the DNA Genotek OMNIgene® ORAL (OME-505) device to stabilize viral RNA in the CRL COVID-19 Self Collection Testing Kit from Clinical Reference Laboratory, Inc. (CRL, Lenexa, KS, USA. Initial COVID-19 testing conducted at CRL was performed using the CRL Rapid Response™ test with the FDA's Emergency Use Authorization (EUA).[7] Initial diagnostic testing was conducted at CRL using the Zymo Quick-DNA/RNA™ Viral MagBead kit (Zymo Research Corporation, Irvine, CA, USA) on Tecan automated platforms (Tecan Life Sciences, Männedorf, Switzerland). RT-PCR was performed using the Logix Smart™ Coronavirus Disease 2019 (COVID-19) kit (Co-Diagnostics, Inc., Salt Lake City, UT, USA) using Bio-Rad CFX96™ Touch Real-Time PCR detection systems with Bio-Rad CFX Manager 3.1 software (Bio-Rad Laboratories,

Hercules, CA, USA). These samples were stored and shipped at room temperature to researchers at the Landers Lab, University of Virginia.

4.2.2. Sample Pooling Protocol

The pooling protocol was identical to that described in Chapter 3.2.2. and illustrated in **Figure 3-1A**. Briefly, sample pools of "high", "moderate," or "low" viral titer clinical samples were created with the combination of 250 µL of three positive samples to form a 750 µL bulk sample. These samples were then combined with negative clinical samples in the appropriate volumes to achieve 1:50 dilutions, while a portion was designated for analysis as the "neat" samples.

4.2.3. RNA Extractions using the PDQeX Platform

This process is outlined in **Figure 4-1** and is an abbreviated version of that described in **Figure 3-1**. Samples were first enriched via nanoparticle pre-concentration.[2,5] Positive and negative clinical samples were combined in the appropriate proportions to achieve "neat" and 1:50 pools with a total volume of 500 µL (**Figure 4-1A**). A total of 100 µL of Nanotrap® Magnetic Virus Particles (CERES Nanosciences, Inc, Manassas, VA, USA) were added to each dilution pool and thoroughly mixed via vortexing. The supernatant was removed, and the extraction cocktail was added. The cocktail included 88 µL of nuclease-free water, 2 µL of RNAGEM (MicroGEM US Inc., Charlottesville, VA, USA), and 10 µL of 10 X BLUE Buffer (MicroGEM, Charlottesville, VA, USA). After thoroughly vortexing the pooled sample and the extraction cocktail, the mixture was transferred to a PDQeX cartridge before thermocycling in the PDQeX Nucleic acid

Extractor (MicroGEM, Charlottesville, VA, USA) at 95 °C for 5 minutes (**Figure 4-1B**). This process was repeated for each dilution pool, and aliquots of extracted samples were stored at -80 °C for future use (**Figure 4-1C**).

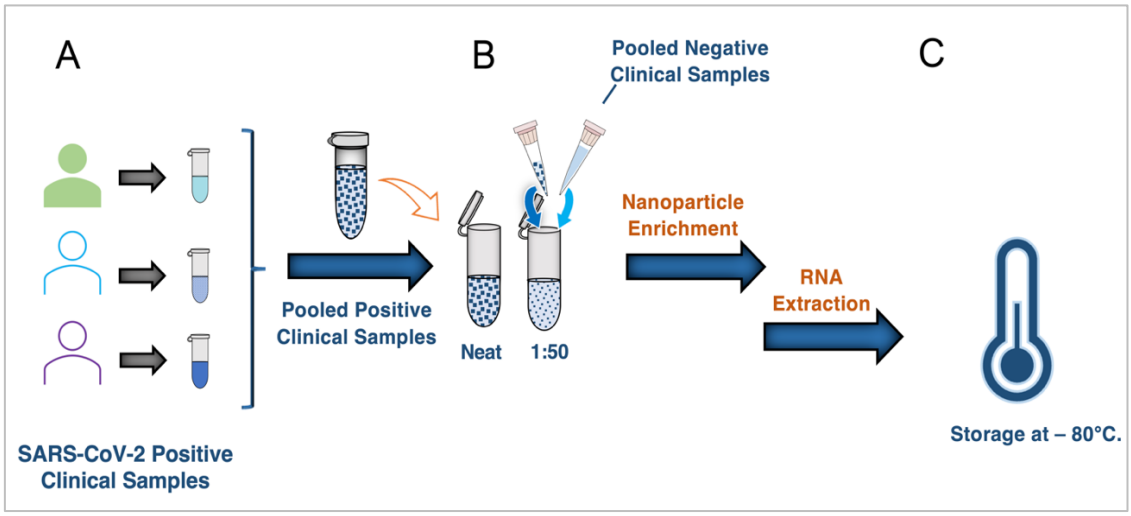

Figure 4-1. Schematic outlining the enrichment and extraction process employed for clinical saliva samples. (A) shows the pooling of positive clinical samples. (B) Dilution of positive pool using pooled negative clinical samples. (C) Storage of extracted RNA at -80 °C until further analyses.

4.2.4. Optimization of Thermal Cycling Parameters

RT-PCR protocol

The C_T data obtained from RT-PCR experiments were used to evaluate the relative success of upstream preparation and detection of SARS-CoV-2 viral RNA in pooled and diluted samples. The selected RT-PCR assay was developed by the Centers for Disease Control and Prevention (CDC) under an emergency use authorization (EUA) in February 2020.[7] The 2019-nCoV_N_Positive Control plasmid (Integrated DNA Technologies, Coralville, IA, USA) was serially diluted to obtain concentrations of 1000, 100, 50, and 10 copies/µL and used as positive controls for real-time RT-PCR. Each reaction was a total volume of 20 µL and was comprised of 5 µL of plasmid (positive controls) or PCR-grade

water (non-template controls), a 5 µL of TaqPath™ 1-Step RT-q-PCR Master Mix (Thermo Fisher Scientific, Waltham, MA, USA), 1 µL of SARS-CoV-2 (2019-nCoV) CDC RUO N1 primer-probe mix (Integrated DNA Technologies, Coralville, IA, USA), and 9 µL of PCR-grade water. Samples were run in either triplicate or quintuplicate using the suggested protocol for the TaqPath™ 1-Step RT-q-PCR Master Mix, including UNG incubation at 25 °C for 120 s, reverse transcription at 50 °C for 900 s, polymerase activation at 95 °C for 120 s, and 40 amplification cycles (95 °C for 3 s and 60°C for 30 s). As plasmid was used for these experiments, the reverse transcription step was not integral and was thus reduced to 1 s. Samples were analyzed using a QuantStudio™ 5 Real-Time PCR System for Human Identification (Applied Biosystems, Waltham, MA, USA).

Optimization using the conventional instrument

Initial experiments to determine optimal conditions for rapid RT-PCR were conducted using a conventional instrument – the QuantStudio™ 5 Real-Time PCR System for Human Identification (Applied Biosystems, Waltham, MA, USA). The most efficient but rapid thermocycling parameters were systematically determined by stepwise variations using the conditions described in the previous section as a starting point. Firstly, experiments were conducted with and without the inclusion of the UNG incubation step while adhering to all other manufacturing conditions, and the data obtained were compared. Subsequently, the polymerase activation step was optimized by testing periods of 2 min (manufacturer's protocol), 1 min, and 30 s. Denaturation and annealing (amplification cycles) were optimized by testing dwell times of 3 vs. 1 s, and 30, 15, 7, and 1 s,

respectively. All experiments were conducted using the instrument's default ramp rate of about 2.73 °C/s.

Optimization using the microfluidic instrument

After optimization of thermal cycling parameters on the conventional instrument, the parameters were applied to the microfluidic device, and further reduction of assay time was investigated. The initial thermal cycling program excluded UNG incubation and utilized 2 min at 95°C for polymerase activation, 1 s at 95° C for denaturation, and 7 s at 60 °C for annealing. Denaturation and annealing steps were repeated for a total of 40 cycles. (These parameters are discussed further in the following Results and Discussion section). Given the derived parameters, ramp rates of 8, 10, and 12 °C/s were first evaluated. This was followed by testing 2 min, 1 min, 30 s, and 15 s dwell times for optimization of the polymerase activation step, and 7 vs. 1 s for the annealing step. Note that the denaturation step required no further optimization, as it was already held for 1 s.

These experiments were conducted using an injection-molded, custom polycarbonate microfluidic chip. As detailed by Nouwairi et al., the inlet and amplification chamber had total capacities of 50 and 40 µL, respectively, and were connected via two channels. Additional pieces of heat-stable, biocompatible, adhesive-backed polymeric film (100 µm thick) were used to enclose the architecture on either face of the chip. These pieces were cut using a CO_2 laser cutter (VLS3.50, Universal Laser Systems, AZ, USA). Following the input of reagents via pipetting, a ball press was used to place a polymeric ball (McMaster-Carr, IL, USA) into the inlet to hermetically seal fluid into the chip. The assembly of the components used in this process is summarized in **Figure 4-2**. Fluid was

centrifugally transferred into the PCR amplification chamber (**Figure 4-2A**) before the cartridge was placed into the mechatronic system (depicted in **Figure 3-7**, for reference).

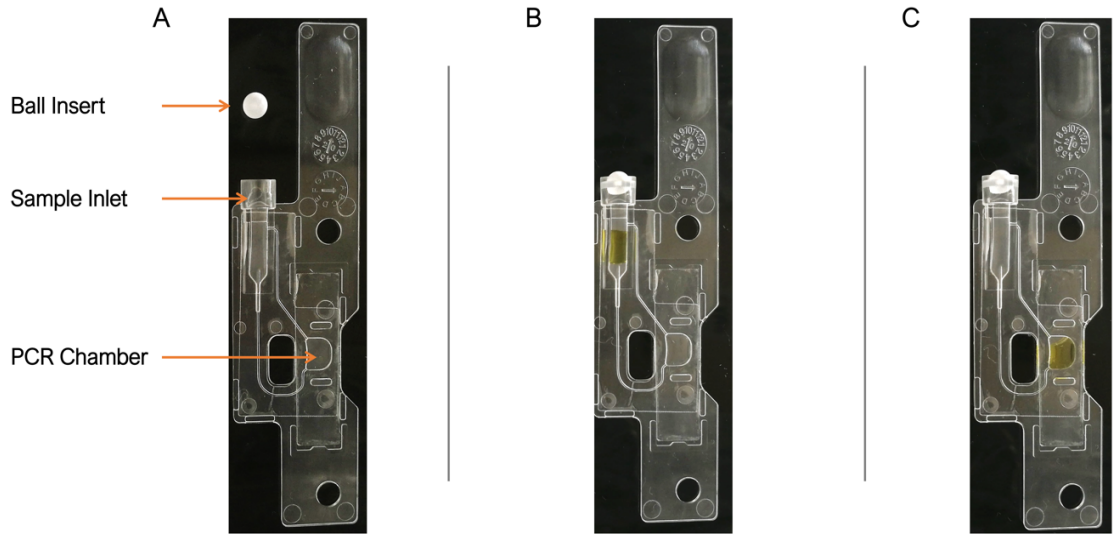

Figure 4-2. Cartridge images against a dark background captured using a lightbox and Huawei smartphone. (A) shows the cartridge before the introduction of liquid into the cartridge via the inlet. The ball insert is placed using a ball press and serves to create a hermetically sealed system. (B) shows the sealed cartridge with yellow food dye in the inlet chamber for illustrative purposes. (C) shows the cartridge following the centrifugally driven transfer of the fluid to the PCR chamber for analysis.

Data Acquisition and Analysis

In all cases, optimization experiments were conducted using the 2019-nCoV_N_Positive Control plasmid (Integrated DNA Technologies, Coralville, IA, USA), which was serially diluted to obtain a concentration of 100 copies/µL and used as a standard analyte. Additionally, as described in the previous section, TaqPath™ 1-Step RT-q-PCR Master Mix and the associated chemistry were used for all experiments.

Following data acquisition, analysis and statistical comparisons were conducted using GraphPad Prism version 9.3.1. (350) for macOS, GraphPad Software, San Diego, California USA, and Microsoft Office Excel. Baseline determination, subtraction, and Following data acquisition, analysis, and statistical comparisons were conducted using

GraphPad Prism version 9.3.1. (350) for macOS, GraphPad Software, San Diego, California USA, and Microsoft Office Excel. Baseline determination, subtraction, and thresholding for the conventional instrument were performed using the device's software, exported, and analyzed.[8,9] As outlined by Nouwairi et al., in the case of the microfluidic apparatus, the average fluorescence signal from the third to 15th cycles was subtracted from each data point along the curve, and the mean baseline was determined through the calculation of the overall mean of all average baseline.[4,9] The threshold was set as three times the standard deviation of the comprehensive mean baseline, while the amplification curves graphed relative fluorescence units vs. cycle number. As is common practice, the cycle threshold values were then defined as the points at which the amplification curves crossed the threshold.[9]

4.2.5. Cartridge Recycling Protocol

Cartridge recycling was conducted using batches of ≤ 20. First, the adhesive was pierced and removed using a small gauge (~ 20 g) needle. The cartridges were then submerged in 90% isopropanol (IPA, Sigma Aldrich, St. Louis, MO) (v/v, in PCR-grade water) for five minutes. Cartridges were removed from 90% IPA, and the adhesive was peeled from the cartridge manually. The cartridges were then resubmerged in 90% IPA for another 5 minutes. Any remaining glue was removed from the cartridges using WypAll® General Cleaning Wipes (Kimberly-Clark, Irving, TX, USA) dampened with 90% IPA. Any residual IPA was removed by thorough rinsing with deionized (DI) water. The

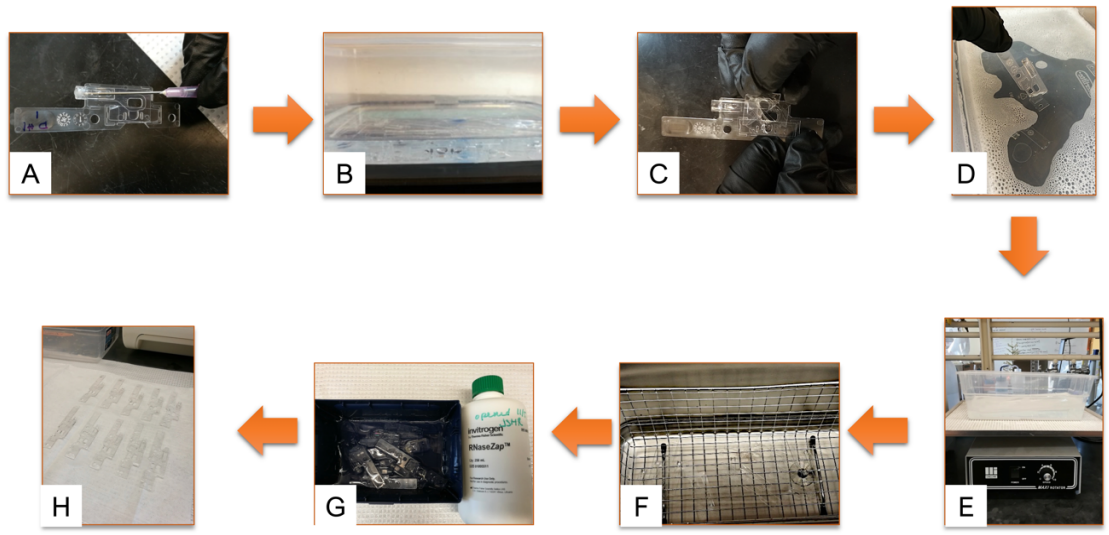

Figure 4-3. Outline of cartridge recycling protocol. (A) depicts ball removal. After adhesive is pierced, moderate force is required to expel the insert from the inlet. (B) shows a lateral view of chips submerged in IPA. (C) shows the removal of polymeric adhesive from the cartridge. (D) illustrates the submersion of the cartridge in soap solution after removal of polymeric adhesive and residue. € shows the cartridges in soap solution as rotation occurs. (F) This image shows submerged cartridges in the sonication basket. (G) shows submersion in RNase Decontamination Solution. (H) Sterilized chips as arranged before the drying step.

cartridges were then submerged in a soap solution (~ 750 mL) and rotated using a Labline 4631 Platform Rotator Shaker (Marshall Scientific LLC, Hampton, NH, USA) for ~5 minutes before rinsing with DI water. Subsequently, the microdevices were placed into a sonicator basket and submerged in a Digital Ultrasonic Cleaner (Seeutek) with 10% Cavicide Disinfectant Cleaner solution (750 µL) (Metrex Research, LLC., Orange, CA, USA) and cleaned for ten minutes at room temperature. These were then removed and rinsed with DI water before an additional submersion in the sonicator basket – the cleaning solution for this step was 750 µL of 20% bleach solution.

After cleaning for seven minutes, another rinse step was conducted, and excess water was drained from the cartridges. This was followed by submersion in RNase*Zap*™ RNase Decontamination Solution (Invitrogen, Waltham, MA, USA) for ~ 3 minutes before a final rinse with DI water. Cartridges were then placed on a sheet in single layers and covered before being left for ≥ 24 hours to dry. This process is summarized in **Figure 4-3**.

The dried and sterilized chips were then stored in a sealed container with layers separated using sheets until required for experiments. Randomly selected cartridges were assembled and used to perform RT-PCR under the same conditions discussed in previous sections to verify successful sterilization. Non-template controls were used to evaluate the sterility of the recycled cartridges using the microfluidic instrument. Additional negative controls were run using the Quant Studio 5 instrument to confirm results.

4.3. Results and Discussion

Preliminary studies showed that the microfluidic device could be used to achieve an assay runtime reduction of 57%.[2] As was the case in the previous phase of experiments, there was no modification of the amplification mixture used for RT-PCR. A further reduction of amplification runtime with minimal losses in assay sensitivity is discussed here.

Although optimization experiments were devised to facilitate adaptation to the microfluidic instrument, initial optimization experiments were conducted with the conventional instrument due to the primary drawback of the novel platform – only a single sample can undergo RT-PCR using this device at any time. Conversely, up to 96 samples can be analyzed simultaneously using the Quant Studio 5 instrument. The process of obtaining a statistically significant number of replicates for each adjustment of parameters and the inclusion of non-template controls made early adaptation to the microfluidic apparatus impractical. As such, after maximizing the use of the conventional instrument to derive a baseline rapid thermocycling program, assay time was further reduced using the microfluidic device and interfacing chip. Controls were run with each experiment; note

that non-template controls were excluded from bar charts, as there were no observations of their amplification and detection.

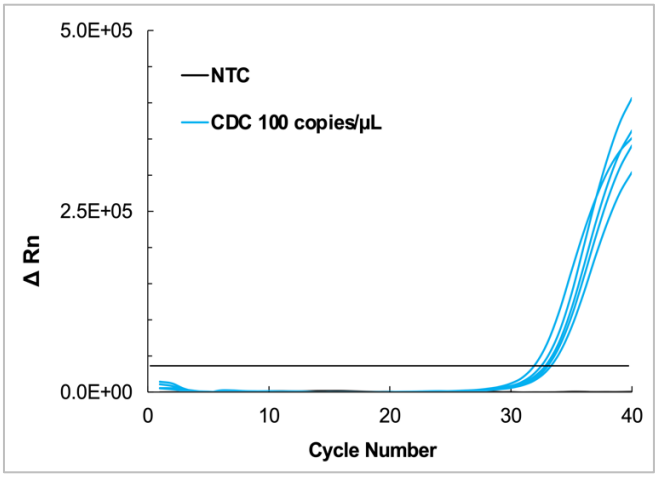

Figure 4-4. Amplification curve obtained using manufacturer's protocol. This protocol was paired with conventional instrument to determine a basis of comparison for subsequent adjustment of parameters (*n = 5*).

Table 4-1. Summary of C_T data obtained using the manufacturer's protocol and conventional instrument (*n = 5*).

Replicate	C_T Value
1	31.783
2	32.110
3	32.568
4	32.335
5	31.188

4.3.1. Optimization of Thermal Cycling Parameters

RT-PCR protocol

The average assay runtime for the RT-PCR experiments conducted using the manufacturer's protocol and the conventional instrument was 63 min and 11 s. The sensitivity and performance of the adapted parameters were determined by statistical comparison to the average C_T values obtained using these conditions. The amplification plot derived using these parameters is given in **Figure 4-4,** and a summary of C_T data obtained is shown in **Table 4-1**. Briefly, the C_T values for replicates amplified at a concentration of 100 copies/µL averaged ~31.997; this served as a baseline for the optimization of individual parameters moving forward.

Optimization using the conventional instrument

The UNG incubation step was the first parameter evaluated to determine whether or not this step in the workflow was required. The UNG, or uracil-N-glycosylase gene, is often included in master mixes to prevent "carryover" contamination, a type of contamination that may originate from the laboratory environment or amplification products and primers used in previous experiments that may produce false positives.[10,11] Additionally, UNG degrades mis-primed or nonspecific products in the reaction mixture while leaving the reproduced nucleic acid template intact.[10] Recall that the goal of this work is to develop a rapid protocol to contribute to the fastest viable sample-to-answer microfluidic workflow, the inclusion of this step was evaluated by comparing data obtained with the exclusion of the UNG incubation step. A bar chart comparing data obtained in each case is shown in **Figure 4-5**., which demonstrates no statistical difference between means ($p < 0.05$, $\alpha = 0.05$), and the UNG step was excluded from the thermocycling program for the next stage of optimization experiments.

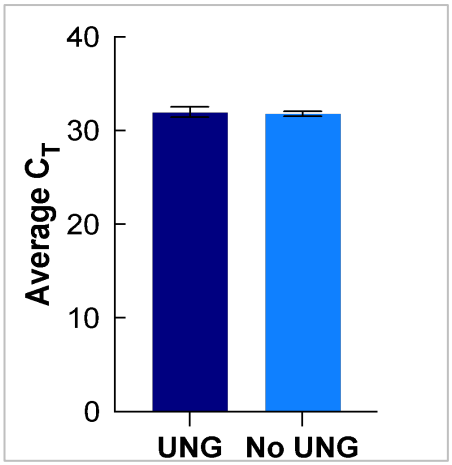

Figure 4-5. UNG vs. No UNG. This bar chart comparing data obtained when the necessity of the UNG step was evaluated ($n = 5$). There were no instances of amplification observed for the non-template controls.

In addition to the manufacturer's recommended dwell time of 2 min, 1 minute and 30 s dwell times were evaluated for the polymerase activation step. The polymerase

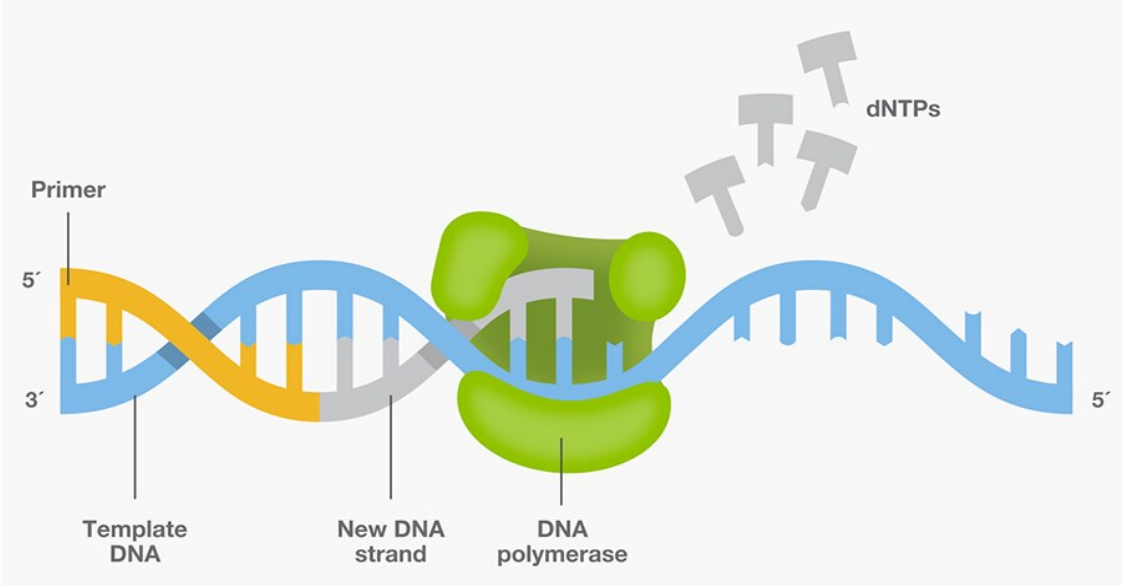

Figure 4-6. A schematic depicting the extension of 3' end of a PCR primer in the 5' to 3' by DNA polymerase. This highlights the necessity of polymerase activation for the successful amplification of target nucleic acids. The term dNTP refers to deoxyribonucleotide triphosphate (dNTP), the substrates for DNA polymerizing enzymes. [11]

activation step is critical to successful amplification as the DNA polymerase synthesizes new complementary strands from the single-stranded template DNA. They are characteristically active in the 5' → 3' direction, thereby incorporating nucleotides and facilitating extension at their 3' ends in the same direction.[12–14] **Figure 4-6** (Thermo Fisher Scientific) illustrates and summarizes this mechanism of action. Average C_T values of 32.8 ± 0.339, 32.5 ± 0.401, and 30.0 ± 2.376 were obtained for 2 min, 1 min, and 30 s dwell times, respectively. There was no statistical difference between means obtained when the 2 min dwell time was compared to the 1 min ($p = 0.5992$) and 30 s ($p = 0.1630$) dwell times ($\alpha = 0.05$ in all cases).[8] Despite these findings, it was decided that it would be best to proceed using the recommended 2-minute period as this data set showed minor deviation between replicates. Additionally, the inclusion of this step would not contribute significantly to the overall runtime – at best, a minute and a half would be subtracted from the total time.

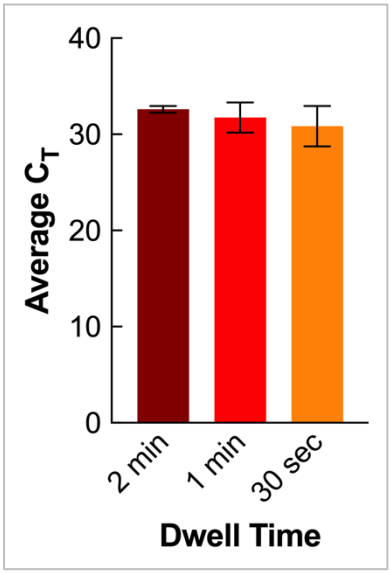

Figure 4-7. Comparison of data obtained for optimization of the polymerase activation step using the conventional instrument. There was no statistical difference between means ($p < 0.05$) ($n = 5$). There were no instances of amplification observed for the non-template controls.

This could be critical in some reactions, but it was determined to be an acceptable compromise in this case, as finetuning would occur using the microfluidic device. This data is summarized in **Figure 4-7.**

Regarding the cycles of the 2-step amplification program, including denaturation and annealing, decreased hold parameters were also investigated. For denaturation, the manufacturer-recommended 3 s dwell time was tested in addition to a reduced 1 s dwell time. The average C_T values obtained were 32.8 ± 0.339 and 32.4 ± 1.143 for 3 and 1 s dwell times, respectively. An unpaired t-test analysis showed no significant difference between the means ($p = 0.9470$) at a 95% confidence interval.[8]

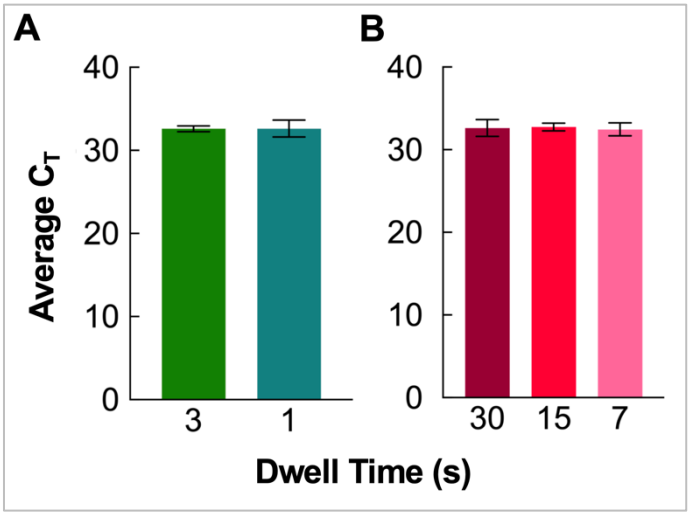

Figure 4-8. Comparison of data obtained for optimization of the amplification cycling steps using the conventional instrument. (A) Data obtained for the denaturation step which was not statistically different when analyzed using a t-test ($p = 9470$). (B) Data obtained for annealing step which was not statistically different ($p = 0.8398$). $n = 5$ and $\alpha = 0.05$ in both cases. There were no instances of amplification observed for the non-template controls

Finally, 15 and 7 s dwell times were evaluated for the annealing step, in addition to the manufacturer-recommended 30 s, and the average C_T values obtained were 32.4 ± 1.144, 33.1 ± 0.164, and 32.7 ± 0.987, respectively. There were no statistically significant differences between the means when

tested with a 95% confidence interval (p = 0.8398). These data are shown in **Figure 4-8**. Given these results, the 1 s and 7 s dwell times were optimal for the denaturation and annealing steps, respectively. The optimal thermocycling parameters for rapid RT-PCR for this assay using the conventional instrument are summarized in **Table 4-2**. As evidenced by this data, the runtime was reduced from 63 min 11 s to 34 m and 5 s.

Table 4-2. Optimized thermocycling RT-PCR protocol derived using the conventional Instrument. Manufacturer-recommended dwell times follow the optimized time in parentheses for reference.

STAGE	STEP	# OF CYCLES	TEMP.	DWELL TIME
1	*NO* UNG incubation	-	-	-
2	Polymerase activation	1	95 °C	2 min (2 min)
3	Amplification - Denaturation	40	95 °C	1 s (3 s)
	Amplification - Annealing		60 °C	7 s (30 s)

Optimization using the microfluidic instrument

As previously discussed, optimization experiments on the microfluidic platform utilized the thermocycling protocol described in **Table 4.2** as the starting point for experiments. Still, ramp rate reduction was made possible by the unique hardware specific to the device and the physics associated with the microfluidic interface. As detailed in the publication outlining the validation of this instrument, it was theorized that the direct interfacing between the Peltiers and the PCR chambers would facilitate rapid heat transfer.[4] Additionally, as discussed in **Chapter 1**, the transition to the microfluidic platform, despite the use of identical volumes, resulted in a higher surface-area-to-volume ratio, accelerating

the kinetics of the reaction.[4,15] Ramp rates were also adjusted before moving on to optimization of dwell times based on kinetics – the amplification rate correlates to the speed at which thermal cycling occurs.[11]

The ramp rates used to evaluate the optimum conditions for ultra-rapid amplification were 8, 10, and 12 °C/s. Previous validation experiments report that 12 °C/s is the fastest ramp rate possible without requiring significant power consumption.[4] This is a critical consideration as the long-term goal is to achieve an integrated, portable, and field-deployable instrument for point-of-need diagnostics. Similarly, a cooling rate of 10 °C/s was used in all cases based on validation data.

It should be noted that the manufacturers of the conventional instrument (Quant Studio 5), Thermo Fisher, report that the device has one of the highest temperature ramping capacities available for commercial instruments of this type. Still, the maximum suggested ramp rate for the 0.2 mL 96-well block model is listed as 6.5 °C/s. Considering this, achieving a 12 °C/s ramp rate with a field-deployable device would be an exceedingly favorable alternative to using a less rapid instrument within the confines of a central laboratory. **Figure 4-9** summarizes the data obtained from the ramp rate optimization experiments. CONV+MP refers to analyses

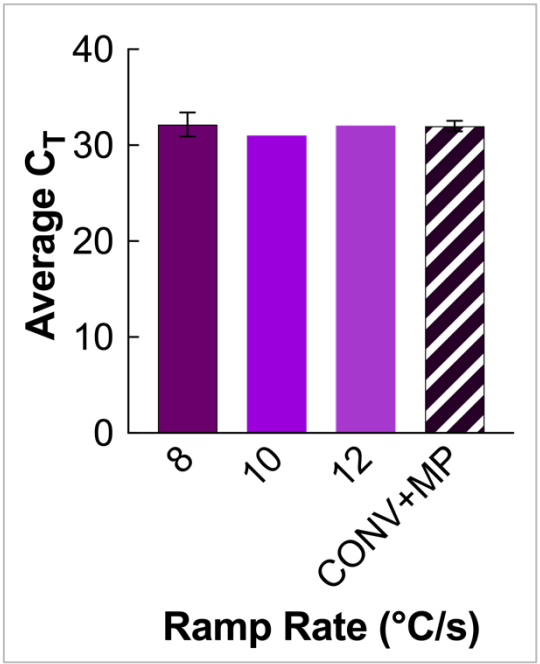

Figure 4-9. Optimizarion of ramp rate using the microfluidic instrument. There were no statistical differences between means at the 95% confidence level ($n = 5$ for the conventional assay and $n = 3$ for the microfluidic assay). CONV+MP denotes the average C_T data obtained using the conventional instrument and manufacturer's protcol.

performed using the manufacturer-recommended protocol and the conventional instrument.

The average C_T values obtained were 32.2 ± 1.258, 31.0 (no deviations, denoted ND hereafter), and 32 (ND) for 8, 10, and 12 °C/s, respectively, as compared to 32.0 ± 0.538 obtained using the conventional instrument and the manufacturer's protocol. A one-way ANOVA test showed no significant difference between means ($p < 0.05$). Further, there were no statistical differences when the C_T values obtained using the microfluidic instrument were individually compared to those obtained using the conventional device and the manufacturer's protocol; QS5 vs. 8, 10, and 12 °C/s comparisons yielded p values of 0.9736, 0.1597, and > 0.9999, respectively.[8] $\alpha = 0.05$ in all cases. As such, a ramp rate of 12 °C/s was chosen for subsequent assays.

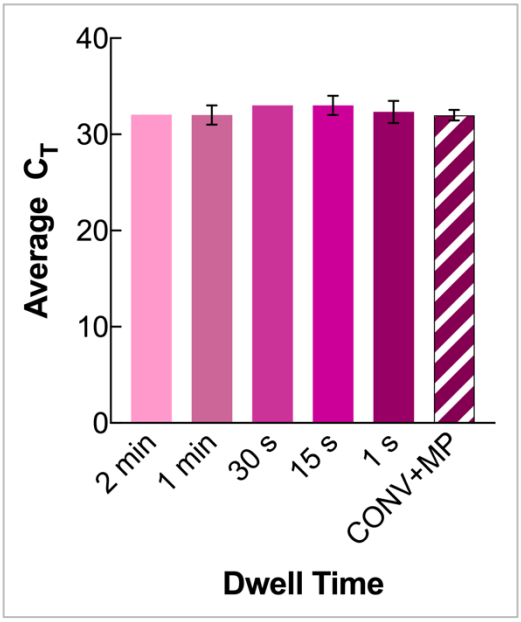

Figure 4-10. Optimization of the polymerase activation dwell time using the microfluidic instrument. There were no statistical differences between means at the 95% confidence level (*n = 5* for conventional and *3* for microfluidic assays, $\alpha = 0.05$).

The dwell times for the polymerase activation step were evaluated similarly. 2 min, 1 min, 30 s, 15 s, and 1 s dwell times were analyzed to determine optimal conditions. The average C_T values obtained were 32.0 (ND), 32.0 ± 1.000, 33.0 (ND), 33.0 ± 1.000, and 32.3 ± 1.155 for 2 min, 1 min, 30 s, and 15 s and 1s dwell times, respectively (**Figure 4-10**). There were no statistical differences between means when a one-way ANOVA test was conducted ($\alpha = 0.05$). QS5 vs. 2 min, 1 min, 30 s, 15 s, and 1 s yielded p values of > 0.9999, > 0.9999,

0.3052, 0.3052, and > 0.9650, respectively.[8] Therefore, the selected dwell time moving forward was 30 s, as it was the fastest time tested for which there was no deviation between replicates. Recall, this is a critical step in the PCR process. It was thus important that the results be reproducible at this stage.

Finally, the dwell times for the denaturation and annealing stages were tested. Similar to before, no further optimization was required for the denaturation step as the minimum dwell time of 1 s had been achieved. For the annealing step, however, the 7 s time derived from optimization using the conventional instrument was compared to 3, and 1 s dwell time to evaluate performance. The average C_T values obtained were 33.0 (ND), 35.6 ± 0.577 for 7 s and 3 s dwell times, respectively (**Figure 4-11**). The maximum C_T value of 40 was assigned for assays conducted using the 1 s dwell time as there was no amplification in any of the replicates tested. In this case, there were statistical differences between the average C_T values obtained when tested using a one-way ANOVA.[8]

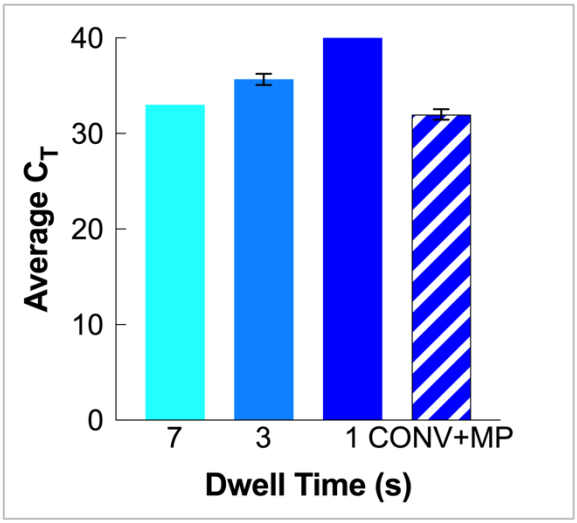

Figure 4-11. Optimization of dwell time for the annealing step using the microfluidic instrument. There was no amplification for assays performed using the 1 s dwell time and the maximum cycle value of 40 was assigned. In this case, there were statistical differences observed between means (n = 5 for conventional and 3 for microfluidic assays). CONV+MP denotes the average C_T data obtained using the conventional instrument and manufacturer's protocol. $\alpha = 0.05$.

Additionally, when the CONV+MP value was compared to each dwell time, the 7s, 3s, and 1s data were statistically different with p values of 0.0246, < 0.001, and < 0.001. Therefore, the 7 s dwell time was deemed most appropriate for amplification moving forward. Though the values obtained were statistically different from the average C_T values obtained using

the manufacturer's protocol and Quant Studio 5, they were statistically similar to those obtained using the conventional instrument and the rapid protocol with a 7 s dwell time for the annealing step ($p = 0.2925$, $\alpha = 0.05$).

Additionally, given that the average cycle values were 33.0 (ND) for the 7 s dwell time using the microfluidic platform vs. 32.0 ± 0.538 using the conventional device and manufacturer's protocol, the slight increase in cycle number and associated decrease in sensitivity are not likely to be prohibitive. Further, the overall assay runtime was decreased from 63 m and 11 s to 13 min and 30 s – a reduction of approximately 50 min (79%). It is reasonable to conclude that the statistical difference could be perceived as an acceptable loss given the potential for the ultra-rapid PON diagnosis of the SARS-CoV-2 virus.

In summary, the optimized program includes a ramp rate of 12 °C/s, a 30 s polymerase activation step at 95 °C, a 1 s denaturation step at 95 °C, and a 7 s annealing step at 60 °C, with 40 amplification cycles.

4.3.2. Cartridge Recycling Protocol

As was the case in most research laboratories and clinical facilities during the peak of the SARS-CoV-2 pandemic, there were difficulties regarding the replenishment of microfluidic chips for use in this and other projects in progress due to supply chain limitations. Here, a recycling protocol was developed and validated to mitigate the impact of this occurrence and reuse chips while also ensuring the removal of any reagents or amplicons from the reaction chambers.

The success of the protocol was evaluated by conducting PCR experiments using the conditions derived above, non-template controls, and microfluidic cartridges that had

been recycled and assembled. Ideally, following the recycling protocol no amplification would be observed, indicating successful sterilization of the microfluidic cartridges.

The amplification mixture was prepared with a portion designated for analysis using the conventional instrument and the remainder to be analyzed using the microfluidic device. The assays run on the traditional instrument served as controls as it was theorized that amplification observed on both instruments would indicate an issue with the master mix; conversely, if amplification was detected for microfluidic samples but not observed in conventionally run samples, this might indicate microbial activity or microfluidic instrument malfunction and simplify the troubleshooting process. This was critical to verify, as initial experiments showed consistent amplification when recycled chips were tested for sterility. However, the amplification was later linked to reagent contamination rather than ineffective sterilization.

A vital consideration when devising this procedure was the most efficient way to remove the polymeric sheets and adhesives from the surface of the chip without causing physical or chemical defects leading to device failure, including cracks, scratches, or etching. This eliminated the use of several physical and chemical disassembly strategies initially under consideration.

First, 90% isopropyl alcohol was selected as a method to remove the polymeric sheets and requisite adhesives from the primary chip. This was chosen after unsuccessfully exploring alternatives, including gun cleaner (as suggested by the manufacturers of the sheets) and mineral oil. According to the safety data sheet, the gun cleaner was 70 – 90% acetone, 5 – 10 % carbon dioxide, 5 – 10 % toluene, and 1 – 5 % orange terpenes.[16] Exposure of the chips to the 90% IPA solution was minimized to prevent physical damage.

Next, the soap solution (as detailed in **Materials and Methods**) was included to remove visible residue and debris from the chip's surfaces. The bleach, Cavicide Disinfectant Cleaner solutions, and RNaseZAP™ were sequentially formed to eliminate viral and bacterial contaminants.[17–19]

As shown in **Figure 4-12**, no amplification was observed for replicates run using the microfluidic or conventional instrument. This was indicative of a viable protocol, and

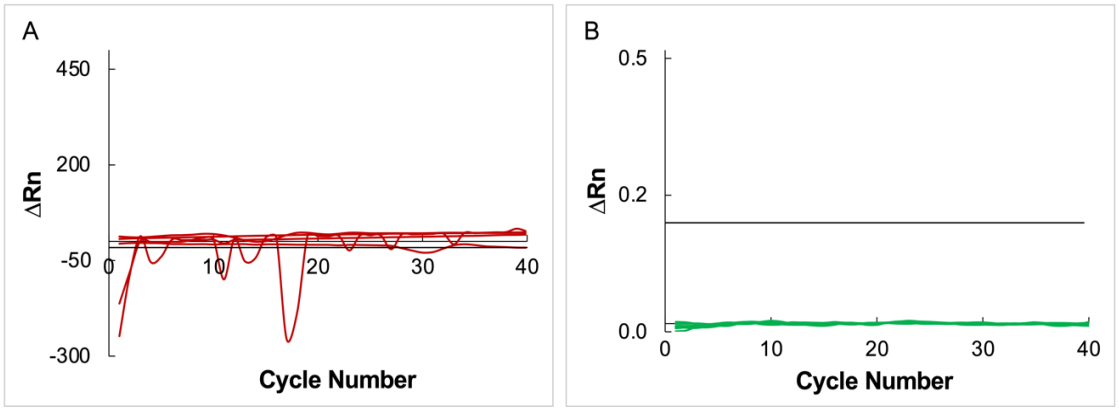

Figure 4-12. Amplification plots obtained from validation of the chip cleaning protocol. (A) shows the plot obtained from the microfluidic instrument ($n = 5$) while (B) shows that obtained using the conventional instrument ($n = 7$). There was no amplification observed in either case.

further validation was obtained as additional researchers performed the protocol independently with similar outcomes.

4.4. Conclusions

The optimization of thermocycling parameters for the adaptation of a SARS-CoV-2 diagnostic assay to an ultra-rapid microfluidic PCR instrument is described here. This entailed the systematic adjustment of RT-PCR conditions, first on a conventional instrument (QuantStudio™ 5 Real-Time PCR System for Human Identification) and then on a microfluidic device, to determine the shortest overall runtime for the assay that can be used without significant losses to sensitivity. The transition from an in-tube format to a

microfluidic platform was also investigated in this process. These proof-of-concept experiments are the basis for applying the adapted RT-PCR protocol to the extracted clinical saliva samples for method validation.

When the optimization experiments using the conventional instrument, the QuantStudio™ 5 Real-Time PCR System for Human Identification, were completed, the runtime required for successfully amplifying and detecting the 2019-nCoV_N_Positive Control plasmid was reduced from 63 min and 11 s to 34 min and 5 s. This was further reduced when optimization experiments were conducted using the microfluidic device, giving a final runtime of 13 min and 30 s, a 50 min (79%) time reduction. Additionally, these objectives were achieved with no adjustments to the amplification mixture chemistry and minimal sensitivity loss ($< \pm 1$ C_T unit).

These experiments indicate the potential for eventually realizing an on-site, ultra-rapid diagnostic platform for detecting SARS-CoV-2 that serves communities at the point of need.

4.5. References

1. Dong, X.; Liu, L.; Tu, Y.; Zhang, J.; Miao, G.; Zhang, L.; Ge, S.; Xia, N.; Yu, D.; Qiu, X. Rapid PCR Powered by Microfluidics: A Quick Review under the Background of COVID-19 Pandemic. *TrAC Trends in Analytical Chemistry* **2021**, *143*, 116377. https://doi.org/10.1016/j.trac.2021.116377.

2. Marshall, J. S.; Turiello, R.; Cunha, L. L.; Frazier, E. V.; Hickey, J.; Chapman, J.; Poulter, M. D.; Fehling, H. L.; Landers, J. P. Rapid SARS-CoV-2 Virus Enrichment and RNA Extraction for Efficient Diagnostic Screening of Pooled Nasopharyngeal or Saliva Samples for Dilutions Up to 1:100. *Diagnostics* **2022**, *12* (6). https://doi.org/10.3390/diagnostics12061398.

3. Waidi Folorunso Sule; Daniel Oladimeji Oluwayelu. Real-Time RT-PCR for COVID-19 Diagnosis: Challenges and Prospects. *Pan African Medical Journal* **2020**, *35*.

4. Nouwairi, R. L.; Cunha, L. L.; Scott, O.; Hickey, J.; Thomson, S.; Knowles, S.; Chapman, J.; Landers, J. P. Ultra-Rapid Real-Time Microfluidic RT-PCR Instrument for Nucleic Acid Analysis. *Lab Chip* **2022**.

5. Dignan, L. M.; Turiello, R.; Layne, T. R.; O'Connell, K. C.; Hickey, J.; Chapman, J.; Poulter, M. D.; Landers, J. P. An Ultrafast SARS-CoV-2 Virus Enrichment and Extraction Method Compatible with Multiple Modalities for RNA Detection. *Anal Chim Acta* **2021**, *1180*, 338846. https://doi.org/10.1016/j.aca.2021.338846.

6. Turiello, R.; Dignan, L. M.; Thompson, B.; Poulter, M.; Hickey, J.; Chapman, J.; Landers, J. P. Centrifugal Microfluidic Method for Enrichment and Enzymatic Extraction of Severe Acute Respiratory Syndrome Coronavirus 2 RNA. *Anal. Chem.* **2022**, *94* (7), 3287–3295. https://doi.org/10.1021/acs.analchem.1c05215.

7. *Emergency Use Authorization (EUA) Summary CRL Rapid Response*. https://www.fda.gov/media/140661/download (accessed 2022-01-17).

8. GraphPad Software, L. L. C. *Prism 9 for MacOS*; GraphPad Software, LLC: San Diego, California USA, 2021.

9. Real-Time PCR Handbook - Thermo Fisher Scientific, 2014.

10. *What is UNG/UDG?*. https://www.thermofisher.com/us/en/home/life-science/pcr/real-time-pcr/real-time-pcr-learning-center/real-time-pcr-basics/what-is-ung-udg.html (accessed 2021-11-12).

11. Yamamoto, Y. PCR in Diagnosis of Infection: Detection of Bacteria in Cerebrospinal Fluids. *Clin Diagn Lab Immunol* **2002**, *9* (3), 508–514. https://doi.org/10.1128/cdli.9.3.508-514.2002.

12. *PCR Basics*. https://www.thermofisher.com/us/en/home/life-science/cloning/cloning-learning-center/invitrogen-school-of-molecular-biology/pcr-education/pcr-reagents-enzymes/pcr-basics.html (accessed 2022-07-09).

13. Kuhn, H.; Sahu, B.; Rapireddy, S.; Ly, D. H.; Frank-Kamenetskii, M. D. Sequence Specificity at Targeting Double-Stranded DNA with a γ-PNA Oligomer Modified with Guanidinium G-Clamp Nucleobases. *Artif DNA PNA XNA* **2010**, *1* (1), 45–53. https://doi.org/10.4161/adna.1.1.12444.

14. Stillman Bruce. Deoxynucleoside Triphosphate (DNTP) Synthesis and Destruction Regulate the Replication of Both Cell and Virus Genomes. *Proceedings of the National Academy of Sciences* **2013**, *110* (35), 14120–14121. https://doi.org/10.1073/pnas.1312901110.

15. Wittwer, C. T.; Herrmann, M. G. 14 - Rapid Thermal Cycling and PCR Kinetics. In *PCR Applications*; Innis, M. A., Gelfand, D. H., Sninsky, J. J., Eds.; Academic Press: San Diego, 1999; pp 211–229. https://doi.org/10.1016/B978-012372185-3/50015-8.

16. ChemTel Inc. *Safety Data Sheet according to OSHA HCS (29CFR 1910.1200) and WHMIS 2015 Regulations*. Break-Free Powder Blast Gun Cleaner. http://sds.chemtel.net/webclients/safariland/finished_goods/Break-Free%20Powder%20Blast%20Gun%20Cleaner.pdf (accessed 2022-07-09).

17. US EPA, O. *What's the difference between products that disinfect, sanitize, and clean surfaces?* https://www.epa.gov/coronavirus/whats-difference-between-products-disinfect-sanitize-and-clean-surfaces (accessed 2021-09-01).

18. Wu, Y.; Wu, J.; Zhang, Z.; Cheng, C. DNA Decontamination Methods for Internal Quality Management in Clinical PCR Laboratories. *J Clin Lab Anal* **2018**, *32* (3). https://doi.org/10.1002/jcla.22290.

19. *Instrument Cleaning - Rnase Decontamination*. National Institute of Environmental Health Sciences.https://www.niehs.nih.gov/research/resources/protocols/extraction/cleaning/index.cfm (accessed 2022-07-05).

5. Towards the Ultra-Rapid, Multitarget, On-site PCR Detection of Bordetella Species on a Miniaturized Real-time PCR System

5.1. Introduction

Whooping cough, commonly known as pertussis, is a highly contagious respiratory disease caused by the Gram-negative coccobacillus *Bordetella pertussis.*[1–4] According to the Centers for Disease Control and Prevention (CDC), there are an estimated 24.1 million cases of pertussis and approximately 160 700 deaths annually.[5,6] Pertussis epidemics usually occur in three to five-year cycles, with the infection typically being transferred from adolescents and adults to susceptible infants. [1] While pertussis in adolescents and adults is generally mild, infants, especially those under five months old, often have severe and sometimes fatal symptoms.[1,3] These symptoms may include paroxysmal cough, which gives the illness its name, lymphocytosis, dysregulated secretion of insulin, alterations in neurologic function, and post-tussive vomiting, which may result in malnutrition and dehydration.[2] Although additional species exist in the Bordetella family, *pertussis* is most often observed in cases of human infections. Pertussis may spread rapidly within populations via contact with airborne droplets.[7] The basic reproductive number (R_0) of this illness, a term that refers to the expected number of secondary cases produced by a confirmed primary case in a completely susceptible population, has been reported to be higher than those observed for polio, rubella, smallpox, mumps, and diphtheria, with one infected person potentially transmitting *B. pertussis* to as many as 12 – 17 other individuals. For comparison, the number of infections estimated to be transferred from an infectious to susceptible person for polio and smallpox is 5 – 7.[7]

Given this disease's highly contagious nature, several diagnostic methods are currently in use to lessen the spread of pertussis by early detection and treatment of infected persons. These methods include bacterial culture, serology, direct fluorescent antibody (DFA) methods, and polymerase chain reaction (PCR) techniques.[4,7] Of these methods, culture is reported to be 100% specific and is often referred to as the "gold standard". [4,7,8] However, it is also less sensitive than other methods, with a 12 – 60% sensitivity rate and the drawback of lengthy incubation periods.[4,7,9] Conversely, real-time PCR assays have shown higher sensitivity and specificity, with rates of 70 – 99% for sensitivity and 86 – 100% for specificity.[4,9] As such, PCR analyses are currently the primary method of detection and diagnosis.

Most PCR tests currently used achieve diagnoses by detection of insertion sequences. Insertion sequences refer to "transposable DNA elements approximately 1 000 base pairs in length that can be inserted into multiple sites on the same chromosome".[1] These insertion sequences are usually present in multiple copies per genome, thereby increasing the sensitivity of PCR analyses. Typically, clinical diagnoses target a single gene sequence, usually 1S481, as it is a multicopy sequence and inherently confers higher sensitivity. Estimates of the number of copies per *B. pertussis* genome range from 50 to as many as 238.[1,4,10] Unfortunately, the prevalence of this insertion sequence can also result in false positives and false negatives. False-positive diagnoses are generally more likely as copy numbers of targets increase because DNA contamination is more readily amplified.[1,3,4,8,10,11] Still, a pilot study conducted in February 2010 in the United Kingdom found that approximately 80% of laboratories relied solely on the detection of IS481 for the diagnosis of whooping cough.[11] Although this study was conducted some time ago,

data reported by the CDC indicates that this is still the primary target of PCR analyses for pertussis diagnoses.[12]

To circumvent the issue of false-positive diagnoses, secondary insertion sequences are often tested. This strategy is also recommended by the CDC.[12] Another insertion sequence, IS1002, is secondary in prevalence to IS481 and is often suggested as a means of confirming positives. It is found in *B. pertussis* with 4 to 8 copies per genome.[1] In tandem, the IS481 target could be used as a highly sensitive screening assay, while the IS1002 target serves as a confirmatory tool.[1]

Given this information, a method of detecting *B. pertussis* and diagnosing whooping cough with high sensitivity and specificity is detailed herein. In addition to validating these insertion sequences, the protocol is further optimized for adaptation to an ultra-rapid microfluidic PCR platform to create a rapid, low-cost, point-of-need (PON) assay. A PON assay could facilitate mitigation of community outbreaks in susceptible populations, for example, in school settings.

This protocol was optimized by evaluating experimental parameters using a conventional PCR instrument before adapting to a microfluidic platform. Thermal cycling parameters were systematically assessed to determine the fastest feasible runtime with minimal losses in sensitivity. This process is similar to that described in **Chapter 4,** where the PCR protocol is optimized and adapted to use with a microfluidic platform.

5.2. Materials and Methods

5.2.1. Preparation of Standards

Standard samples of *Bordetella pertussis* UT25 genomic double-stranded DNA (Vaccine Development Center, WV, USA or ATCC, Manassas, VA, USA) with a concentration of 1.0 ng/µL were prepared using molecular biology grade nuclease-free water (Fisher Scientific, Pittsburgh, PA, USA) as diluent.

5.2.2. Real-time PCR

Each reaction totaled 20 µL and comprised 2 µL of template DNA or nuclease-free water, as appropriate, 10 µL of Luna® Universal Probe qPCR Master Mix (New England Biolabs Inc., Ipswich, MA, USA), 0.8 µL of 10 µM forward primer (Eurofins Genomics Company, Louisville, KY, USA), 0.8 µL of 10 µM reverse primer (Eurofins Genomics Company, Louisville, KY, USA), 0.4 µL of probe, (Eurofins Genomics Company, Louisville, KY, USA), 2 µL of template DNA, and 6 µL of nuclease-free water. The primers and probes used were specific to the targeted insertion elements (IS1002 and IS481) as appropriate and were based on those detailed by Roorda et al.[11] These are shown below in **Table 5-1**.

Table 5-1. DNA sequences of primers and probes directed against the insertion sequences used in this study. These sequences were based on those detailed by Roorda et al.[11]

TEMPLATE	PRIMER/PROBE (LABEL)	SEQUENCE (5'-3')
IS481	Forward primer	GCCGGATGAACACCCATAAG
	Reverse primer	GCGATCAATTGCTGGACCAT
	Probe (FAM)	CGA TTG ACC TTC CTA CGT C [MGBEQ] (19mer)
IS1002	Forward primer	CTA GGT CGA GCC CTT CTT GTT AAC
	Reverse primer	GCG GGC AAG CCA CTT GTA
	Probe (CY5)	CAT CGT CCA GTT CTG TTG CAT CAC CC [BHQ2] (26mer)

The protocol recommended by the manufacturers was used for PCR analyses of matrix effects. This entailed an initial denaturation step at 95 °C for 60 s, followed by 40 to 45 amplification cycles comprising denaturation at 95 °C for 15 s and annealing and extension at 60 °C for 30 s. The QuantStudio™ 5 Real-Time PCR System for Human Identification (Applied Biosystems, Waltham, MA, USA) was used to conduct these experiments.

5.2.3. Optimization of Thermal Cycling Parameters

In all cases, optimization experiments were conducted using 1.0 ng/µL of template *B. pertussis* DNA and run in either triplicate or quintuplicate for each condition.

Optimization using the conventional instrument

As seen in **Chapter 4**, initial assay optimization experiments were conducted using a conventional instrument - the QuantStudio™ 5 Real-Time PCR System for Human Identification. The optimal parameters for thermocycling were determined similarly by systematically adjusting the conditions for the real-time PCR protocol described above. In this case, the insertion element targeted was IS1002 due to a protracted and persistent IS481 contamination issue. As detailed in the introductory section, the high prevalence of the IS481 targets in the pertussis genome may often lead to the amplification of contaminating DNA. Unfortunately, this issue was frequently encountered in the course of these experiments. Still, although there was no systematic optimization using the IS481 insertion element, the data obtained from the use of the manufacturer's protocol before the contamination event was used as a basis of comparison when microfluidic instrument optimization was conducted.

Firstly, the dwell time of the initial denaturation step was optimized by testing 60, 30, and 15 seconds. Next, the denaturation and annealing phases of the amplification cycling step were optimized by testing 15, 7, and 1 s, and 30 and 15 s, respectively. This process is summarized in **Table 5.2**.

Table 5.2. Summary of parameters systematically evaluated. This was done to derive the optimum thermocycling program for rapid PCR using the conventional instrument.

Optimization	Stage					
	Initial Denaturation		Amplification (45 cycles)			
	Temp (°C)	Time (s)	Temp (°C)	Time (s)	Temp (°C)	Time (s)
Manufacturer's Protocol	**95**	**60**	**95**	**15**	**60**	**30**
Dwell Time: Initial Denaturation	95	**60 30 15**	95		60	30
Dwell Time: Denaturation	95		95	**30 15 1**	60	30
Dwell Time: Anneal	95		95		60	**30 15 7**

Optimization using the microfluidic instrument

The optimized settings derived from the conventional instrument were applied to the microfluidic device. This was the initial step in further reduction of total assay time by varying parameters and comparing data. As such, the initial thermal cycling program was 60 s for initial denaturation, 7s for the denaturation phase of amplification, and 15 s for the annealing step. (These parameters are discussed further in the following Results and Discussion section). The microfluidic cartridge used with this instrument is detailed in **Chapter 4**.

First, ramp rates of 6, 8, and 10 °C were evaluated. This was followed by testing dwell times of 60, 30, and 1 s for the initial denaturation step. Finally, the amplification cycling step was optimized by testing 15, 7, and 1 s dwell times for denaturation and

annealing steps. In this case, optimization experiments were conducted for IS481 and IS1002 targets.

Data Analysis

Following data acquisition, analysis and statistical comparisons were conducted using GraphPad Prism version 9.3.1. (350) for macOS, GraphPad Software, San Diego, California USA, and Microsoft Office Excel. Baseline determination, subtraction, and thresholding for the conventional instrument were performed using the device's software, exported, and analyzed.[13,14] As outlined by Nouwairi et al., in the case of the microfluidic apparatus, the average fluorescence signal from the third to 15th cycles was subtracted from each data point along the curve, and the mean baseline was determined through the calculation of the overall mean of all average baseline.[14,15] The threshold was set as three times the standard deviation of the comprehensive mean baseline, while the amplification curves graphed relative fluorescence units vs. cycle number. As is common practice, the cycle threshold values were then defined as the points at which the amplification curves crossed the threshold.[14]

5.3. Results and Discussion

Given the successful amplification of viral RNA using the ultra-rapid microfluidic instrument described in Chapter 4, along with the preliminary data obtained from the analyses of human genomic DNA extracted from buccal swabs described by Nouwairi et al., it was theorized that the assay for the detection and diagnosis of whooping cough could be adapted to this microfluidic platform.

Again, initial experiments were conducted using the conventional instrument due to the impracticability of completing the entire process using the microfluidic device. As stated in **Chapter 4**, analysis of only a single sample per amplification experiment was a limiting factor associated with the microfluidic platform. Further reduction of assay runtime was then completed using the microfluidic instrument. There was no amplification of non-template controls, and these were assigned the maximum cycle number of 40 and excluded from the graphs.

Here, parameters chosen as a result of optimization experiments were to be applicable to the successful detection and diagnosis of both insertion elements to create a more accurate, multitarget, rapid diagnostic assay for the detection of *pertussis* and thus whooping cough.

5.3.1. Optimization of Thermal Cycling Parameters

Optimization using the conventional instrument

The average assay runtime for PCR experiments conducted using the manufacturer's protocol and the conventional instrument was approximately 59 minutes. The performance of the adapted parameters at each stage was evaluated by statistically comparing the average C_T values at each stage to the data obtained using these standard conditions. The amplification plot derived using these parameters and targeting the IS1002 insertion element is shown in **Figure 5-1**, with a summary of C_T data shown inset. The average C_T value obtained in this case was 20.7 ± 0.05. Although there were no optimization experiments for the IS481 target as discussed above, data from an assay conducted using the manufacturer's protocol and the conventional method performed

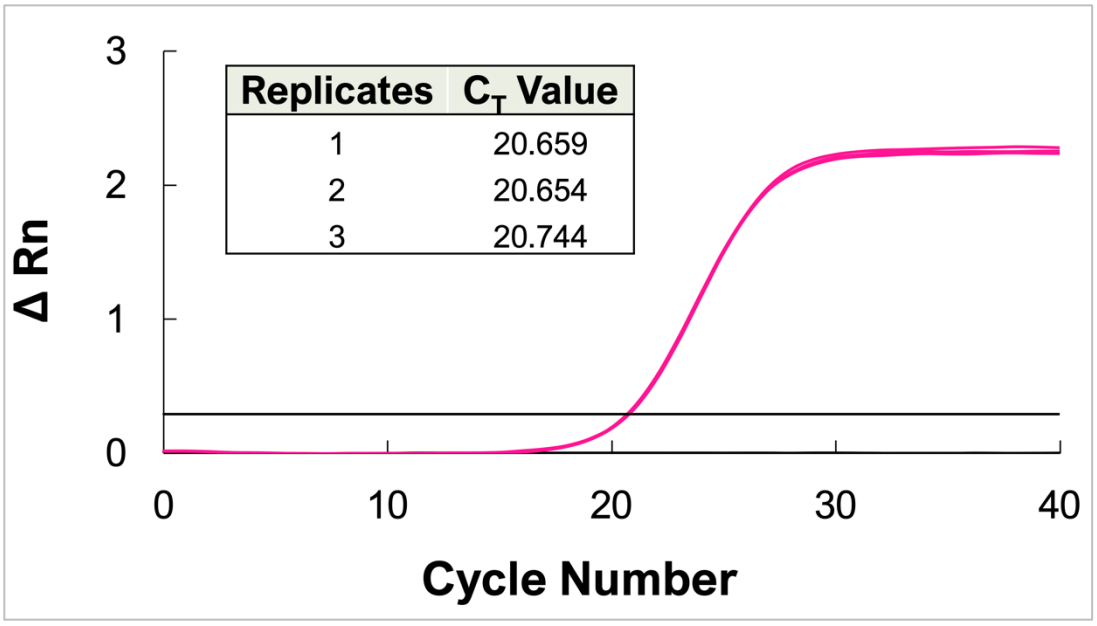

Figure 5-1. Data obtained using the manufacturer's protocol and targeting the IS1002 insertion element. This protocol was paired with the conventional instrument to derive a basis of comparison for optimization experiments (*n = 3*). The C_T values obtained are given inset.

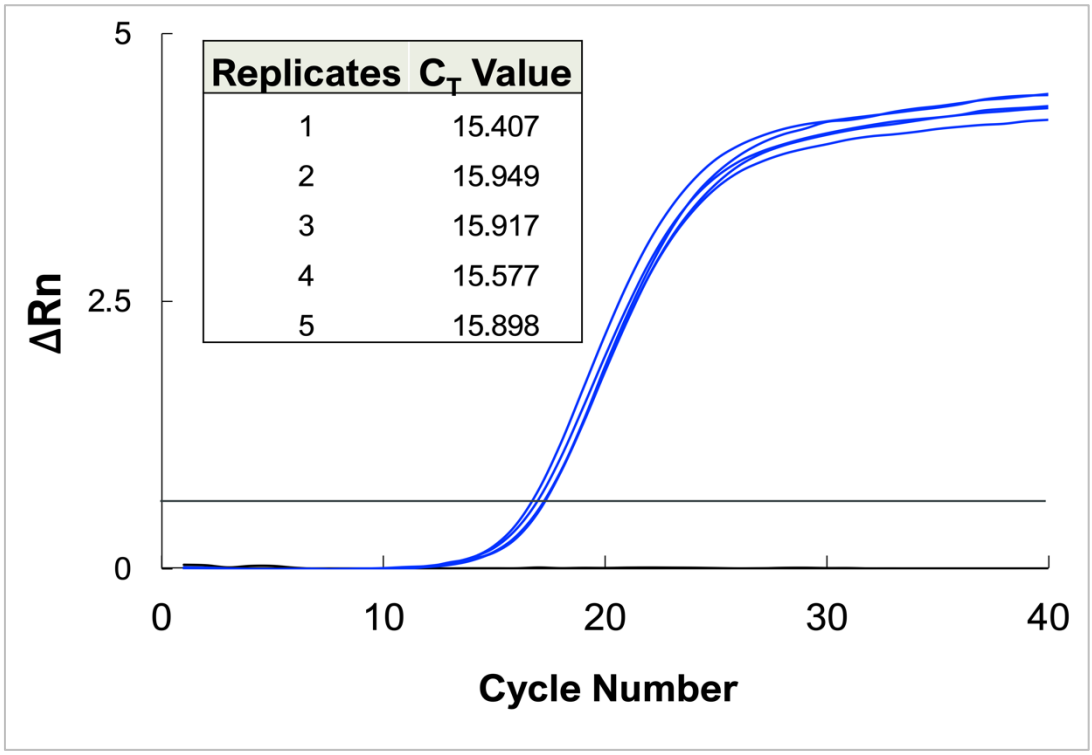

Figure 5-2. Data obtained using the manufacturer's protocol and conventional instrument and targeting the IS481 insertion element. The C_T values are given; *n = 5*.

before the contamination issue developed was used as a basis of comparison and is given

in **Figure 5-2**. The average C_T value obtained for this target was 15.7 ± 0.243.

For IS1002, in addition to the values listed above (inset **Figure 5-1**) for the manufacturer's suggested dwell time of 60 s, the average C_T values obtained were 23.1 ± 1.08 and 23.4 ± 1.13 for 30 and 15 seconds, respectively (**Figure 5-3**) when dwell times for the initial denaturation step were evaluated. A one-way ANOVA test showed statistical differences between means at a 95% confidence level. When the average values for the 60 s dwell time were compared to 30 and 15 s data via Dunnett's multiple comparisons test, these were found to be significantly different, with a p value of 0.0300 for 60 s vs. 30 s and 0.0172 for 60 s vs. 15 s.[13,16] Given the 3 unit increase in C_T and the statistical differences calculated when the additional dwell times were tested, the 60 s dwell time was retained for subsequent experiments.

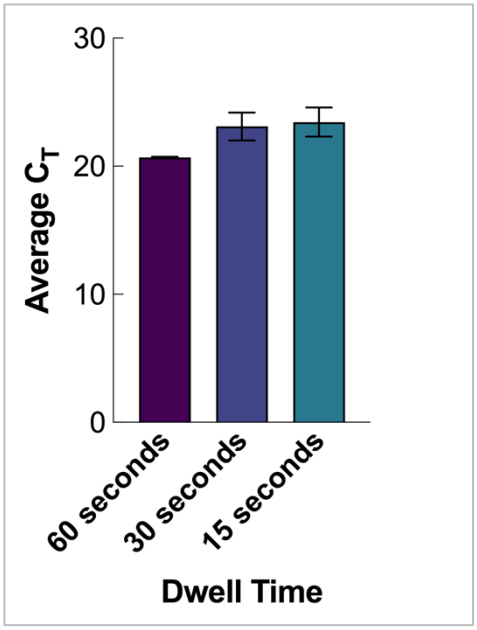

Figure 5-3. Comparison of data obtained for optimization of the initial denaturation dwell time using the conventional instrument. These data were found to be statistically different (p = 0.0188), and the 60 s dwell time was selected (*n = 3, α = 0.05*).

Next, the dwell times for the denaturation step of the amplification cycling phase were assessed, and 15, 7, and 1 second dwell times were evaluated. Additional experiments were conducted to reevaluate the 1-second runtime and determine if the disparity in results obtained was due to experimental error or inefficient amplification. On the second occasion, less favorable and more disparate data was collected; as such, it was deduced that this dwell time could not feasibly be selected. Only 1 of 3 replicates produced a measurable

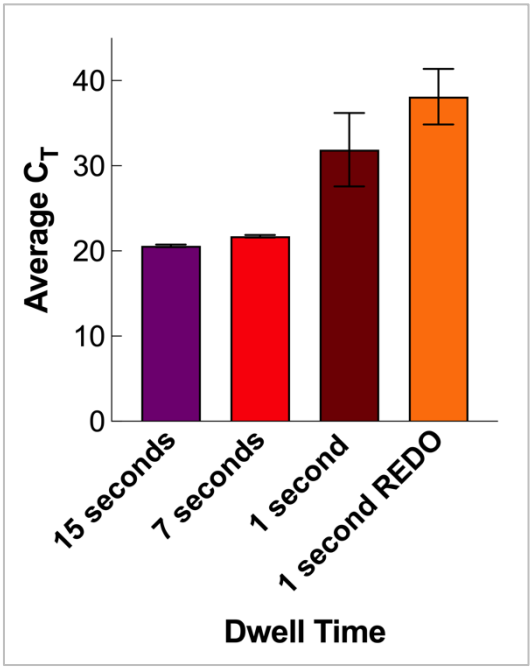

Figure 5-4. Comparison of data obtained for optimization of the amplification cycle's denaturation dwell time using the conventional instrument. These data were found to be statistically different from each other (p = 0.0027) and the 7 s dwell time was selected (*n = 3, α = 0.05*).

response, and the remaining replicates were assigned the maximum cycle value of 40. The results obtained from these optimization experiments are summarized in **Figure 5-4**.

The average C_T values, in this case, were 20.6 ± 0.146, 21.7 ± 0.166, and 31.9 ± 4.315 for dwell times of 15, 7, and 1 s, respectively. When the 1 s dwell time was reanalyzed, the average C_T value obtained was 38.12 ± 3.259. The values derived using the 1 s dwell time were significantly higher than the others, indicating that this was insufficient to allow for complete denaturation of DNA.

As discussed in **Chapter 1**, in the case of TaqMan real-time PCR, an oligonucleotide probe is fluorescently labeled on the 5' end and includes a quencher dye on the 3' end. In the intact state, the fluorescence is quenched by proximity between the probe and a quencher dye. In the presence of a target, the probe and quencher dye are separated, and the emitted fluorescence facilitates the measurement and quantification of DNA.[17,18] Consequently, if there is insufficient separation of DNA during the denaturation phase, the signal will be negatively affected, and fluorescence may be delayed or prohibited. In this case, the results indicate that the 1 s dwell time was insufficient, and fluorescence was impeded. When the average values for the 15 s dwell time were compared to 7 and 1 s data via Dunnett's multiple comparisons test, the data obtained for the 15 s and

1 s dwell times were statistically different ($p = 0.0026$). For 15 s vs. 7 s, however, there were no statistical differences ($p = 0.8106$), and the 7 s dwell time was selected for subsequent experiments.[13,16]

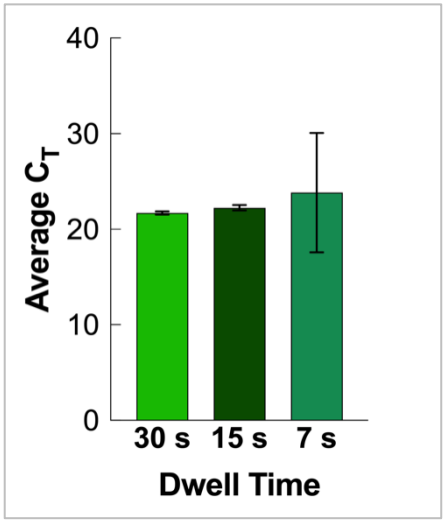

Figure 5-5. Comparison of data obtained for optimization of the amplification cycle's annealing dwell time using the conventional instrument. The 15 s dwell time was selected in this case (*n = 3*).

Finally, the dwell times for the annealing step were evaluated. Dwell times of 30, 15, and 7 s were tested to determine optimal parameters, and the results were compared. The average values obtained in this case were 21.7 ± .166, 22.3 ± 0.272, and 23.8 ± 6.26 for 30, 15, and 7 s dwell times, respectively (summarized in **Figure 5-5**). When directly compared using Dunnett's multiple comparisons test, there were no statistical differences for 30 s vs. 15 s ($p = 0.9768$) and 30 s vs. 7 s ($p = 0.7116$).[13,16] While there was no statistical difference between means, the standard deviation for the 7 s dwell time data was quite significant. The 15 s dwell time was thus selected for this step.

Overall, the dwell time was reduced from ~ 59 minutes with an average C_T value of 20.7 ± 0.05 to ~ 38 minutes (37 min 51 s) with an average C_T value of 22.3 ± 0.272. Despite the 1.6 unit increase in C_T, there was a 36% reduction in runtime. The minor increase was thus not viewed as a deterrent, and optimization experiments on the microfluidic device were initiated. The parameters for the optimized protocol are summarized in **Table 5-3**.

Table 5-3. Summary of optimal parameters for thermal cycling derived using the conventional instrument. The manufacturer's recommended conditions are given in parentheses in red following the optimized values.

SOURCE	OPTIMIZATION EXPERIMENTS		
CONDITIONS	**T (°C)**	**Time (s)**	**No. of cycles**
INITIAL DENATURATION	95	60 (60)	1 (1)
AMPLIFICATION CYCLES	95 60	7 (15) 15 (30) (+ plate read)	40 (40 - 45)
COOLING STEP	N/A	-	

Optimization using the microfluidic instrument

As was the case in **Chapter 4**, the optimization experiments on the microfluidic platform utilized the thermocycling protocol derived from the conventional instrument. The protocol applicable in this case is described in **Table 5-3.** as the starting point. However, the influence of adjusting the ramp rate was additionally evaluated given the theorized enhancement of amplification due to a higher surface-area to volume ratio and accelerated kinetics.[15,19]

Note, IS481 and IS1002 targets were evaluated in this phase of experiments as the persistent contamination issue had been resolved by this time. It was theorized that if the conventional instrument settings worked for the IS1002 target, which is lower in prevalence than the IS481, the conditions should also be applicable to the non-optimized insertion element. As such, the traditional experiments were not adjusted nor repeated for this target. The data obtained for each insertion element will be detailed in sequence, as

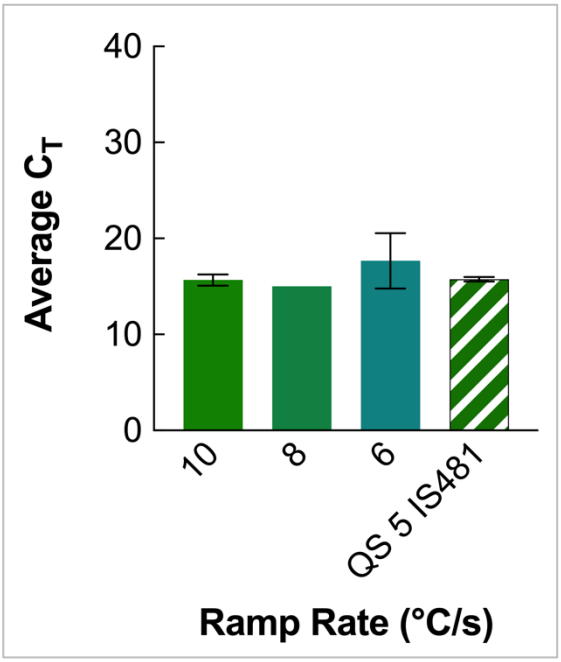

Figure 5-6. Optimization of ramp rate using the microfluidic instrument – IS481 target. There were no statistical differences between means at the 95% confidence level (*n = 3 for microfluidic assays and 5 for conventionl assays).* QS 5 denotes the Quant Studio conventional instrument.

this research aims to find optimized parameters compatible with the detection of both targets.

Ramp Rates

The ramp rates evaluated were 6, 8, and 10 °C/s for heating and 10 °C/s for cooling.[15] Preliminary experiments indicated that a ramp rate of 4 °C/s (tested in **Chapter 4** for microfluidic experiments) led to non-specific binding amplification and the generation of bubbles within the microfluidic chamber, and this was excluded.

The data obtained for the IS481 target is summarized in **Figure 5-6**, while that for IS1002 is outlined in **Figure 5-7**. In the case of IS481, the average C_T values obtained were 15.7 ± 0.577, 15.0 (No deviation, ND), and 17.7 ± 2.89 for 10, 8, and 6 °C/s ramp rates, respectively. According to Dunnett's multiple comparisons test, there were no statistical differences between means. Still, the 6 °C/s ramp rate had the highest standard deviation and the slowest ramp rate. Although the 8 °C/s ramp rate yielded means with no deviation, the 10 °C/s ramp rate was chosen as it was most in line with the overall goal of runtime reduction, in addition to being statistically similar to the data used as the basis of comparison.

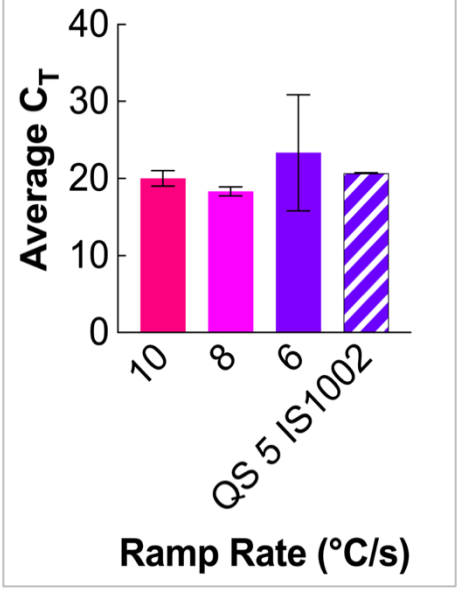

Figure 5-7. Optimization of ramp rate using the microfluidic instrument – IS1002 target. There were no statistical differences between means at the 95% confidence level (*n = 3).* QS 5 denotes the Quant Studio conventional instrument.

For IS1002, the average values obtained were 20.0 ± 1.00, 18.3 ± 0.577, and 23.3 ± 7.51 for rates of 10, 8, and 6 °C/s, respectively. According to an ordinary one-way ANOVA, there was no significant differences between means ($p = 0.4823$, $\alpha = 0.05$). Dunnett's multiple comparisons test showed no statistical differences when the value obtained using the manufacturer's protocol was compared to those obtained using the 10 ($p = 0.9920$), 8 ($p = 0.7926$), and 6 ($p = 0.7353$) °C/s ramp rates ($\alpha = 0.05$). Still, the standard deviation when a ramp rate of 6 °C/s was used was significant, and the average C_T value obtained using this parameter was confirmed during a series of retests. The disparity of values obtained was thought to be due in part to the generation of air pockets observed using the 4 °C/s ramp rate, and this option was excluded. 10 °C was chosen as this was also well-suited to analyses targeting the IS481 insertion element.

Initial Denaturation

The dwell times analyzed for this step were 60 s, 30 s, and 1 s. The values obtained for the IS1002 insertion element were 20.3 ± 1.53 for the 60 s dwell time, 19.7 ± 1.15 for the 30 s dwell time, and 22.3 ± 0.577 for the 1 s dwell time. These data are summarized in **Figure 5-8**. An ordinary one-way ANOVA test showed no significant differences between

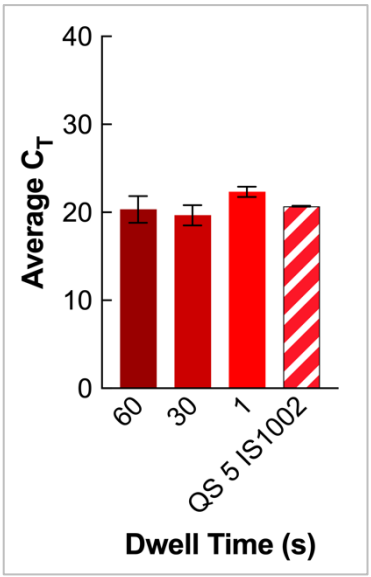

Figure 5-8. Optimization of initial denaturation step using microfluidic instrument – IS1002 target. There were no statistical differences between means at the 95% confidence level (*n = 3).* QS 5 denotes the Quant Studio conventional instrument.

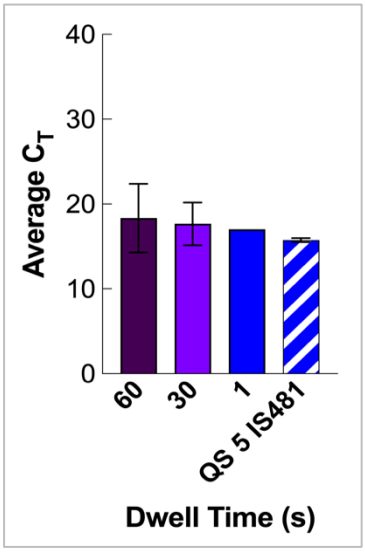

Figure 5-9. Optimization of initial denaturation step using the microfluidic instrument – IS481 target. There were no statistical differences between means at the 95% confidence level (*n = 3 for µfluidic instrument, 5 for QS5).* QS 5 denotes the Quant Studio conventional instrument.

means at a 95% confidence level (p = 0.0563). When individual values were directly compared to those obtained using the conventional instrument using Dunnett's multiple comparisons test, there were no significant differences between the QS5 (Quant Studio 5) values vs. those derived using dwell times of 60 s (p = 0.9475), 30 s (p = 0.4941), and 1 s (0.1784).

For the IS481 insertion element, the average C_T values obtained were 18.3 ± 4.04, 17.7 ± 2.52, and 17.0 (ND) for the 1 s dwell time. These results are summarized in **Figure 5-9**. As with IS1002, there were no statistical differences between means at a 95% confidence level (p = 0.4091), and direct comparisons showed no statistical differences between QS 5 and 60 s (p = 0.2987), 30 s (p = 0.5200), or 1 s (p = 0.7852) data ($\alpha = 0.05$).

However, the dwell time that could reliably be used for both insertion elements was 1 s. Still, this resulted in a 1.3 unit increase in C_T value for the IS481 target and a 1.6 unit increase for the IS1002 target. This was determined to be a minor acceptable loss, and optimization experiments continued.

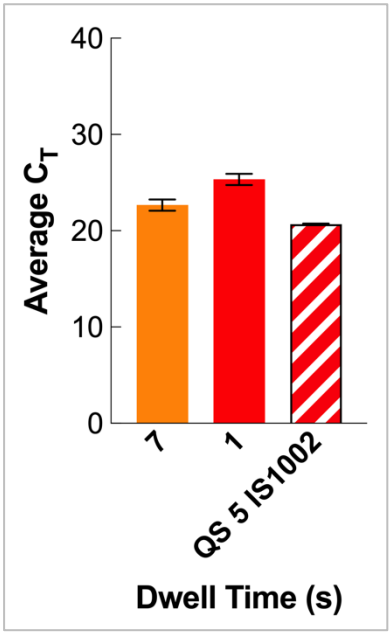

Figure 5-10. Optimization of denaturation step of the amplification cycling phase using the microfluidic instrument – IS1002 target. There were statistical differences between means at the 95% confidence level (*n = 3*, p = <0.0001*)*. QS 5 denotes the Quant Studio conventional instrument.

Amplification Cycles - Denaturation

For IS1002, the average C_T values obtained were 22.7 ± 0.577 and 25.3 ± 0.577 for the 7 and the 1 s dwell times, respectively. These results are summarized in **Figure 5-10**. A one-way ANOVA test indicated statistical differences between means at a 95% confidence level ($p < 0.0001$). Dunnett's multiple comparisons test for QS 5 data vs. that obtained using the 7 s and 1 s dwell times showed that these were statistically dissimilar and produced p values of 0.0039 and p <0.0001, respectively.

In the case of IS481, the average C_T values derived from the experiments to optimize the denaturation phase were 16.3 ± 0.577 for 7 s dwell times and 19.7 ± 0.577 for 1 s dwell times, as illustrated in **Figure 5-11**. There were significant differences between means at the 95% confidence level when a one-way ANOVA test was performed ($p < 0.0001$). However, Dunnett's multiple comparisons tests showed that while there was a significant difference observed when the QS 5 average value was compared to the data obtained for the 1 s dwell time ($p < 0.0001$), there was no difference between QS 5 data and that obtained for the 7 s dwell time ($p = 0.1901$).

Given that no significant difference was observed when the data from the 7 s dwell time and conventional instrument were compared (IS481), this time was chosen for the next phase of experiments. Though there was a statistical difference for both dwell times

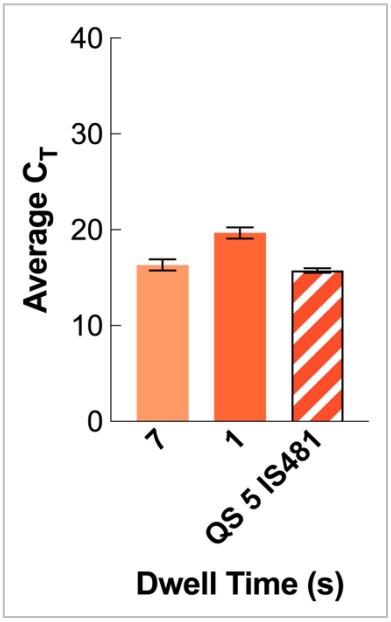

Figure 5-11. Optimization of denaturation step of the amplification cycling phase using the microfluidic instrument – IS481 target. There were statistical differences between means at the 95% confidence level (*n = 3* for µfluidic instrument and *5* for the QS5*)*. QS 5 denotes the Quant Studio conventional instrument.

evaluated for the IS1002 target, it was determined that the magnitude of the delta between the conventional data and the microfluidic data would be analyzed to determine if the loss in C_T units was tenable. The loss of 2 units was determined to be acceptable given the overall potential of the optimized assay, and 7 s was used as the denaturation dwell time for the experiments to optimize parameters for the annealing step.

Amplification Cycles – Annealing Step

The final step, annealing, was optimized by testing dwell times of 15 s, 7 s, and 1 s for both targets. For IS1002, the average C_T values for each dwell time were 24.3 ± 0.577, 25.7 ± 1.15, and 29.3 ± 0.577 for the 15, 7, and 1 s dwell times, respectively (**Figure 5-12**). A one-way ANOVA test revealed that there were significant differences between these means ($p < 0.0001$, $\alpha = 0.05$). Dunnett's multiple comparisons test showed that for the QS 5 data vs. the data acquired using the 15 s dwell time, there was a statistical difference at the 95% confidence level ($p = 0.0006$). This was also the case for comparisons to 7s, and 1 s dwell times, with p values of < 0.0001 in both instances.

For the IS481 insertion element, average C_T values for 15, 7, and 1 s dwell times were 19.0 (ND), 21.7 ± 1.15, and 29.3 ± 0.577. One-way ANOVA testing indicated significant differences between means at the 95% confidence level ($p < 0.0001$), and

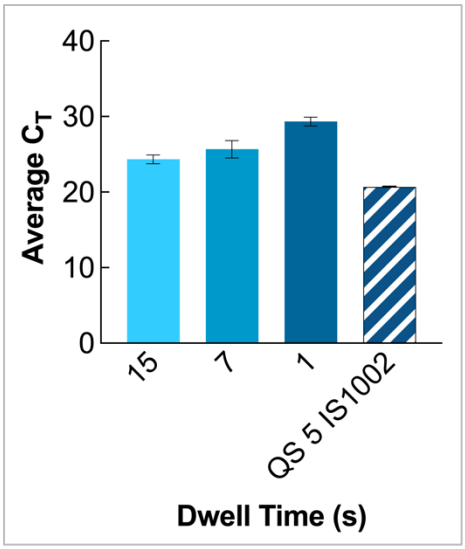

Figure 5-12. Optimization of the annealing step dwell time using the µfluidic instrument – IS1002 target. There were statistical differences between these means at a 95% confidence level ($p < 0.0001$).

Dunnett's multiple comparison tests showed statistical differences between QS5 values and data acquired at all dwell times ($p < 0.0001$).

The completion of the annealing optimization experiments introduced a challenge. Recall, the average C_T values obtained when the manufacturer's protocols and conventional instrument were used were 20.7 ± 0.050 for the IS1002 insertion element and 15.7 ± 0.243 for the IS481 insertion element. Following optimization experiments on the microfluidic device, it was evident that the dwell time for the annealing step which would give the most favorable results would be 15 s. Still, the dwell time that would give satisfactory results but with a more significant increase in cycle threshold values was 7 s. As such, a determination had to be made as to whether or not the deciding factor would be retaining the maximum amount of sensitivity or completion of the assay in the fastest possible time. If the 15 s dwell time were chosen, the overall runtime for the optimized protocol would be 17.7 minutes, compared to a 12.5 min runtime if the 7 s dwell time was selected. However, for the IS1002 insertion element, this would mean an increase in average C_T value of 5 units compared to 3.6 units for the 15, and 7 s dwell times, respectively. In the case of the IS481 insertion element, this would entail an increase in average values of either 6 units or 3.3 units.

Although the increases for the 7 s dwell times were not insignificant, this dwell time was selected as the average C_T values were still well within the bounds of an acceptable positive value and would thus still be recognized as positive diagnoses (≤ 35 cycles).[4,20] The final deciding factor would likely be the application of the protocol to clinical samples using either dwell time and determining the practical impact of this difference.

Considering this determination, the protocol derived using the microfluidic instrument involved a 10 °C/s ramp rate, a 1 s initial denaturation step at 95 °C, and amplification cycles of 1 s at 95 ° C for denaturation and 7 s at 60 °C for annealing. This optimized protocol had a runtime of 12 min and 30 s, giving a 46.5 min reduction in runtime (79 %) from the initial 59 min process when conducted using the microfluidic instrument compared to the conventional device.

5.4. Conclusions

The optimization of thermocycling parameters for the adaptation of a whooping cough diagnostic assay to an ultra-rapid microfluidic PCR instrument is described here. The optimization process entailed systematic variation of parameters at each stage of the PCR process and statistical analyses of the data obtained to determine the feasibility of a practical application. This was first completed using a conventional instrument (the QuantStudio™ 5 Real-Time PCR System for Human Identification using the IS1002 insertion element. The optimized parameters from these experiments were then transferred to the microfluidic platform and further evaluated to determine the shortest viable assay runtime that could be employed with minimal losses in sensitivity.

Consequently, the runtime for successful detection and diagnosis of these insertion elements, which are prevalent in the genome of the *Bordetella pertussis* bacteria, the primary causative agent of whooping cough, was reduced from 59 minutes to 38 minutes using the conventional instrument, a reduction of 21 minutes (36%). The runtime was further reduced to 12 minutes and 30 seconds when adapted to the microfluidic device, a decrease of 46.5 minutes (79%). Although there were some losses in sensitivity, successful detection of targets was achieved at threshold values well below the diagnostic "cutoff" value of 35 cycles, and the adapted protocol was determined to be viable for further validation experiments. Additionally, a significant reduction in time was achieved with no adjustments to the amplification mixture.

These proof-of-concept experiments are foundational, with the final validation of the adapted protocol being its application to clinical samples for diagnoses. Still, these represent significant potential for the eventual field deployment of an accurate and sensitive multitarget microfluidic instrument for onsite detection of whooping cough.

5.5. References

1. Loeffelholz, M. J.; Tang, Y.-W. Laboratory Diagnosis of Emerging Human Coronavirus Infections – the State of the Art. *Emerging Microbes & Infections* **2020**, *9* (1), 747–756. https://doi.org/10.1080/22221751.2020.1745095.

2. Hewlett, E. L.; Burns, D. L.; Cotter, P. A.; Harvill, E. T.; Merkel, T. J.; Quinn, C. P.; Stibitz, E. S. Pertussis Pathogenesis--What We Know and What We Don't Know. *J Infect Dis* **2014**, *209* (7), 982–985. https://doi.org/10.1093/infdis/jit639.

3. Martini, H.; Detemmerman, L.; Soetens, O.; Yusuf, E.; Piérard, D. Improving Specificity of Bordetella Pertussis Detection Using a Four Target Real-Time PCR. *PLoS One* **2017**, *12* (4), e0175587. https://doi.org/10.1371/journal.pone.0175587.

4. Tatti, K. M.; Sparks, K. N.; Boney, K. O.; Tondella, M. L. Novel Multitarget Real-Time PCR Assay for Rapid Detection of Bordetella Species in Clinical Specimens. *J Clin Microbiol* **2011**, *49* (12), 4059–4066. https://doi.org/10.1128/JCM.00601-11.

5. *Pertussis (Whooping Cough)*. https://www.cdc.gov/pertussis/fast-facts.html (accessed 2022-07-11).

6. Yeung, K. H. T.; Duclos, P.; Nelson, E. A. S.; Hutubessy, R. C. W. An Update of the Global Burden of Pertussis in Children Younger than 5 Years: A Modelling Study. *Lancet Infect Dis* **2017**, *17* (9), 974–980. https://doi.org/10.1016/S1473-3099(17)30390-0.

7. Kilgore, P. E.; Salim, A. M.; Zervos, M. J.; Schmitt, H.-J. Pertussis: Microbiology, Disease, Treatment, and Prevention. *Clin Microbiol Rev* **2016**, *29* (3), 449–486. https://doi.org/10.1128/CMR.00083-15.

8. Qin, X.; Galanakis, E.; Martin, E. T.; Englund, J. A. Multitarget PCR for Diagnosis of Pertussis and Its Clinical Implications. *J Clin Microbiol* **2007**, *45* (2), 506–511. https://doi.org/10.1128/JCM.02042-06.

9. Wendelboe, A. M.; Van Rie, A. Diagnosis of Pertussis: A Historical Review and Recent Developments. *Expert Rev Mol Diagn* **2006**, *6* (6), 857–864. https://doi.org/10.1586/14737159.6.6.857.

10. Parkhill, J.; Sebaihia, M.; Preston, A.; Murphy, L. D.; Thomson, N.; Harris, D. E.; Holden, M. T. G.; Churcher, C. M.; Bentley, S. D.; Mungall, K. L.; Cerdeño-Tárraga, A. M.; Temple, L.; James, K.; Harris, B.; Quail, M. A.; Achtman, M.; Atkin, R.; Baker, S.; Basham, D.; Bason, N.; Cherevach, I.; Chillingworth, T.; Collins, M.; Cronin, A.; Davis, P.; Doggett, J.; Feltwell, T.; Goble, A.; Hamlin, N.; Hauser, H.; Holroyd, S.; Jagels, K.; Leather, S.; Moule, S.; Norberczak, H.; O'Neil, S.; Ormond, D.; Price, C.; Rabbinowitsch, E.; Rutter, S.; Sanders, M.; Saunders, D.; Seeger, K.; Sharp, S.; Simmonds, M.; Skelton, J.; Squares, R.; Squares, S.; Stevens, K.; Unwin, L.; Whitehead, S.; Barrell, B. G.; Maskell, D. J. Comparative Analysis of the Genome Sequences of Bordetella Pertussis, Bordetella Parapertussis and Bordetella Bronchiseptica. *Nat Genet* **2003**, *35* (1), 32–40. https://doi.org/10.1038/ng1227.

11. Roorda, L.; Buitenwerf, J.; Ossewaarde, J. M.; van der Zee, A. A Real-Time PCR Assay with Improved Specificity for Detection and Discrimination of All Clinically Relevant Bordetella Species by the Presence and Distribution of Three Insertion Sequence Elements. *BMC Research Notes* **2011**, *4* (1), 11. https://doi.org/10.1186/1756-0500-4-11.

12. *Pertussis*. https://www.cdc.gov/pertussis/clinical/diagnostic-testing/diagnosis-pcr-bestpractices.html (accessed 2021-01-25).

13. GraphPad Software, L. L. C. *Prism 9 for MacOS*; GraphPad Software, LLC: San Diego, California USA, 2021.

14. Real-Time PCR Handbook - Thermo Fisher Scientific, 2014.

15. Nouwairi, R. L.; Cunha, L. L.; Scott, O.; Hickey, J.; Thomson, S.; Knowles, S.; Chapman, J.; Landers, J. P. Ultra-Rapid Real-Time Microfluidic RT-PCR Instrument for Nucleic Acid Analysis. *Lab Chip* **2022**.

16. Dunnett, C. W. New Tables for Multiple Comparisons with a Control. *Biometrics* **1964**, *20* (3), 482–491.

17. Nadkarni, M. A.; Martin, F. E.; Jacques, N. A.; Hunter, N. Determination of Bacterial Load by Real-Time PCR Using a Broad-Range (Universal) Probe and Primers Set. *Microbiology (Reading)* **2002**, *148* (Pt 1), 257–266. https://doi.org/10.1099/00221287-148-1-257.

18. *Essentials of Real-Time PCR - US*. https://www.thermofisher.com/us/en/home/life-science/pcr/real-time-pcr/real-time-pcr-learning-center/real-time-pcr-basics/essentials-real-time-pcr.html (accessed 2022-07-08).

19. Wittwer, C. T.; Herrmann, M. G. 14 - Rapid Thermal Cycling and PCR Kinetics. In *PCR Applications*; Innis, M. A., Gelfand, D. H., Sninsky, J. J., Eds.; Academic

Press: San Diego, 1999; pp 211–229. https://doi.org/10.1016/B978-012372185-3/50015-8.

20. Paddock, C. D.; Sanden, G. N.; Cherry, J. D.; Gal, A. A.; Langston, C.; Tatti, K. M.; Wu, K.-H.; Goldsmith, C. S.; Greer, P. W.; Montague, J. L.; Eliason, M. T.; Holman, R. C.; Guarner, J.; Shieh, W.-J.; Zaki, S. R. Pathology and Pathogenesis of Fatal Bordetella Pertussis Infection in Infants. *Clinical Infectious Diseases* **2008**, *47* (3), 328–338. https://doi.org/10.1086/589753.

6. Final Remarks

6.1. Conclusions

The research described in this dissertation focused on addressing an unmet need for field-forward, user-friendly, accurate, sensitive, specific, and robust technologies in the fields of forensics and clinical diagnostics for onsite applications.[1–4] Despite significant strides in diagnostic technologies, the primary model for testing solutions relies on the use of centralized laboratories.[5] As highlighted by the global COVID-19 pandemic, the reliance on centralized laboratories often creates a strain on resources and clinicians or technicians, hinders access to patients and communities, and limits attempts to mitigate the spread of illness as infected persons are not diagnosed and isolated promptly.[6,7] For forensic applications, specifically, analyses at laboratories can have turnover times on the order of days, thereby delaying investigations and potentially impeding the apprehension of perpetrators.[4] Consequently, the work outlined here details the development of microfluidic technologies geared towards addressing associated deficits in these fields.

Chapter 2 details the adaptation of an assay for identifying biological sex via analysis of fingermark deposits to a microfluidic platform. The success of this adaptation hinged on selecting a metric by which the concentration of amino acids in a given deposit could be evaluated. Further, methods of detection amenable to the assay, in this case, the Sakaguchi test, while being adaptable to a microfluidic device were required. The PCL fabrication method worked in concert with the colorimetric detection of arginine via a standard computer scanner, image analysis techniques, and the application of centrifugal principles to create a microdevice capable of performing several of the unit operations required for onsite deployment of this assay.[8–11]

Chapter 3 describes a departure from forensic diagnostics to detail the development of a sensitive, rapid SARS-CoV-2 diagnostic method for large-scale population screening.[12] This entailed the use of nanoparticle enrichment techniques coupled with PDQeX extraction technologies to detect minute concentrations of viral RNA in clinical saliva samples. This leveraged previously developed technology to extract viral RNA from clinical specimens derived from nasopharyngeal swabs in viral transport media (VTM), "fresh" saliva samples spiked with positive clinical samples, and clinical saliva samples. The results obtained for low, moderate, and high viral titer samples of each sample type were assessed and compared. The most favorable data was produced from analyses of the saliva specimens collected by patients using a commercially available kit. Microfluidic adaptation of the assay combined with the use of gold standard instrumentation was employed to demonstrate successful detection of the virus in dilution pools up to 1:100. A blind study confirmed the potential for practical applications of the developed techniques as results were 100% concordant with the clinical diagnoses provided by the sample source following experiments.

Preliminary experiments demonstrated the potential for optimizing the pooling assay for point-of-need (PON) deployment using a novel, ultra-rapid, microfluidic PCR amplification device. The reduction of overall assay runtime was briefly introduced in this chapter, with a 57% decrease in runtime discussed. The thermocycling program was applied to the microfluidic platform, and the chamber temperatures were monitored to create a temperature profile. The data obtained confirmed that the correct temperatures were attained during amplification and that cycling was consistent.

Chapter 4 details the next phase of these experiments. The overall assay time was further reduced by methodical adjustments of thermocycling parameters used in the PCR protocol. The physical properties of the polymeric material used to fabricate the microfluidic cartridges were combined with custom-built hardware to capitalize on the kinetic advantages inherent to analyses on the micro-scale. As a proof-of-concept, viral plasmids were used as targets – first for the in-tube, then for microfluidic optimization experiments.

Summarily, there was successful reduction of assay runtime using the conventional instrument, with the 63 min 11 s assay being decreased to 34 min and 5 s with no significant losses in sensitivity. This reduction was achieved with no adjustments to the chemistry and components of the amplification mixture obtained commercially. Further decreases in runtime were conducted using the microfluidic platform, with the final runtime of 13 min and 30 s - a 50 min (79%) reduction. This was achieved with minimal sensitivity loss ($< \pm$ 1 C_T unit). This presented a favorable alternative to centralized lab testing, where the turnover time from the collection of samples to diagnosis could be 2 – 3 days.[13] Additionally, a cartridge recycling protocol was developed, and the rationale and details of the method are outlined and discussed.

Finally, **Chapter 5** describes the utilization of similar concepts to optimize thermocycling parameters for PCR detection of whooping cough. Two insertion elements – IS481 and IS1002 were targeted due to their prevalence in the *pertussis* genome. Consequently, the optimized process applies to the detection of both insertion elements toward the goal of facilitating duplex applications.

Similar to the process detailed in **Chapter 4**, the runtime was successfully reduced using the conventional instrument (59 minutes to 38 minutes, a 36% reduction). This runtime was further reduced to 12 mins and 30 s when adapted to the microfluidic device (59 minutes to 12.5 minutes, a 79% reduction). In this case, however, there were losses in the detection sensitivity, which though not prohibitive to successful diagnosis, were statistically relevant.

Chapter 3 details a protocol with the potential to facilitate large-scale molecular diagnostics in times of medical crisis. Chapters 3, 4, and 5 represent significant progress towards the eventual goal of onsite analyses enabled by microfluidic technologies.

6.2. Ongoing Studies and Future Work

Though the projects described herein detail significant strides towards addressing the need for onsite methodology and instrumentation for clinical and forensic analyses, the potential for further advancements and enhancements still exists. The additional research and development required are centered around the complete integration of and automation of process chains to facilitate sample-to-answer solutions which are not reliant on significant operator input or technical training.

6.2.1. Microdevice for Analysis of Fingermark Deposits

Although **Chapter 2** detailed 93% accuracy of identification using the proposed protocol, the deposits analyzed were donated by only 15 unknown participants. A blind study involving a much larger number of donors should be conducted to provide a more statistically robust data set.

Additionally, this study could be expanded to incorporate the evaluation of an internal standard. The analysis of another component characteristically detected in fingermark deposits due to inherent sweat content could be used to normalize variations in data. Such variations usually result from differences in individual rates of sweating and shedding. One such set of internal standards is sodium and potassium, which have previously been used to normalize the volume of sweat collected from male and female subjects in a study conducted by Appenzeller et al.[14] The primary challenge, in this case, would be the determination of a compatible colorimetric assay to work in tandem with the evaluation of arginine concentration.

Alternatively, the Bradford assay has been reported as a valuable method for normalizing amino acid content in sweat secretions. Since Bradford reagent binds primarily to arginine, lysine, and histidine, normalization would leverage the ratio of arginine compared to the other amino acids to differentiate biological sex with a pre-existing internal control. This has been demonstrated by Brunelle et al. previously. [15]

Ultimately, the ideal outcome would be the complete integration of unit operations to create an automated system for onsite use. A simple readout would rely on establishing a colorimetric threshold and programming a presumptive binary “Male” or “Female” readout.

6.2.2. Ultra-rapid, Point-of-Need Molecular Diagnostics of Pathogens for Infectious Diseases

Preliminary experiments in Chapter 3 demonstrated the potential for using a novel, ultra-rapid microfluidic PCR amplification device to detect and diagnose SARS-CoV-2 in clinical saliva and nasopharyngeal samples diluted up to 1:100. This forecasted the research

described in Chapter 4. As the capability of detection in large sample pools had been demonstrated, the focus shifted from establishing feasibility to conducting optimization experiments. Consequently, RNA enrichment and extraction from clinical saliva samples with dilutions of up to 1:50 were performed. The final goal was to analyze these specimens using the optimized protocol and microfluidic apparatus. Unfortunately, towards the end of the optimization phase, access to the conventional instrument was not possible, and the data curated only reflects the proof-of-concept experiments performed using viral plasmids. As such, the next step of this project is assessing the practical application of the protocol using clinical samples.

First, however, the sensitivity of the optimized protocol must be verified using a molecular controls kit such as the Seracare AccuPlex™ SARS-CoV-2 Verification Panel.[16] Experiments targeted viral plasmids, which do not require enrichment or extraction. The positive kit materials include the complete SARS-CoV-2 viral genome to better approximate clinical conditions. These are viewed as full process controls, providing fully extractable RNA with a protein coat akin to virulent specimens, but without the risk of infection and replication.[16,17] Calibration curves prepared using viral plasmid vs. molecular controls would be designed and analyzed using conventional and optimized microfluidic methods. This process would allow for the evaluation of sensitivity. Practical application to “real-world” use would confirm the suitability of the rapid protocol for point-of-need deployment.

Similarly, the next validation phase for rapid diagnostic assays targeting pertussis entails practical application using clinical samples. In this case, preliminary experiments were conducted to analyze potential matrix effects. Briefly, clinical samples previously diagnosed as negative at the University of Virginia Hospital were spiked with known concentrations of *B. pertussis* template DNA. The PDQeX instrument was then used to extract DNA from the spiked clinical samples, and PCR targeting IS481 was then performed using the manufacturer's protocol and the QuantStudio™ 5 instrument. Although the correlation between concentration and average C_T value indicated by the R^2 was less favorable for spiked samples, the potential for microfluidic amplification was demonstrated. Still, an investigation of the efficiency of extraction of whole bacteria instead of free DNA is necessary, as with SARS-CoV-2 diagnoses detailed above.

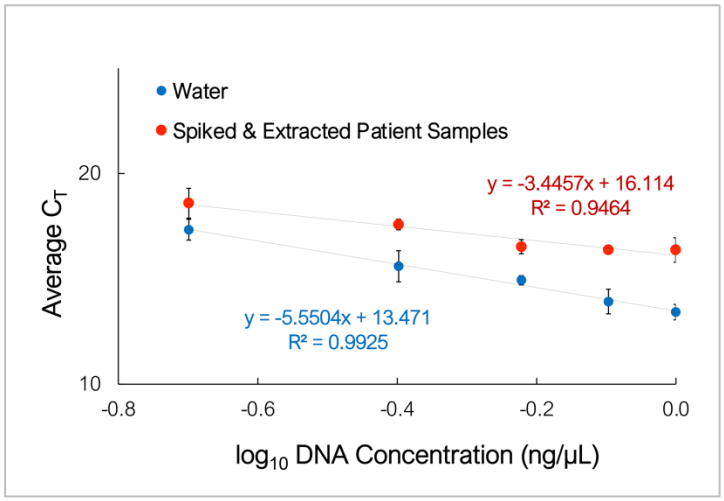

Figure 6-1. Preliminary data analyzing matrix effects. Standards were prepared by preparing solutions of known concentrations of *pertussis* template DNA using either nuclease-free water or negative clinical samples as diluent.

A fully integrated system that automates the enrichment and extraction of nucleic acids and PCR amplification with minimal complexity and operator input is in development and will represent the culmination of these projects.

6.3. Summary

The work described here focuses on applying microfluidic technologies to forensic and clinical analyses at the point of need. Such technologies provide solutions for forensic and clinical scientific communities, with unlimited potential for contributions to other fields. Given the significant advancements toward full integration and automation of relevant process chains detailed herein, the potential for realizing the initial research goals and ameliorating the existing deficit has been demonstrated.

6.4. References

1. Escobar, A.; Chiu, P.; Qu, J.; Zhang, Y.; Xu, C.-Q. Integrated Microfluidic-Based Platforms for Onsite Detection and Quantification of Infectious Pathogens: Towards On-Site Medical Translation of SARS-CoV-2 Diagnostic Platforms. *Micromachines (Basel)* **2021**, *12* (9). https://doi.org/10.3390/mi12091079.

2. Valera, E.; Jankelow, A.; Lim, J.; Kindratenko, V.; Ganguli, A.; White, K.; Kumar, J.; Bashir, R. COVID-19 Point-of-Care Diagnostics: Present and Future. *ACS Nano* **2021**, *15* (5), 7899–7906. https://doi.org/10.1021/acsnano.1c02981.

3. Jagannath, A.; Cong, H.; Hassan, J.; Gonzalez, G.; Gilchrist, M. D.; Zhang, N. Pathogen Detection on Microfluidic Platforms: Recent Advances, Challenges, and Prospects. *Biosensors and Bioelectronics: X* **2022**, *10*, 100134. https://doi.org/10.1016/j.biosx.2022.100134.

4. Bruijns, B.; van Asten, A.; Tiggelaar, R.; Gardeniers, H. Microfluidic Devices for Forensic DNA Analysis: A Review. *Biosensors (Basel)* **2016**, *6* (3). https://doi.org/10.3390/bios6030041.

5. Danielson, P. B.; McKiernan, H. E.; Legg, K. M. Integrated Polymerase Chain Reaction Technologies (Sample-to-Answer Technologies). *Molecular Diagnostics* **2016**, 59–78. https://doi.org/10.1016/B978-0-12-802971-8.00005-5.

6. Arena, F.; Pollini, S.; Rossolini, G. M.; Margaglione, M. Summary of the Available Molecular Methods for Detection of SARS-CoV-2 during the Ongoing Pandemic. *International Journal of Molecular Sciences* **2021**, *22* (3). https://doi.org/10.3390/ijms22031298.

7. Meagan N. Esbin; Oscar N. Whitney; Shasha Chong; Anna Maurer; Xavier Darzacq; Robert Tjian. Overcoming the Bottleneck to Widespread Testing: A Rapid Review of Nucleic Acid Testing Approaches for COVID-19 Detection. *RNA* **2020**, *26*, 771–783. https://doi.org/10.1261/rna.076232.120.

8. Sakaguchi, S. ÜBER EINE NEUE FARBENREAKTION von PROTEIN UND ARGININ. *J. Biochem* **1925**, *5* (1), 25–31. https://doi.org/10.1093/oxfordjournals.jbchem.a128359.

9. Brunelle, E.; Huynh, C.; Alin, E.; Eldridge, M.; Le, A. M.; Halámková, L.; Halámek, J. Fingerprint Analysis: Moving Toward Multiattribute Determination via Individual Markers. *Anal.Chem.* **2018**, *90* (3), 2401–2401. https://doi.org/10.1021/acs.analchem.8b00039.

10. Marshall, J. S.; Sita, M. L.; Landers, J. P. Microfluidic Device for the Identification of Biological Sex by Analysis of Latent Fingermark Deposits. *Micromachines* **2021**, *12* (4). https://doi.org/10.3390/mi12040442.

11. Thompson, B. L.; Ouyang, Y.; Duarte, G. R. M.; Carrilho, E.; Krauss, S. T.; Landers, J. P. Inexpensive, Rapid Prototyping of Microfluidic Devices Using Overhead Transparencies and a Laser Print, Cut and Laminate Fabrication Method. *Nat. Protoc.* **2015**, *10* (6), 875–886. https://doi.org/10.1038/nprot.2015.051.

12. Marshall, J. S.; Turiello, R.; Cunha, L. L.; Frazier, E. V.; Hickey, J.; Chapman, J.; Poulter, M. D.; Fehling, H. L.; Landers, J. P. Rapid SARS-CoV-2 Virus Enrichment and RNA Extraction for Efficient Diagnostic Screening of Pooled Nasopharyngeal or Saliva Samples for Dilutions Up to 1:100. *Diagnostics* **2022**, *12* (6). https://doi.org/10.3390/diagnostics12061398.

13. Waidi Folorunso Sule; Daniel Oladimeji Oluwayelu. Real-Time RT-PCR for COVID-19 Diagnosis: Challenges and Prospects. *Pan African Medical Journal* **2020**, *35*.

14. Appenzeller, B. M. R.; Schummer, C.; Rodrigues, S. B.; Wennig, R. Determination of the Volume of Sweat Accumulated in a Sweat-Patch Using Sodium and Potassium as Internal Reference. *Journal of Chromatography B* **2007**, *852* (1), 333–337. https://doi.org/10.1016/j.jchromb.2007.01.037.

15. Brunelle, E.; Le, A. M.; Huynh, C.; Wingfield, K.; Halámková, L.; Agudelo, J.; Halámek, J. Coomassie Brilliant Blue G-250 Dye: An Application for Forensic Fingerprint Analysis. *Anal. Chem.* **2017**, *89* (7), 4314–4319. https://doi.org/10.1021/acs.analchem.7b00510.

16. *AccuPlexTM SARS-CoV-2 Quality Solutions*. Product Sheet. https://www.seracare.com/globalassets/seracare-resources/ps-0505-0168-0159_accuplex-sars-cov-2-quality-solutions.pdf (accessed 2022-07-12).

17. Turiello, R.; Dignan, L. M.; Thompson, B.; Poulter, M.; Hickey, J.; Chapman, J.; Landers, J. P. Centrifugal Microfluidic Method for Enrichment and Enzymatic Extraction of Severe Acute Respiratory Syndrome Coronavirus 2 RNA. *Anal. Chem.* **2022**, *94* (7), 3287–3295. https://doi.org/10.1021/acs.analchem.1c05215.